Estimation of Neural Field Models from Spatiotemporal Electrophysiological Data

Yashar Baradaranshokouhi

Supervised by: Professor Visakan Kadirkamanathan

Department of Automatic Control & System Engineering

University of Sheffield

A Thesis Submitted for

Doctor of Philosophy

April 2015

I would like to dedicate this thesis to my parents.

Acknowledgements

I would like to say thanks to Professor Visakan Kadirkamanathan, my supervisor without whom this would have not been possible. I am thankful for his patience and support. Special thanks to Dr Parham Aram for his support and valuable inputs. I would also like to extend my sincere gratitude to Dr Anthony Rossiter for his support in my most critical times.

Finally, I owe my deepest gratitude to my family, especially to my father, Professor Sirous Baradaran Shokouhi who has always encouraged me in my education and research.

Abstract

The human brain is one of the most complex systems faced in research and science. Different methods and theories from various categories of science and engineering have contributed to understanding the functionality of the brain and its underlying structure. However, development of a complete theory remains a huge challenge. Among many different aspects of this field of research, one of the main branches is focused on brain disorders, causes and possible improvements to treatments and patients life quality. To tackle this challenge, experimental and clinical measurements have been used with computational models to analyse and contribute to treatments of brain disorders. Signal processing is playing a key role on detecting key features out of brain electrical recordings and developing frameworks that can give insight into underlying structure of recorded observations. As part of the scope of this thesis, previous work have been extended by relaxing some of the assumptions in earlier work and checking the performance of developed framework under new conditions.

The main focus of this thesis is based on application of Unscented Kalman Filter with Amari type model for human brain electrical activities. It is assumed that Amari type models can present the underlying dynamics of the brain activity. The Amari type model is presented in state space form and by use of a decomposition method, the estimation framework has been used to estimate the states and connectivity kernel gains. Heterogeneous connectivity is considered as long range connection in a neural network. The novelty introduced in this thesis is the introduction of a heterogeneous connectivity kernel in Amari type model and estimating the connectivity strength.

Applications of the developed methods on the synthetic data are applied on epilepsy data and results are presented. By monitoring the parameters, it is

possible to show that brain dynamics from normal to abnormal states can be detected. Further research and future work in this area can potentially lead to prediction of seizure and eventually improving life quality of patients with epilepsy.

Contents

List of Figures

List of Tables

Nomenclature

Roman Symbols

$*$	Convolution operator
$\breve{C}$	Array of observation matrix
χ	Matrix of sigma vectors
$\delta(.)$	Delta-dirac function
Γ	Inner product of field Gaussian basis functions
$\gamma(.)$	Field disturbance covariance function
μ	Long range connectivitiy gain
Ω	Spatial domain
$\omega(.)$	Spatial connectivity kernel
ϕ	Vector of field Gaussian basis functions
ψ	Vector of Gaussian basis functions
Σ	Covariance
τ	Time constant
Θ	Parameter Set
θ	Parameter set

$\top$	Transpose operator
ε	Observation noise
ς	Slope of sigmoidal activation
ξ	Synaptic parameter
ζ	Inverse synaptic time constant
C	Observation matrix
D	Temporal Differential Operator
$e(.)$	State disturbance vector
$E[.]$	Expectation function
$f(.)$	Firing rate function
$g(.)$	Weighted firing rate
$h(.)$	Synaptic response kernel
K	Filter gain
M	Cross-covariance matrix
$m(.)$	Observation kernel
n_y	Number of sensors
$q(.)$	Non-linear state function
r	Spatial location
S	Smoother gain
T	Simulation time length
t	time (index)
T_s	Sampling time

$u(.)$	Heaviside step function
$v(.)$	Mean membrane potential
v_0	firing threshold
W	Matrix of sigma vector weights
x	State vector
y	Observation vector
P	Covariance matrix

Chapter 1

Introduction

1.1 Background

Human brain is one of the most complex structures that has been studied to this date. Study of nervous system and its functionality has been extended to different science fields. Many case studies and research outcomes have suggested correlations between parts of brain actively engaged in performing specific tasks. The importance of this field has been growing rapidly during last few decades which has emerged to scientific study of nervous system as a branch of science (neuroscience) with different divisions such as computational neuroscience. Computational neuroscience is theoretical approach in the field of neuroscience to develop scientific rules and methods that can explain the underlying structure of the brain [Kandel *et al.*, 2000].

Despite large area of research in the field of neuroscience, there are many unexplored questions about the relation between different parts of the brain and how such correlations lead to a mature system that can develop cognition, logic, learning and exhibiting complex behaviours. Many attempts have been made to investigate the structure of brain dynamics by multi-disciplinary research areas between different science fields such as biology and engineering [Breakspear *et al.*, 2010].

The brain is built up of neural cells. The communication between neural cells have been studied and analysed extensively which has resulted in a good level

of understating about information flow amongst neural cells. The behaviour of larger neural populations is questioned and different models have been developed to describe the communication and synchronisation of large scale networks.

Following observations, clinical experiments and research, a general map of human brain has been established that gives a general outline of different functionalities of the brain [Johnson, 2003]. The human brain structure can be analysed in three different levels from microscopic to mesoscopic and macroscopic levels. The former one presents the properties and behaviours of a single neuron where as the latter one is a model of larger neural network. In messoscopic and macroscopic levels, effect of single neuron properties and behaviour is taken into account in large network characteristics. Indeed, such models take into account that the larger neural network behaviour is a result of smaller unit communications and their synchronisations.

It is important to build a better understanding of this level of brain activity as many of the neural disorders emerge at larger network interactions such as epileptic seizure, schizophrenia and Parkinson's disease.

In science, experimental data is usually presented by graphs, and mathematical functions are used to describe any pattern formations of data or to parametrise the underlying structure. Recording brain electrical activities has important clinical applications and can be also used to validate computational models and existing theories. In order to have a better understanding of brain dynamics as a natural phenomenon, the mathematical descriptions are used for parametrising experimental data obtained by a specific task [Spiegler *et al.*, 2011].

The term "model" is used in many scientific fields and papers. It describes many different types of structures. The range of models used in different fields expands from mathematical models of a single equation to programming codes in several pages. The more complex the system is, the more simplifications are needed to get an insight into the dynamics of the system.

It is important to clarify the difference between the model, hypothesis and the theory. Theories or hypotheses are developed for outlining mechanism of a system that should be evaluated against the real measurements.

Therefore, a model is developed to evaluate a specific feature of a theory. Application of this in the field of neuroscience yields that although the field of

computational neuroscience is a theoretical field, developed models should give a plausible presentation of underlying dynamics so results obtained by use of such models can match the experimental data. As an example, the model might assume a single neuron type as a result of which the properties of each neuron such as its connectivity strength to another neuron and its temporal characteristics is neglected in such an approach as such individual factors are assumed irrelevant to the dynamics of a large scale population. As another example, special focus is given to synchronized state of the network and heterogeneous connectivity in the network is neglected. Hence, different models have been developed targeting a number of specific areas of interest. In other words, the modelling has been subject to the objectives of the research question under investigation. There has been a good level of progress in understanding the neural functionality while the study of dynamics in large scale populations is largely open for discussion [Cunningham & Yu, 2014].

Despite the fact that much has been obtained about the structure and functional characteristics of the brain, the brain's behaviour for information processing is not well understood. In other words, there is a large field of research focused on how subcomponents of brain are communicating as a functional unit.

As a result, developing models for studying brain dynamics at a large scale network is very important. Epilepsy, Alzheimer's disease and other brain disorders are observed at large scale neural networks. Hence, developing models that describe large scale neural populations is very important [Aram *et al.*, 2013].

Another challenge is the constraints of current treatments with regards to patient specific information. Current treatments are targeting particular disease or disorders in general. However individual patient's response to prescribed treatments have been different and this is a result of various individual medical and biological background [Alejo J.Nevado Holgado, 2010]. One of the advantages of model based treatments is contributing to patient specific treatment. An interesting outcome in analysing the EEG recordings from patients include pattern of parameters for each individual [Jirsa & Haken, 1996]. Developed models can be used for analysing the observations from patients and obtained parameter trajectories reflect on underlying dynamics for each individual patient. This can contribute to improvement of treatments in future.

To have a better understanding of the methods proposed in the thesis, a brief background on biology of the human brain will be provided in Section 2.1. In the next section, the thesis structure is explained.

1.2 Thesis Structure

Chapter 1

Thesis structure and research novelty is explained with a brief introduction that provides outline of this research and explains its importance.

Chapter 2

Chapter two is the literature review where previous work is discussed and a brief introduction is given on early attempts on understanding the brain functions. This is followed by recent research outcomes which has been used as primary work in this research.

Chapter 3

One of the important properties of neuronal behaviours is related to its communication mechanism. Synaptic kernel is a key element in mean field model of neural populations. There are different models presenting this functionality of neurons. One of the simplest models for this purpose is the alpha function.

A more general expansion of alpha function is illustrated by difference of two exponential functions that can be described by a second order ODE. Although, this type of presentation does not describe the biological details in transmitting and receiving synaptic potentials, it explains this functionality with a close match to the experimental excitatory and inhibitory post-synaptic potentials. This can be explained by considering the fact that the post-synaptic response comprises a finite rise and decay time.

The derivation of the Amari type neural field model with a second order synaptic kernel is provided and synthetic data from model simulation is used in the estimation framework to obtain estimated homogeneous connectivity kernel gains, neural field and synaptic time constants.

Chapter 4

Developed estimation framework is applied to data from a patient with epilepsy and connectivity kernel gains are computed. Parameter trajectory during differ-

ent stages of a seizure is checked and changes in the parameter space is discussed.

Chapter 5

Long range connection is included in the Amari type neural field model by altering the spatial connectivity kernel to take into account the heterogeneous connectivity [Jirsa, 2002]. Such a connection topology proposes that the neural activity not only happens along neighbourhood areas in cortical grey matter but also in long range projections through the white matter [Jirsa, 2004a].

In general, based on the previous work, it has been observed that model with this details reproduces cortical propagation activity better than networks with only homogeneous connectivity kernel. Heterogeneous connectivity is introduced in the equations of the Amari type model. A state-space presentation of the model is given and parameters including connectivity kernel gains and synaptic time constant in addition to states are estimated from data. Data is generated by the neural field equations with fixed parameters. The results of the estimation enables a comparison between the true values and the estimated outputs of the model with estimated parameters.

For simulation purposes, the model is reduced to a finite-dimension state-space presentation where an estimation framework is applied. The estimation process includes a two-step iterative algorithm. First part is Unscented Raunch-Tung-Striel Smoother for estimation of the states and the second part is a least squares algorithm for estimation of the parameters. The performance of the developed method is evaluated with a Monte Carlo simulation where the consistency in the results are observed with variation of random signals at each iteration [Aram *et al.*, 2013].

Finally, chapter 6 gives a summary of results and possible future work.

1.3 Novelty of the Research

Chapter 3: Second order synaptic kernel

A second order synaptic kernel has been considered that leads into a second order ordinary differential equation (ODE). It has been implemented in the model derivation given for a homogeneous field. The resulting model and estimation equations are original contributions of this chapter.

Chapter 4: Application of second Order synaptic kernel to experimental data

This chapter demonstrates the application of connectivity kernel estimation to intracranial Electroencephalography (iEEG) recordings during an epileptic seizure and shows the potential for detecting and characterising the phases of epileptic episodes.

Chapter 5: Heterogeneous connectivity

The main novelty of this chapter is introduced by integrating the long-range connections in previous work to the homogeneous field. The estimation framework and the model derivation are extended to take into account a simplified model of long-range connections which introduces heterogeneous connectivity. Model mismatch has been used to identify the locations of the long-range connections.

Chapter 2

Literature Review

2.1 Brief Foundation of Brain Physiology

From early ages, there has been an ongoing interest in studying the human organ systems. In many years of research and experimental experience, different organ systems have been analysed and treatments to various diseases have been discovered. Among all, human brain has remained one of the most mysterious complex systems and there is a large body of research conducted on nervous system disorders and different methods for their treatments. Nervous system plays a key role in the human body. It is involved in daily activities, emotions and sensing the surrounding environment, learning and many other functionalities. Nervous system of a human body consists of different parts, for a detailed explanation of each part the interested reader can refer to Bear *et al.* [2007].

There are different research fields with objectives to show the resemblance of human nervous system to sophisticated artificial networks or neural systems in other live species such as cats, mice and monkeys [Bressloff, 2003; Wright & Liley, 1996].

As part of the introduction, a brief review will be given about the structure of the brain and different terms that will be used through out this thesis. It is not the intention of this thesis to target the full scientific vocabulary of the neuroscience research field. Some of the references that can provide a good cover for this purpose can be named as Bear *et al.* [2007]; Kandel *et al.* [2000].

There is a clear connection between different human body organs and a defined list of activities. Simple examples of this in a general case of human body can be named as the use of hands and fingers to handle objects and to hold them; feet help an individual to walk, run or stand and eye enables observing the surrounding. In a similar approach, an ancient Greek scholar made the conclusion that human brain has the functionality of sensing its surrounding environment [Bear *et al.*, 2007].

A well-known Roman scholar Galen, performed different experiments on sheep brains. Also, his work included treating patients with brain injuries. Based on his observations, the sheep brain can be divided into two parts named as the cerebrum and the cerebellum. It was concluded in his work that the cerebrum is made of a more tough material in comparison with the cerebellum. In his belief, cerebrum had the responsibility for sensing the surrounding environment and cerebellum was in charge of muscles and movements. His early observations was not far from reality. Later in 17^{th} and 18^{th} centuries, this was improved by Galen which gave rise to allocating different body functionalities to different parts of the brain (localisation of various activates in the human brain) [Bear *et al.*, 2007].

Towards the end of the 19th century, human nervous system was reviewed in different parts such as brain, spinal cord and peripheral part. These were the beginnings of categorising human nervous system into local sub-categories.

The next milestone in human brain research relates to findings about the structural forms of bumps (Called gyri) and grooves (called sulci and fissures) in each individual person. It was based on this, that cerebrum was sub-categorised into two main lobes. This was an early step in further functional localisation of the human brain. By this, it means that each part of the brain is expected to be involved in a specific range of activities. Hence, such activities are related to different localised parts of the brain. One of such methods used in assigning a specific activity to a part of the brain is called experimental ablation. On this method, part of a brain is injured or deactivated and the effect of this experiment is observed on a specific activity [Bear *et al.*, 2007].

In 1811, it was suggested that the role of cerebrum is in receiving sensory information and the cerebellum is the origin of the motor signals (motor signals are

signals that cause a move). Later in 1823, French physiologist Marie-Jean-Pierre Flourenes applied the ablation experiment on birds brain. The results confirmed the Galens and Bells earlier statements about cerebrum and cerebellum. Flourens experiments demonstrated that cerebellum was actively involved in coordination of movements while perception and sensation is highly related to cerebrum [Bear *et al.*, 2007]. Based on the observations of Paul Broca, a French neurologist, it was found that human cerebrum was directly connected to speaking abilities. This came to his attention when treating a patient who could hear but could not speak. After the patient's death, a lesion was found on his left frontal lobe. Later on, several similar cases also reported this correlation [Bear *et al.*, 2007].

The above history is a small number of contributions in mapping the nervous system and human brain into different activities. Following the previous work, human nervous system is now considered to be made of four main regions namely, spinal cord, brain stem, cerebral cortex and cerebrum.

A brief review is given for the main divisions of human brain in the following sub-sections:

Cerebellum

Cerebellum is believed to be in charge of particular automotive movements and motor behaviours. Recent research has revealed the relevance of this part of human brain to cognitive functions such as learning, language and attentions. This is also involved in rhythmic movements [Kandel *et al.*, 2000].

Cerebral Cortex

One of the largest part of the brain is the cerebral hemisphere where the cerebral cortex is also located. Cerebral cortex is the thin outer layer of the cerebral hemisphere which is responsible for functions such as planning and execution of daily activities. Cerebral cortex has been divided into four parts namely, frontal lobe, parietal lobe, temporal and occipital lobes.

Hippocampus

This is another part of the cerebral hemisphere which is believed to be highly related to occurrence of seizures and epilepsy. Hippocampus is involved in long-term memory storage and its malfunction can lead to Alzheimer's diseases.

Thalamus

Thalamus plays an important role on crossing the information between cortex

and brain stem. Because of this, it is involved in many different functions and activities such as attention, timing and movements. It is associated with seizure and epilepsy [Kandel *et al.*, 2000].

On a smaller scale, all body organs are built of cells and human brain is not excluded from this list. At this level, a good understanding of cell structure and function can provide dynamics of the neural field [Bear *et al.*, 2007]. A closer look at brain cells has enabled sorting neural cells into different categories. Cell function, chemistry and structure are a number of cell features that are involved in categorising the cells. Between different cell types, neural cells are considered as one of the most important categories as neural cells are in charge of sensing the environment and communicating to other neurons.

The glia or lial cells are involved in insulating, nourishing and supporting neighbourhood neurons. It is interesting to know that glia is a Greek word that is called glue and it is believed to keep the brain in one peace. Based on the publications of Camilo Golgi, it is observed that the neural cells shape consists of two main parts namely cell body and neuritis. In his work, the neuron body was turned into darker colour in comparison to other brain tissues. Neural cell body is called Soma. Neuritis are branches separated from body cell which can be divided into two categories namely as dendrites and axons. Axon length can reach up to a centimetre or two in some cases where as dendrites have a shorter and thinner branches from cell body [Bear *et al.*, 2007].

Connected neural cells are exchanging electrical signals via chemical channels where such signals are called action potentials. The communication system between neurons can be explained in three different stages. First presynaptic action potentials which is basically, the action potentials received from previous layer of neurons. This is integrated in the neural cell (based on internal properties and characteristics of the cell) and a new action potential is sent out to the next layer which is called postsynaptic action potential.

The receiving end of an action potential is called postsynaptic cell and the source of the action potential is called the presynaptic cell. In the first step, it is important to have a simple function describing a single neuron. A neuron structure is illustrated in Figure 2.1.

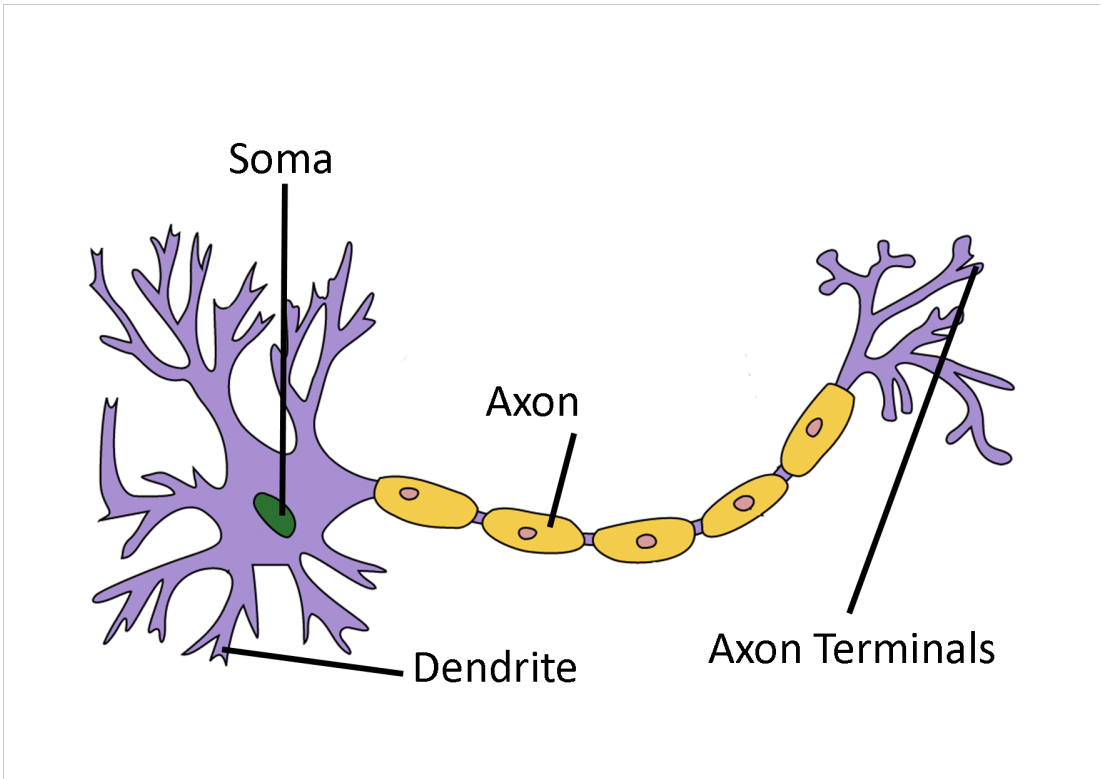

Figure 2.1: Neuron structure - adapted from Wikipedia [2009].

A single neuron comprises of a soma, an axon and dendrites. The central part of a neuron is called the soma with a typical diameter of 20 micrometres [Bear *et al.*, 2007; Fratini *et al.*, 2015]. Another important part of a neuron is the axon, specialised in transferring the information between neurons [Dityatev & Rusakov, 2011; Sejnowski & Poggio, 2007].

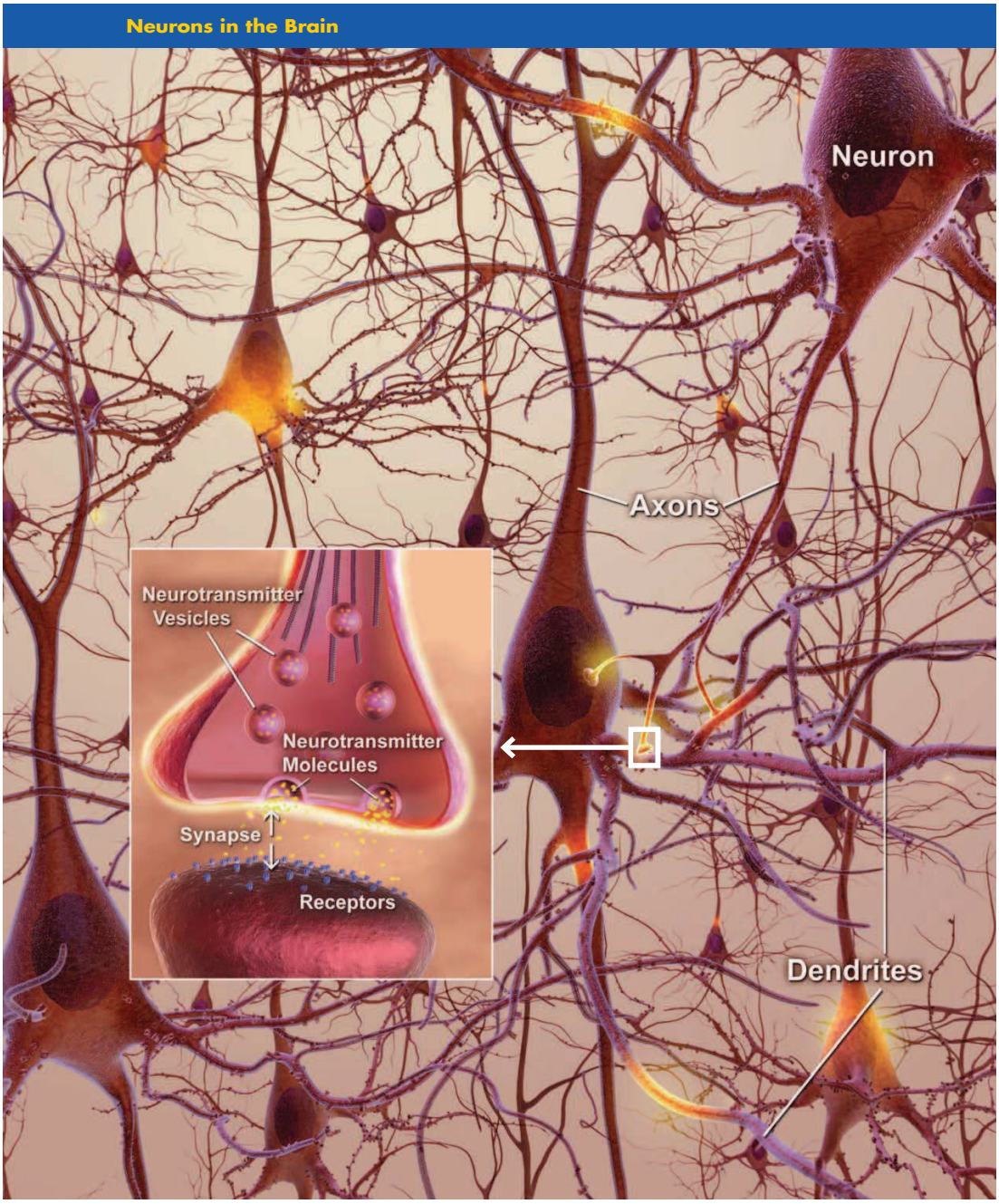

Figure 2.2: Neuron structure illustrating the synapse - extracted from US National Institutes of Health [2008].

The process of transferring the information from one neuron to another one is called synaptic transmission. As illustrated in Figure 2.2, the gap between the presynaptic and postsynaptic membranes are named as synaptic cleft. Transmission of the information between the neurons happens as electrical signals along the axons change to chemical signals at the synaptic cleft. The chemical signal is called the neurotransmitter. The electrical-chemical-electrical transformation enables communication between neurons [Gibson *et al.*, 2005].

The presynaptic potentials are integrated in the membrane of the neuron and a postsynaptic action potential is fired if the integral of presynaptic potentials reaches a specific threshold potential.

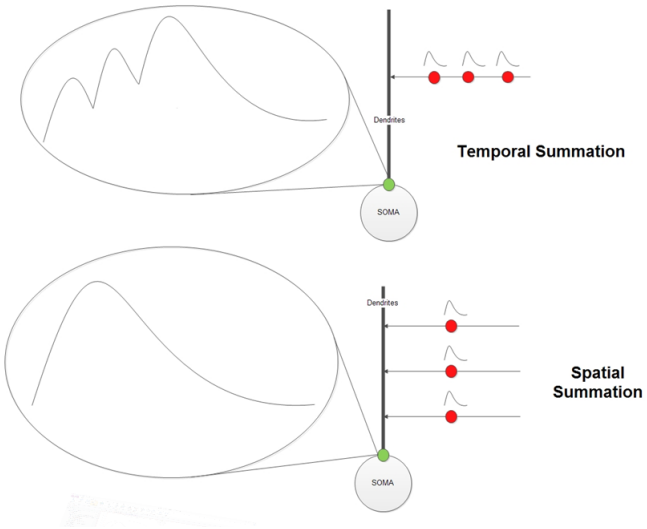

Figure 2.3: Spatial and temporal presynaptic potentials - adapted from Bear *et al.* [2007].

The integration of presynaptic potentials received from the dendrite can be separated in two groups as spatial and temporal summation [Magee, 2000]. Spatial summations happen at the same time but at different spatial locations. The temporal summation happens when presynaptic potentials arrive at the same location but with a different time delay. This is demonstrated in Figure 2.3 where as an example, three presynaptic potentials arrive at different locations on the dendrite simultaneously (spatial summation) and the result of summation is displayed on a separate curve. The same is plotted for temporal summation when three presynaptic potentials arrive at dendrite with different time delays. Result

of integration shows an increase in the amplitude over time.

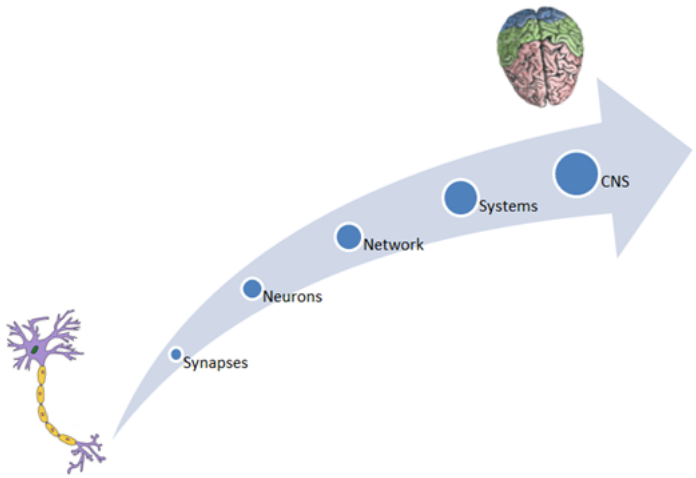

Figure 2.4: Different neural scales, from a single neuron cell to human brain - adapted from Wikipedia [2009]

Communication of neurons results in synchronised local electrical activity. Figure 2.4 demonstrates a general outline of neural communication in different scales [Hormuzdi *et al.*, 2004; Moratal, 2012]. It is not the purpose of this thesis to discuss biological details. Interested readers are referred to the book of Principles of Neuroscience Kandel *et al.* [2000].

2.2 Synaptic Response

Different physiological processes are involved in a synaptic transmission that makes the modelling of the synaptic transmission a difficult task. There are many synapses in a small size network with stochastic nature since synapses change their properties over time. In some of the models, presynaptic signals and neural communication from a close neural neighbourhood are considered by a sigmoid firing rate function [Abbott, 1991]. In such a structure, the postsynaptic currents are described by a first order ODE in which a term is related to the presynaptic potential by a sigmoid function [Destexhe *et al.*, 2002]. As

an example of such a model, Wilson & Cowan, characterise the neural field as a fraction of the neural activity in a small spatial neighbourhood (instead of a single neuron activity) in each time unit.

As a result of such complexities, many abstractions and simplifications are considered when modelling synaptic response. As part of such simplifications, synapses are assumed to be excitatory or inhibitory connections which ignores the diversity of synapses. A model that represents the full details of the ion channels and synapses will be computationally and mathematically very complex. In this work, more computationally efficient models are considered that can present various synaptic currents. A simple model for postsynaptic conductance can be named as alpha function given in equation (2.1).

$$h(t) = \frac{-t}{t_s} e^{\frac{-t}{t_s}} \tag{2.1}$$

Alpha function introduced by Rall [1967], is a popular model for presenting different forms of postsynaptic currents. In equation (2.1), t denotes time, e(.) is an exponential function and the term t_s presents the time constant for postsynaptic potential and it can be used to distinguish between the fast and slow synaptic kernel responses [Bhattacharya, 2013; Whittaker, 1963]. In other words, the alpha function has a single time constant. As a result, rise and decay time constants are correlated and they can not be set individually [Roth, 2009].

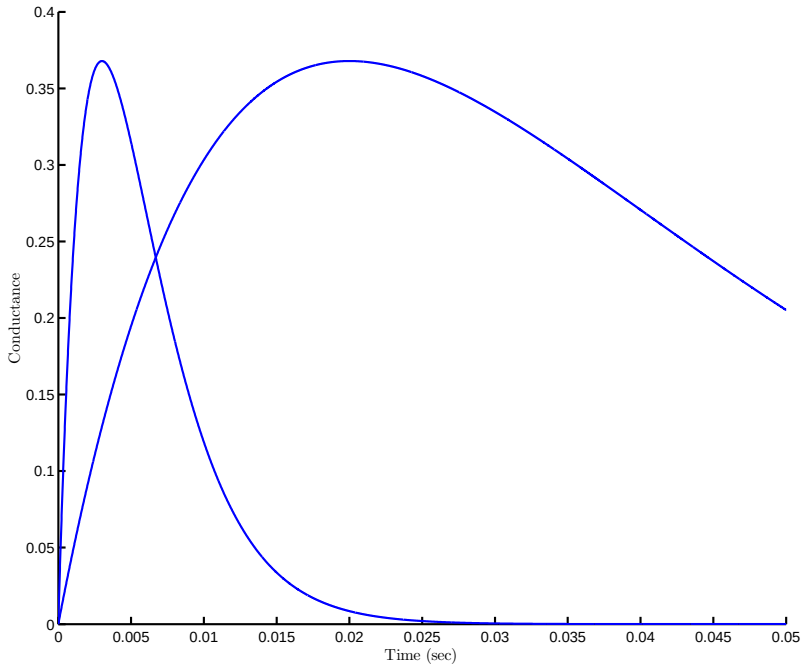

Figure 2.5: Postsynaptic Conductance generated by alpha function with two different time constants (3 ms and 20 ms).

Plots of synaptic conductance with two different synaptic time constants for the alpha function is plotted in Figure 2.5. The synaptic conductance with smaller time constant of 3 milliseconds shows a faster response in comparison to the slower time constant of 20 milliseconds. It is important that the duration of the simulations should last long enough to accommodate the full synaptic response. This is considered for setting the simulation run times in the next chapters.

A generalisation of the alpha function leads to difference of two exponential functions. This type of model with low number of parameters can be used to present various synaptic currents. It is computationally simple and it is implemented in different studies and previous work Gabbiani *et al.* [1994]. A main disadvantage of models with low number of parameters that present the vast variety of synaptic currents _ specially in this case, the alpha function _ is lack of direct biological interpretation [Destexhe *et al.*, 2002].

In the following equation, the two time constants ζ_1 and ζ_2 present the time constant for inhibitory and excitatory synapses respectively. This form of the

synaptic kernel, $h(t)$, is inspired by Marten *et al.* [2009a].

$$h(t) = \frac{\zeta_1\zeta_2}{\zeta_2 - \zeta_1}\left[\exp(-t/\tau_1) - \exp(-t/\tau_2)\right] \tag{2.2}$$

Where τ_1 and τ_2 are inhibitory and excitatory time constants, respectively. Inverse of time constants are given by ζ_2 and ζ_1. Equation (2.2) can be described as the solution to a second order differential equation as $(\partial^2+(\tau_1+\tau_2)\partial+\tau_1\tau_2)h(t) = 0$ where ∂ presents a differential operator.

Having provided a brief introduction on history of human brain and theoretical approaches in understanding its function and dynamics, it should be also mentioned that human brain as one of the most complex systems has shown a number of disorders which have been studied for several years. Next section will focus on brain disorders and more specifically on epileptic seizures.

2.3 Brain Disorders

For many brain disorders, temporary treatments have been developed whereas long term effective treatment is an open area of research. Examples are epilepsy and Alzheimer's disease. Amongst such disorders, epileptic seizure is affecting the life quality of many people in UK and worldwide [Institute of Medicine (US) Committee on the Public Health Dimensions *et al.*, 2012; McLaughlin *et al.*, 2008]. Seizure is a state of brain when a neural population starts to show abnormal electrical activity which causes unproductive movements and imbalances in a person [Kandel *et al.*, 2000]. The main cause of epilepsy and seizure are still unknown. It is only in very rare cases that death is caused by a seizure. However, the disorder can adversely affect the life quality of patients.

More than 40 different types of seizures have been identified. A small list of seizure types is given in Table 2.1.

Category	Sub-Category	Description
Partial (Focal)	Simple	Conciousness is not effected.
	Complex	Conciousness is impaired.
	Secondary General	Partial Seizure evolves to generalised seizure
Generalised	Absence	Conciousness is interrupted for a short while and slight involuntary muscle movements might be observed.
	Myoclonic	Jerky Muscle Movements for a short while.
	Colonic	a set of repeated myoclonic type seizure
	Tonic	Severe Muscle contraction
	Tonic-clonic	Tonic case followed by a clonic jerky muscle
	Atonic	Loss of motor control which causes the effected person to collapse.
Unclassified		Any other type of seizure not classified above.

Table 2.1: A number of different seizure types and their symptoms [Gastaut, 1970].

As mentioned earlier, abnormal electrical activity is observed during a seizure. This is continuation of earlier work of Bois-Reynmond (1818-1896) and Carlo Matteucci (1811 1868) where electrical activity of an injured tissue was recorded. Brain electrical activity was first recorded by Richard Caton (Liverpool, England) by placement of electrodes of a galvanometer on the scalp. This is known as the term EEG or in its longer format as Electroencephalogram since then [Gensini *et al.*, 2004; Pearce, 2001] (Electro is referring to the electrical activity, Encephlo is referring to signal diffusion).

Intracranial EEG is another form of brain electrical recording by use of electrodes placed on exposed surface of cerebral cortex [Lehnertz, 1999]. This is called iEEG in short. In this method, the artefacts included in EEG coming from the scalp are eliminated. Such artefacts can be caused by different reasons such as blinking or hand movements. There are other recoding types such as fMRI where a patient is required to be steady (Which is not the case for a seizure). For such constraints during the recording time, EEG has become one of the suitable recoding choices during the past years [Saeid Sanei, 2007].

Development of computational models is highly demanding for analysis of seizure dynamics. This is more obvious when complexity of brain structure and communication between neural population is taken into account. Commonly accepted models for presenting the electrical activities during seizure can give insight to the inner dynamics of the brain structure while a patient is going through a transition from a normal state into a seizure.

The epilepsy models can be divided into two main categories: Macroscopic models and detailed networks [Kramer & Cash, 2012]. One of the important aspects of a model is purpose of the model and its capability of presenting the targeted activity. Following early work of Wilson & Cowan [1972] macroscopic models are developed based on the concept of a mean field model. Mean field models take into account two main types of neural cells. Inhibitory cells and excitatory principal cells regardless of biophysiological characteristic of individual cells. Dynamics of a seizure in a large scale neural population can be better understood by use of a mean field model. On the other hand, in comparison to application of other multivariate auto-regressive (MVAR) models in estimation of functional connectivity such as previous work of Hesse *et al.* [2003]; Kaminski & Blinowska [1991]; Sameshima & Baccalá [1999], mean field models can present the seizure dynamics with lower computational complexity [Aram, 2011].

The downside of mean-field models is the missing characteristics of each biophysiological and individual neural cell characteristics. A good history on epilepsy modelling and comparison of previous work is given at Ullah & Schiff [2009]. Following the early work of Lopes da Silva *et al.* [1974], models have been developed for resting state EEG such as alpha rhythm. Further work have been carried out based on the bifurcation theory and use of nonlinear differential equations such

as Kramer & Cash [2012]; Marten *et al.* [2009a]; Wendling *et al.* [2001].

The model of Wendling *et al.* [2002] is capable of producing different types of EEG signals. Previous work of Marten *et al.* [2009b]; Suffczynski *et al.* [2004]; Wendling *et al.* [2001] are more focused on analysing the parameter changes based on the model and finally the Kramer *et al.* [2007] has used 14 differential equations to mimic the inhibitory and excitatory dynamics in cortex [Ullah & Schiff, 2009].

Considering that EEG recordings are obtained from the scalp, macroscopic model is the most appropriate model type to describe the underlying neural population activity. However, a realistic model would be impossible considering the complexity of underlying structure of neural field.

2.4 EEG Generation

The discovery of electrical activities in the brain goes back to 1875 by Richard Caton where electrical activity was observed on open brain in monkeys and rabbits [Bear *et al.*, 2007].

Later on, it was shown that the brain's electrical activity can be measured from human scalp.

The EEG signal is a result of addition of the EPSPs (Excitatory Postsynaptic Potential) and IPSPs (Inhibitory Postsynaptic Potential) of pyramidal neurons. Most inhibitory synapses happen at soma (neural cell core) while both excitatory and inhibitory synapses happen in dendrites [Harris & Weinberg, 2012]. Pyramidal neurons are oriented perpendicular to the surface of the cortex and the excitatory synapses are spatially separated from inhibitory synapses. These two features enable the EEG recordings [Mirowski *et al.*, 2008].

Pioneering work in analysing EEG data goes back to work of Lopes da Silva *et al.* [1974] and Freeman [2007] whose work led to proposal of models at resting state such as $\alpha-$ rhythm.

Analysing EEG recordings during an epileptic seizure can reflect on underlying physiological dynamics [Malagarriga *et al.*, 2015]. This is expected to be obtained in the parameter space of a neural model. By parameter space, it is refereed to a trajectory of values that model parameters go through during the period of an pre-seizure to seizure and seizure to post-seizure [Nevado-Holgado *et al.*, 2012a].

2.5 Computational Neural Models

Mathematical models can provide a functional description of the underlying dynamics of the electrical activity recorded in electro-physiological data. Considering the accumulation of the neuron cells, the neural electrical activity recorded via EEG measurement presents a large scale neural population [Panzeri *et al.*, 2015]. Hence, neural mass and neural field modelling can be used to describe the measurements.

Rest and sleep states can be named as good examples of self-organised large scale neural activities [Buzsáki, 2006]. Properties of the brain neural activity suggest a natural connectivity between local areas as well as connections between cortical and subcortical components. The grey matter of the brain is the home for cortical neurons whose connections do not leave the grey matter. Such connections are considered to be unmyelinated in most of the cases and they can extend up to $1cm$ (homogeneous) [Ben-Tal & Smith, 2008]. This type of connections are myelinated and it is spatially variant [Sanz-Leon *et al.*, 2015; Spiegler *et al.*, 2011] (heterogeneous).

It should be noted that local and non-local sources are involved in forming the neural field dynamics. Heterogeneous connections have been found beneficial in different cases such as calcium wave propagation, synchronised coupled excitable units to an external input and Respiratory rhythm generation.

Macroscopic models describe large neural population behaviours and they can be used to clarify brain functionalities locally. At mesoscopic models, neural activity is studied at the level of micro columns and cortical columns [Malagarriga *et al.*, 2015]. At this level, the model will describe electrical activity of a neural population considering the characteristics of a single neuron. It should be noted that in this case, computational neural units have been considered rather than single neural units. Hence, the spatial extension of each unit is about a few hundred micrometres [Aram, 2011; Markounikau *et al.*, 2010].

Such mathematical models can be presented by a set of ODEs such as Nevado-Holgado *et al.* [2012b], Integro-Differential Equations (IDE) or Partial Differential Equations (PDE). Typically, ODEs are used where a macroscopic computational model is used to describe the neural behaviours. One of the well-known partial

systems is given by Hodgkin and Huxley Hodgkin & Huxley [1952].

The main difference between ODEs and PDEs is that the latter one prescribes rate of change of a function with respect to two or more independent variables such as time and space where as ODEs are used in case of a function derivative to time [Mascagni & Sherman, 1989]

Each type of mathematical model is used to present specific features of the brain dynamics but in general, all these models have a common point in describing underlying dynamics by parametrising its functionalities. Fundamental mechanism of neural activities at different spatial scales can be presented by a mathematical model. Hence, EEG recordings during a specific activity can be analysed and parametrised. Some of the premier work in neural modelling can be mentioned as Lopes da Silva *et al.* [1974]; Nunez [1974]; Wright & Liley [1996]. Two important types of mean neural field models can be named as Wilson & Cowan and Amari type models [Coombes *et al.*, 2007].

An interesting research area is developing frameworks that can obtain repeating features or pattern of model parameters when brain electrical activities are analysed [Van Veen *et al.*, 1997]. In order to apply a systematic approach on analysing the signals such as estimation framework, it is important to develop neural field models that can produce the main features of interest similar to features observed in brain electrical activity observations [Pinotsis *et al.*, 2012]. Fitting models to data can reflect changes in the model parameters for a specific type of functional behaviour. A change in pattern of model parameters that corresponds to a neural population behaviour in response to a specific task can lead to suggestions on developing better treatments or identification and prediction of brain disorders [Falk *et al.*, 2012; Fürtinger *et al.*, 2014].

A brief introduction is given on neural modelling in the next section.

2.5.1 Neural Field Model

In case of neural field modelling, the synapses between individual neurons are described by effective averages called as mean fields. This is achieved by use of firing rate that encapsulates the properties of individual neurons. the firing rate function is chosen as a sigmoid function [Coombes, 2010]. The spatial domain

(Ω) over which this process happens results in neural field model. Formulation of dynamics at macroscopic level cannot give insight to characteristics of individual neurons. One mathematical approach to formulating the mesoscopic cortical neural dynamics is given by Wilson & Cowan and Amari [Liley *et al.*, 2011].

2.5.2 Wilson & Cowan Model

Wilson & Cowan model describes the neural dynamics in a population of neurons based on inhibitory and excitatory neurons. Mean field models such as Wilson & Cowan [1972] produce similar signals to those observed from brain electrical activities in EEGs or MEGs. Wilson & Cowan [1972] used a nonlinear model to describe the dynamics of the spatially localised excitatory and inhibitory sub-populations [Moran *et al.*, 2013].

Wilson & Cowan developed a nonlinear model to describe the dynamics of spatially localised excitatory and inhibitory sub-populations in 1970s. His earlier model is altered to include the homogeneously distributed neural population [Wilson & Cowan, 1973].

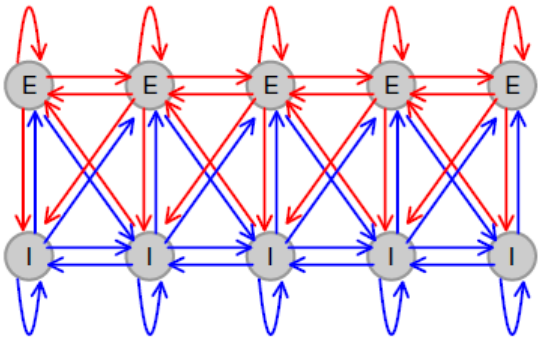

Figure 2.6: The characteristic connectivity of 2D layer Wilson & Cowan model, E: Excitatory and I: Inhibitory, excitatory and inhibitory connections are highlighted by coloured arrows.

A two dimensional functionality was assumed for cortex and subcortical structures which are illustrated in Figure 2.6. Derivation for Wilson & Cowan equations is given here.

Derivation starts by assuming $E(r,t)$ as excitatory and $I(r,t)$ as inhibitory proportion of active neurons at time sample t and spatial location r. Mean rate of activation potentials received by excitatory neurons is given by spatial integration as

$$\int_{-\infty}^{+\infty} \varrho_e E(r', t - \frac{|r-r'|}{\vartheta_e})\omega_{ee}(r-r')dr' \tag{2.3}$$

$$\int_{+\infty}^{-\infty} \varrho_i I(r', t - \frac{|r-r'|}{\vartheta_i})\omega_{ie}(r-r')dr' \tag{2.4}$$

where ϑ_j presents the propagation velocity, ϱ_j is the tissue surface density, ω_{jk} is the connectivity between neurons in class k and class j. In other words, w_{jk} describes how two classes of neurons j and k are connected to each other. By subtracting expression (2.3) from (2.4) and taking into account the linear time-invariant of temporal summation in neurons, mean integrated excitation for excitatory neurons at spatial location r will be obtained as

$$\hat{v}_e(r,t) = \int_{-\infty}^{t} \left[\int_{-\infty}^{+\infty} \varrho_e E(r', t - \frac{|r-r'|}{\vartheta_e})\omega_{ee}(r-r')dr' - \right. \tag{2.5}$$

$$\left. \int_{-\infty}^{+\infty} \varrho_i I(r', t - \frac{|r-r'|}{\vartheta}_i)\omega_{ie}(r-r')dr' \right] h(t-t')dt'$$

Number of excitatory neurons over an element of space (Δ_r) that have not been activated in the time period of $t - t_r$ till t seconds can be described by

$$N_e(r,t) = \left[1 - \int_{t-t_r}^{t} E(r,t')dt' \varrho_e \Delta_r \right] \tag{2.6}$$

Hence, expected number of activated neurons for a time period of Δ_t at $t + t_d$ where t_d denotes the synaptic delay is given by

$$E(r, t+t_d)\varrho_e \Delta_r \Delta_t = N_e(r,t) f_e(\bar{v}_e(r,t))\Delta_t \tag{2.7}$$

where $f_e(.)$ is a sigmoid activation function. Substituting equation (2.5) and equation (2.6) into equation (2.7) will result in

$$E(r,t)\varrho_e\Delta_r\Delta_t = \left[1 - \int_{t-\tau_e}^{t} E(r,t')dt'\right]\varrho_e\Delta_r f_e\Bigg(\int_{-\infty}^{t}\left[\int_{-\infty}^{+\infty}\varrho_e E(r',t)\omega_{ee}(r-r')dr' - \int_{-\infty}^{+\infty}\varrho_i I(r',t)\omega_{ie}(r-r')dr'\right]h(t-t')dt'\Bigg)\Delta_t \tag{2.8}$$

Synaptic delay t_d and the propagation delay are very small and they can be neglected by assuming a sufficient fast conduction velocity. Following equations describe the convolution of E and I with postsynaptic response kernel by

$$\widetilde{E}(r,t) = \int_{-\infty}^{+\infty} E(r,t')h(t-t')dt' \Rightarrow E(r,t) = \tau\frac{\partial\widetilde{E}(r,t)}{\partial t} + \widetilde{E}(r,t) \tag{2.9}$$

$$\widetilde{I}(r,t) = \int_{-\infty}^{+\infty} I(r,t')h(t-t')dt' \tag{2.10}$$

For cortical excitatory neurons, the refractory time t_r is a very small value in comparison to the time constant τ, hence, it can be concluded that

$$\int_{t-t_r}^{t} E(r,t)dt' = \int_{t-t_r}^{t}\left[\tau\frac{\partial\widetilde{E}(r,t')}{\partial t'} + \widetilde{E}(r,t')\right]dt' \approx t_r\widetilde{E}(r,t) \tag{2.11}$$

By substituting equation (2.9) and approximation given in equation (2.11) in equation (2.8) and after rearranging and simplification, the final form of Wilson & Cowan neural field mode can be obtained as

$$\tau\frac{\partial\widetilde{E}(r,t)}{\partial t} = -\widetilde{E}(r,t) + \left[1 - t_r\widetilde{E}(r,t)\right]f_e\Bigg(\int_{-\infty}^{+\infty}\varrho_e\omega_{ee}(r-r')\widetilde{E}(r,t)dr'$$

$$- \int_{-\infty}^{+\infty} \varrho_i \omega_{ie}(r - r')\widetilde{I}(r,t)dr' \Bigg) \tag{2.12}$$

Similar derivation will yield the inhibitory layer as

$$\tau \frac{\partial \widetilde{I}(r,t)}{\partial t} = -\widetilde{I}(r,t) + \left[1 - t_r \widetilde{I}(r,t)\right] f_i \Bigg(\int_{-\infty}^{+\infty} \varrho_e \omega_{ei}(r - r')\widetilde{E}(r,t)dr'$$

$$- \int_{-\infty}^{+\infty} \varrho_i \omega_{ii}(r - r')\widetilde{I}(r,t)dr' \Bigg) \tag{2.13}$$

Above equations are valid based on the time wise condition that activities of $E(r,t)$ and $I(r,t)$ would be longer than the synaptic time constant [Wilson & Cowan, 1973].

2.5.3 Amari Type Model

Similar to model of Wilson & Cowan, Amari [1977] analysed the pattern formation of neural field by assuming the pattern formation to be in one dimensional space with a single layer of inhibitory and excitatory neurons. The neural field equations is given by:

$$\tau \frac{dv(r,t)}{\partial t} = -v(r,t) + \int_{\phi} \omega(r,r') f(v(r',t))dr' + u(r,t) + c \tag{2.14}$$

In equation (2.14), τ is the synaptic time constant and $v(r,t)$ is a spatiotemporal mean neural field. Firing rate function is given by $f(v(r',t))$. Firing rate function in this type of models (macroscopic) is used to encapsulate the neural characteristics in a small local neighbourhood, in this case, a Heaviside function.

$$f(v(r',t)) = \begin{cases} 1 & v(r't) > 0 \\ 0 & v(r',t) < 0 \end{cases} \tag{2.15}$$

Spatial connectivity kernel denoted by $\omega(r,r')$ presents excitatory and inhibitory behaviour for proximate connections and distant connections respec-

tively. In other words, it describes connectivity between neurons at two spatial locations r and r'. The spatial connectivity kernel can be parametrised as the sum of three Gaussian basis functions [Zhou *et al.*, 2009]. The kernel shape is considered (but not limited to) a Mexican hat function and an example of a Mexican hat function is presented in Figure 2.7.

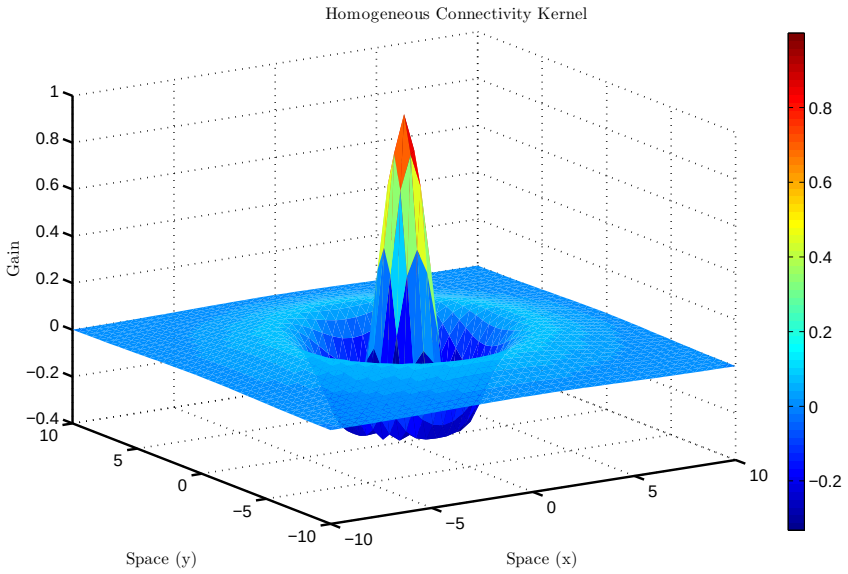

Figure 2.7: Two dimensional Mexican hat function.

For example the connectivity kernel can be parametrised as the sum of three Gaussian basis functions with different widths and gains. This will be applied and presented in next chapters. Finally, external input and constant resting potential are considered by $u(r,t)$ and c.

Each parameter at equation (2.14) is presented in more details on Table 5.1 in Chapter 3. It should be noted that neuron connections are always within a finite length and as a result the integration of the connectivity kernel should exist.

Heterogeneous connectivity in neural networks is discussed in Jirsa & McIntosh [2007]. It is indicated that the connections are ubiquitous in neural networks. Work of Jirsa *et al.* [2008] is more focused on the stability of homogeneous neural field in the presence of heterogeneous connections and its model of a heteroge-

neous connectivity is used in this thesis.

$$\psi_{het}(r, r') = \left[\begin{array}{cc} \mu_1\delta(r - r_1) & \mu_2\delta(r - r_2) \end{array} \right] \tag{2.16}$$

where μ_1 and μ_2 are connectivity gains for long-range connections with connections at locations r_1 and r_2 and δ is the impulse function. Heterogeneous connectivity is established as a two point connection in addition to a homogeneous field. Jirsa [2009] introduces the heterogeneous connectivity in one dimension whereas this is extended to two dimensions in the current thesis. This is achieved by modifying the heterogeneous connectivity equation which is explained in more details in Chapter 5.

Obviously in this case, the global dynamics of the neural field will depend on the local connectivity as well as long-range connections [Jirsa, 2009]. Considering that the connection is two-way, the gains are assumed to be equal on both paths.

There are only a few recent studies that study the effect of spatially invariant field as a result of heterogeneous connections. Qubbaj & Jirsa [2007] is one of the other studies that looks into effects of global connections on local dynamics of coupled brain areas. The studies of Jirsa [2009] suggests that space-time structure of brain coupling namely, coupling strength and time delay caused by the transition speed has specific contributions to spontaneous coherent fluctuations in the resting brain. Such correlations are reflected in Electroencephalography (EEG) recordings. The presence of heterogeneous connectivity and its effect on current estimation framework and neural field have been one of the novelties of the thesis. Neural connections are not limited to intracortical fibers with short ranges, but also long distance corticocortical connections through white matter has been reported [Leuze *et al.*, 2014]. The latter type of connection introduces spatially variant connectivity as the range of connection does not correspond to local homogeneous case [Pinotsis *et al.*, 2013]. In Jradeh [2010], the modelling of heterogeneous case has been studied in one dimension but it has been mentioned that the best geometry would be bi-dimensional. A bi-dimensional approach is considered in this thesis. This thesis is a follow up to previous work of Aram [2011] where homogeneous field is simulated by use of Amari type model and the homogeneous connectivity kernel gains have been estimated by the use of Un-

scented Kalman Filter. Hence, the earlier work have been developed in Matlab which have been used in the next chapters to introduce the novelties in this thesis [Aram, 2011]. Based on this, a modified Amari type model with homogeneous connectivity kernel will be given here.

2.6 Related Work

2.6.1 Homogeneous Connectivity

In different models, assumptions have been made to manage a programmatic approach to start with. Following the earlier work of Amari, the standard mathematical presentation of the mean field model is given by Aram [2011]

$$\frac{\partial v(r,t)}{\partial t} + \zeta v(r,t) = \int_{\Omega} \omega(r,r') f(v(r',t)) dr' + u(r,t) \tag{2.17}$$

$$f(v(r',t)) = \frac{1}{1 + exp(\varsigma(v_0 - v(r',t)))} \tag{2.18}$$

Synaptic kernel is assumed to a first order in Aram [2011]. This is extended to second order in this thesis. The second novelty is contributed by considering a spatially variant connectivity kernel and introducing heterogeneous connectivity. This is achieved by modifications to connectivity kernel which is presented by $\omega(r,r')$ in equation (2.17). Imaging of membrane voltage to EEG recordings can be described by an observation function that takes into account the spatial extent of sensor.

$$y_t(r) = \int_{\Omega} m(r-r') v_t(r') dr' + \varepsilon_t(r) \tag{2.19}$$

Equation (2.19) is used to generate observations from simulated mean field model where $m(r-r')$ is the observation kernel and $\varepsilon_t(r)$ denotes measurement noise and it has a multivariate normal distribution with zero mean and covariance matrix of $\Sigma_\varepsilon = \sigma_\varepsilon^2 I$ (I is the Identity matrix).

Five channels of observation is given in Figure 2.8. This is followed by Figure

2.9 that shows the dynamics in simulated neural field on 9 different time frames.

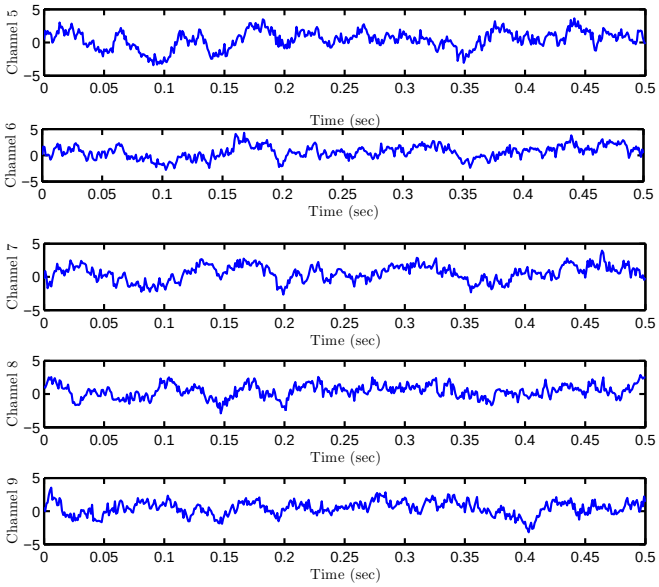

Figure 2.8: Five observation channels.

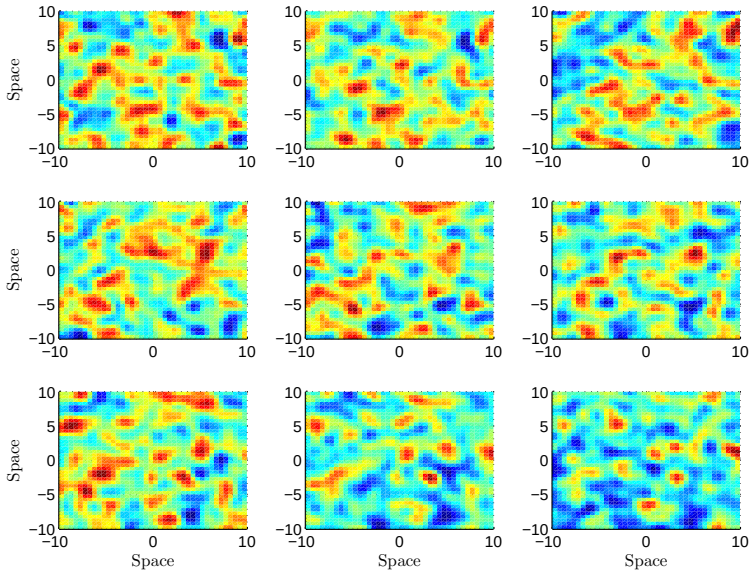

Figure 2.9: Simulated field at different time frames.

Standard form of model is given by equation (2.17) is discretised by use of Euler's method and then it is decomposed to a finite dimensional state-space model [Aram, 2011; Seeger, 2004]. The field decomposition is achieved by

$$v(r,t) \approx \phi_r^T x_t \tag{2.20}$$

The decomposed model is given by

$$x_{t+1} = \int_\Omega \Psi(r') f(\phi^T(r') x_t) dr' + \xi x_t + \Gamma^{-1} \int_\Omega \phi(r) e_t(r) dr \tag{2.21}$$

State-space presentation of the first order neural field model can be given by

$$x_{t+1} = Q(x_t) + e_t \tag{2.22}$$

$$y_t = C x_t + \varepsilon_t \tag{2.23}$$

State-space representation of the model promotes the use of Unscented Kalman Filter. A detailed step by step work out of the decomposition including the parameters' description, implementation of second order synaptic kernel and state-space presentation of Amari type model are given in Chapter 3 and Chapter 5. One can refer to relevant chapters for more information about the parameters in equations (2.20) to (2.23).

2.6.2 Heterogeneous Connectivity

During previous work of Aram [2011], neural field is assumed to be isotropic and homogeneous in a small neural network. For a larger neural population, possibility of long-range corticocortical connections with a patchy structure increases [Braitenberg & Schüz, 1991; Jirsa, 2004b]. It is intended to extend the earlier work to take into account the long-range connections for small network. Hence, propagation time delay can be neglected. However, time delay should be considered in larger networks.

In previous work such as Brackley & Turner [2009] has considered a one dimensional heterogeneous connectivity and a numerical approach is applied to

analyse the effect of heterogeneous connectivity in fluctuation of the neural field. In this thesis, the Amari type model will be expanded to include long-range connections in neuron populations [Pinotsis & Friston, 2011]. This will introduce the heterogeneous connectivity kernel in the model equations [Jirsa, 2002]. Following the earlier work of Jirsa *et al.* [2002]; Qubbaj & Jirsa [2007], the heterogeneous connectivity kernel can be decomposed into two individual parts as:

$$\Psi = \Psi_{hom} + \Psi_{het} \tag{2.24}$$

which presents the connectivity kernel as sum of the homogeneous connectivity kernel with the additional term that causes the spatial variant connectivity.

Focuses of the current work is the identification of heterogeneous connection and estimating the heterogeneous connectivity strength based on a systematic approach. In order to achieve this, the latter case will be approached first, results of which has been used in identifying the locations of possible heterogeneous connection.

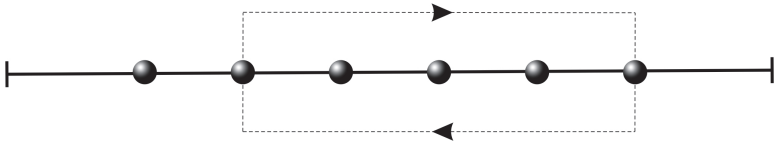

Figure 2.10: Heterogeneous forward and backward connection.

In a homogeneous field, connectivity kernel is assumed to be spatially invariant where as addition of long-range neural connections can lead to spatial variant connectivity kernel. Figure 2.10 shows an example of two-way long-range connection on a single dimension where the connection gain in forward and backward paths are equal. In this case, the heterogeneous connection is a two-way symmetric connection.

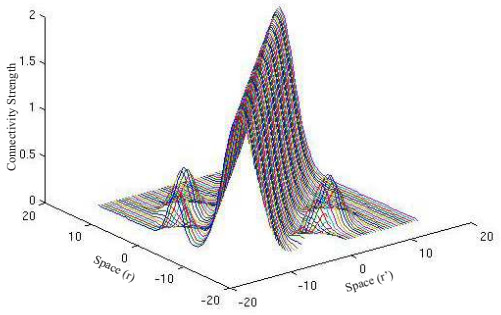

Figure 2.11: Shape of kernel with homogeneous and heterogeneous connectivity.

Figure 2.11 shows a heterogeneous connectivity kernel structure with two randomly selected long-range connections. It shows the structure of the 1D (one dimensional) long-range connection where connectivity of each point to its surrounding neighbourhood is plotted.

It is demonstrated that the addition of the incoming long-range connection, alters the homogeneous connectivity kernel shape. This is a graphical presentation of equation (2.24) [Jirsa *et al.*, 2008].

2.7 Introduction to Kalman Filtering

The standard Kalman filter is a recursive way of solving optimal filtering problem that can be applied to state-space presentation of a linear dynamical system. In Kalman filter each updated state at time t is obtained by taking into account the previous estimates at $t-1$ and the new inputs and measurements. This feature makes Kalman filter more efficient computationally as there is no need to include all of the past observed data.

Mathematical algorithm of Kalman filter is given by Haykin [2004]; Kalman [1960], one can also study the derivation of the Kalman filter in Julier & Uhlmann [1996, 1997]; Julier *et al.* [1995]. The state-space presentation plays an important role in this regard. Indeed, a state x_t presentation of a system gives the minimal set of variables to describe the dynamics of the system. In other words, the state values on each time step is the smallest set of data that is required to predict its

behaviour on the next time frame. It is assumed that the state x_t is unknown and a set of observations at time frame t is used for its estimation. The observations is denoted by y_t.

The state-space presentation of the process is given by:

$$x_{t+1} = F_{t+1,t}x_t + w_t \tag{2.25}$$

Matrix $F_{t+1,t}$ is called the transition matrix. w_t denotes the process transition noise. Subscript t denotes discrete time frame (Used for indexing, such that $t+1$ is the next time frame).

The observation y_t is given by

$$y_t = H_t x_t + v_t \tag{2.26}$$

where H_t is the measurement matrix. Measurement noise is given by v_t and w_t is the process noise.

The Kalman filter solution can be described as use of all observations $[y_1, .., y_N]$ to find the minimum mean-square error estimate of the state x_i where N is an index for time.

Depending on the value of i in x_i as $i = N, i > N, 1 \leq i < N$, it is a filtering, prediction and smoothing problem respectively.

Summary of the Kalman filter is given in Haykin [2004]. A smoother is used in this thesis. Consider a case where observations are given in a data set of N samples (observations are recorded at N points during the time). The time between each recording is considered as sampling time and it is assumed that sampling period is fixed throughout the thesis (non-variant temporal sampling length). Hence, the final time is given by index N. Smoothing is an offline process that means observations are available for the full period of time length. In other words, if $0 < j < N$, then at a given time step j, past and future data is available.

The estimation of states for past observations can be achieved by a filtering step whereas for estimation of future points, the estimation is initialised at time index N and it is computed backward. Hence, the problem is divided into forward and backward parts. Assume that $\hat{x}_j^f$ denotes the estimated states from forward run and $\hat{x}_j^b$ gives the estimated states in backward run. The next issue

to be explained is combining these two states to obtain a smoothed estimation of the state x over the full period of data. This will be part of the mathematical derivation of the Kalman filter. A good explanation of this is available in Haykin [2004].

The above mentioned estimation framework is based on linear state-space models. In previous work of Aram [2011] linear framework is modified for its applications on nonlinear neural field equations. For a nonlinear model, Extended Kalman filter (EKF) can be used [Jazwinski, 2007]. It is an extension of Kalman filtering using a linearisation process. The EKF method operates based on the first-order linearisation of the given nonlinear system which provides an approximate optimal solution for the nonlinear case. This may end up with large errors in estimation due to errors in weight estimation and covariance matrix. To overcome these issues, Unscented Kalman Filter can be used. Unscented Kalman filter is expected to have a superior performance to EKF. Significant contributions on Unscented Kalman filter was first given by Julier & Uhlmann [1996, 1997]; Julier *et al.* [1995] and further developed by Wan & Van Der Merwe [2000]; Wan *et al.* [1999]. One pioneer work on application of the UKF on neural models can be named as Schiff & Sauer [2008].

The UKF uses minimal set of sigma points that fully encapsulate the mean and covariance of the Gaussian random variables. After propagating through the nonlinear system equations, posterior mean and covariance are obtained accurately to the second order approximation [Van Der Merwe, 2004]. In comparison, the EKF only obtains the accuracy to the first order (Taylor series expansion). Hence, with a similar computational complexity, the UKF has a better performance with no need for explicit Jacobian calculations.

Chapter 3

Estimation of Second Order Amari Type Neural Field Model

3.1 Introduction

Synapses play an important role in communication of the neurons and in sending signals to non-neural cells (Ex.: Muscle fibres). Synapses offer a very fast transmission ranging from values smaller than 0.5 ms.

For simplicity, it is assumed that synapses have just excitatory or inhibitory nature. As an accepted approach in the community of the neuroscience, such an assumption reduces the complexities of synapses. A simple function to describe a synapse is the alpha function.

Considering the huge number of synapses in a decent-sized network, efficient simulation of the synaptic kernel is an important part of a model.

A generalised format of Alpha function leads to another synaptic model where Synaptic conductance is presented by sum of two exponentials. One for rising and one for decay phase. Assuming that the time constants of rise time and decay time are not equal, this model can be presented as two ODEs or as a second order system.

This model represents synaptic conductance effectively although it presents many of the underlying biological processes. More exponentials can be used to have a better fit of the synaptic dynamics but this will increase the computational

complexity and extraction of the time constants for each exponential out of noisy data will be a very challenging task.

In the following chapter. A second order synaptic kernel is adopted in the model and synthetic data is generated. Assuming that the time constants are known, the homogeneous connectivity kernel gains for the field is obtained by use of Unscented Rauch-Tung-Stiebel Smoother (URTSS).

It is expected that the use of second order synaptic kernel will enable the model to present wider range of neural activities.

3.2 Model Derivation with Second Order Synaptic Kernel

Following earlier discussions in the literature review, it is concluded that mean field models will be used for describing the neural network dynamics. As a starting point in this thesis, a small network is considered and this can be extended to larger networks. Use of a macroscopic model means that the properties of individual neurons is summed into a lumped gain in model (in this case, connectivity kernel gain) and this in turn will lead to estimation of less number of parameters. It is a challenging task to make a model that captures the required features in trade-off to its complexity.

As discussed earlier, the mean of presynaptic potentials leads to firing postsynaptic membrane potentials. This is described by firing rate function and mean of firing rates in this process can be described by a neural field model. Hence, neural field model will not capture the full properties and characteristics of individual neurons and it will give a mean of firing rate for the underlying neural population. This is of physiological importance as it gives a link to underlying dynamics such as complex spatial patterns; alpha rhythm [Lopes da Silva, 1991; Lopes da Silva *et al.*, 1974] and visual hallucinations and epileptic behaviour as part of neurodynamics, [David & Friston, 2003]. This will be seen in more details in developing the model in the following.

Assuming that r presents a two dimensional space by (x, y) coordinates and

that variable t denotes time in seconds, non-local interactions between cortical populations can be described by a weighted firing rate function as

$$g(r,t) = \int_{\Omega} \omega(r,r') f(v(r',t)) \partial r' \tag{3.1}$$

where $f(v(r',t))$ is the firing rate function for incoming interactions at spatial locations r' and time t. The term Ω refers to a spatial domain over which the neural field is defined where in this case it is a two dimensional space with coordinates x, y. Please note that for computational purposes, r' and r are from matrices of spatial locations. The firing rate function is considered as a nonlinear sigmoid function as given by equation (3.2) where ς is the slope of the firing rate function and it is given a value of 0.56 [Goodfellow *et al.*, 2011]. It should be noted that $\omega(r,r')$ is spatial connectivity kernel. It is assumed that the spatial connectivity kernel has Mexican hat shape. The Mexican hat function can be formed as a sum of three weighted Gaussian functions. The gains of the Gaussian functions will be assumed to be varying over time and the term spatial connectivity kernel will be called as connectivity kernel hereafter. The same assumption holds true in case of a two dimensional connectivity kernel which will be applied in this thesis. The firing rate function is the sigmoid,

$$f(v(r',t)) = \frac{1}{1 + exp(\varsigma(v_0 - v(r',t)))} \tag{3.2}$$

Postsynaptic membrane voltage ($v(r,t)$) at location r and time t can be described by

$$v(r,t) = \int_{-\infty}^{t} h(t-t') g(r,t') \partial t' \tag{3.3}$$

where function $h(t)$ denotes the postsynaptic kernel response. As part of the novelty in this chapter, a second order postsynaptic kernel is considered. A second order postsynaptic kernel will enable the possibility of considering a sharp rise time and a slower decaying time in presentation of a synaptic response. It is referred to the difference between two exponentials in literature as an extension

to the alpha function (discussed earlier in literature review). Hence, the following gives the synaptic kernel equation.

$$h(t) = k_1 u(t) e^{-\zeta_1 t} + k_2 u(t) e^{-\zeta_2 t}, \zeta_1 \neq \zeta_2 \tag{3.4}$$

where ζ_1 and ζ_2 denote rise and decay synaptic time constants, k_1 and k_2 are constants to be tuned in the next steps of the model derivation. The function $u(t)$ is a Heaviside step function.

Replacing equation (3.1) into equation (3.3) gives,

$$v(r,t) = \int_{-\infty}^{t} h(t-t') \int_{\Omega} \omega(r,r') f(v(r',t)) \partial r' \partial t' \tag{3.5}$$

3.2.1 Simplification by Use of Green's Function

To obtain a standard integro-differential format of the model from equation (3.5), application of Green's function will be used to simplify equation (3.5). One of the main properties of a Green's function is given by equation (3.6)

$$Dh(t) = \delta(t) \tag{3.6}$$

where $\delta(t)$ is the Dirac-delta function. Hence, it should be mentioned that function $h(t)$ is considered as a Green's function of a linear differential equation given by differential operator D [Bayin, 2006].

$$D = (\frac{\partial}{\partial t} + \zeta_1)(\frac{\partial}{\partial t} + \zeta_2) = \frac{\partial^2}{\partial t^2} + (\zeta_1 + \zeta_2)\frac{\partial}{\partial t} + \zeta_1 \zeta_2 \tag{3.7}$$

Parameters ζ_1 and ζ_2 are chosen as the rise and decaying synaptic time constants as given in the function $h(t)$ of equation (3.4). The property of the Green's function given in equation (3.6) is utilised to tune the weights k_1 and k_2 in equation (3.4).

Replacing function $h(t)$ into equation (3.6) will yield the following equations.

$$
\begin{aligned}
\tfrac{\partial h(t)}{\partial t} &= k_1\delta(t)e^{-\zeta_1 t} + k_2\delta(t)e^{-\zeta_2 t} - \zeta_1 k_1 e^{-\zeta_1 t}u(t) - k_2\zeta_2 e^{-\zeta_2 t}u(t) \\
\tfrac{\partial^2 h(t)}{\partial t^2} &= k_1\delta'(t)e^{-\zeta_1 t} - k_1\delta(t)\zeta_1 e^{-\zeta_1 t} + k_2\delta'(t)e^{-\zeta_2 t} - k_2\zeta_2\delta(t)e^{-\zeta_2 t} \\
&\quad -\zeta_1 k_1\delta(t)e^{-\zeta_1 t} + \zeta_1^2 k_1 e^{-\zeta_1 t}u(t) - k_2\zeta_2 e^{-\zeta_2 t}\delta(t) \\
(\zeta_1+\zeta_2)\tfrac{\partial h(t)}{\partial t} &= k_1\zeta_1\delta(t)e^{-\zeta_1 t} + k_2\delta(t)\zeta_1 e^{-\zeta_2 t} - k_1\zeta_1^2 e^{-\zeta_1 t}u(t) - k_2\zeta_2\zeta_1 e^{-\zeta_2 t}u(t) \\
&\quad +k_1\zeta_2\delta(t)e^{-\zeta_1 t} + k_2\zeta_2\delta(t)e^{-\zeta_2 t} - \zeta_1\zeta_2 k_1 e^{-\zeta_1 t}u(t) - k_2\zeta_2^2 e^{-\zeta_2 t}u(t)
\end{aligned}
$$

$$
\begin{aligned}
(\tfrac{\partial^2}{\partial t^2} + (\zeta_1+\zeta_2)\tfrac{\partial}{\partial t} + \zeta_1\zeta_2)h(t) &= k_1\delta'(t)e^{-\zeta_1 t} + k_2\delta'(t)e^{-\zeta_2 t} - k_1\zeta_1\delta(t)e^{-\zeta_1 t} \\
&\quad -k_2\zeta_2 e^{-\zeta_2 t}\delta(t) + k_2\zeta_1 e^{-\zeta_2 t}\delta(t) + k_1\zeta_2 e^{-\zeta_1 t}\delta(t)
\end{aligned}
$$

Considering that the Dirac-delta function is only non-zero at $t = 0$, it can be concluded that synaptic kernel response $h(t)$ exhibits the Green's function property with the following assumptions

$$k_1 = -k_2 \tag{3.8}$$

$$k_1 = \frac{1}{2(\zeta_2 - \zeta_1)} \tag{3.9}$$

$$h(t) = \frac{1}{2(\zeta_2 - \zeta_1)}(e^{-\zeta_1 t} - e^{-\zeta_2 t})u(t) \tag{3.10}$$

Also, considering that

$$\int_0^\infty h(t)\partial t = 1 \tag{3.11}$$

$$\Rightarrow \int_0^\infty \frac{1}{2(\zeta_2-\zeta_1)}(e^{-\zeta_1 t} - e^{-\zeta_2 t})\partial t = \frac{1}{2(\zeta_2-\zeta_1)} \int_0^\infty e^{-\zeta_1 t}\partial t - \frac{1}{2(\zeta_2-\zeta_1)} \int_0^\infty e^{-\zeta_2 t}\partial t$$

$$= \frac{1}{2(\zeta_2-\zeta_1)}(\frac{1}{\zeta_1} - \frac{1}{\zeta_2})$$

$$= \frac{1}{2\zeta_1\zeta_2}$$

Hence, a weight of $\eta = \zeta_1\zeta_2$ should be multiplied to the synaptic response kernel to compensate for the mismatch at integration of $h(t)$. This is considered in equation (3.13). The final equation for synaptic response is also inspired by previous work of Marten *et al.* [2009a]; Roth [2009]. Multiplying both sides of equation (3.3) by the linear differential operator D will give;

$$Dv(r,t) = D(h * g)(r,t) \tag{3.12}$$

where the sign $*$ denotes convolution operator. This can be simplified based on the property of the Green's function given by equation (3.6).

$$Dv(r,t) = \eta g(r,t) \tag{3.13}$$

The linear operator D is replaced in equation (3.13). Expanding the brackets gives the standard form of the model in equation (3.14).

$$(\frac{\partial^2}{\partial t^2} + (\zeta_1 + \zeta_2)\frac{\partial}{\partial t} + \zeta_1\zeta_2)v(r,t) = \eta g(r,t) \tag{3.14}$$

$$\frac{\partial^2 v(r,t)}{\partial t^2} + (\zeta_1 + \zeta_2)\frac{\partial v(r,t)}{\partial t} + \zeta_1\zeta_2 v(r,t) = \eta g(r,t) \tag{3.15}$$

$$g(r,t) = \int_\Omega \omega(r,r')f(v(r',t))\partial r'$$

3.2.2 Discretisation

The second order model derived in equation (3.15) can be converted to an equivalent system of two first order ODE [Strogatz, 1994].

$$\ddot{v}(r,t) + (\zeta_1 + \zeta_2)\dot{v}(r,t) + \zeta_1\zeta_2 v(r,t) = \zeta_2\zeta_1 g(r,t) \tag{3.16}$$

$$v_1(r,t) = v(r,t) \tag{3.17}$$

By assumption that $v_1(r,t)$ is the same as the neural field denoted by $v(r,t)$, a second variable can be defined as the derivative of neural field by $v_2(r,t)$ as

$$v_2(r,t) = \frac{\partial v_1(r,t)}{\partial t} \tag{3.18}$$

$$\frac{\partial v_2(r,t)}{\partial t} + (\zeta_1 + \zeta_2)v_2(r,t) + (\zeta_1\zeta_2)v_1(r,t) = \zeta_2\zeta_1 g(r,t) \tag{3.19}$$

Equation (3.18) and equation (3.19) can be approximated by first order Euler's method that will give the standard form of integro-difference neural field model by the following set of equations (3.23).

$$\frac{\partial v_1(r)}{\partial t} = \frac{v_1^{t+1}(r) - v_1^t(r)}{T_s} \tag{3.20}$$

$$\frac{v_2^{t+1}(r) - v_2^t(r)}{T_s} + (\zeta_1 + \zeta_2)v_2^t(r) + (\zeta_1\zeta_2)v_1^t(r) = \zeta_2\zeta_1 g^t(r) \tag{3.21}$$

$$v_2^t(r) = \frac{v_1^{t+1}(r) - v_1^t(r)}{T_s} \Rightarrow v_1^{t+1}(r) = v_1^t(r) + T_s v_2^t(r) \tag{3.22}$$

where T_s is sampling time period. Hence, the parameter t presents an index in time and the next time step is given by $t+1$. Sampling time is assumed to be ten times smaller than the faster time constant (rising time). This will assure that the effects of the smaller synaptic time constant are captured in the approximated model equation given here

$$v_1^{t+1}(r) = T_s v_2^t(r) + v_1^t(r) \tag{3.23}$$

$$v_2^{t+1}(r) - v_2^t(r) + (\zeta_1 + \zeta_2)T_s v_2^t(r) + \zeta_1\zeta_2 T_s v_1^t(r) = T_s\zeta_2\zeta_1 g^t(r)$$

$$g^t(r) = \int_\Omega \omega(r,r')f(v_1^t(r'))\partial r'$$

3.2.3 Addition of Noise and Disturbance

An independent and identically distributed disturbance signal is introduced by addition of term $e_t(r)$ ($e_t(r) \sim GP(0, \gamma(r - r'))$) to take into account unmodeled neighbourhood inputs and uncertainties in the model.

$$v_1^{t+1}(r) = T_s v_2^t(r) + v_1^t(r) \tag{3.24}$$

$$v_2^{t+1}(r) = \xi_2 v_2^t(r) - \xi_1 v_1^t(r) + \xi_1 g(r,t) + e_t(r) \tag{3.25}$$

where $\xi_1 = T_s\zeta_1\zeta_2$ and $\xi_2 = 1 - (\zeta_1 + \zeta_2)T_s$.

A simple replacement of equation (3.25) into equation (3.24) shows that the disturbance will be multiplied by the sampling time T_s. Hence, the disturbance gain is set to a large enough value to compensate for the product of the sampling time with the disturbance. This will assure the effective addition of the disturbance to the model. It can be concluded that

$$v_2^{t+1}(r) = T_s\xi_1 \int_\Omega \omega(r,r') f(v_1^t(r'))\partial r' + \xi_2 v_2^t(r) - \xi_1 v_1^t(r) + e_t(r) \tag{3.26}$$

$$v_1^{t+1}(r) = T_s v_2^t(r) + v_1^t(r) \tag{3.27}$$

The addition of the measurement noise will result in the observation equation to be defined as

$$y^t(r_n) = \int_\Omega m(r_n - r')v_1^t(r')\partial r' + \varepsilon^t(r_n) \tag{3.28}$$

where $m(r-r')$ is an observation kernel of a sensor at the location r_n, $n = 1, ..., n_y$ to be sensor index with n_y as total number of sensors. The term for noise, $\varepsilon^t(r_n) \sim N(0, \Sigma_\varepsilon)$, denotes a multivariate normal distribution with mean zero and the covariance matrix $\Sigma_\varepsilon = \sigma_\varepsilon^2 I$ where I is the identity matrix.

3.2.4 Model Reduction

Neural field is decomposed in order to cooperate standard estimation techniques. Field decomposition is achieved by use of Gaussian basis functions. This will allow a finite-dimension state vector representation and this facilitates the application of estimation methods such as UKF [Aram *et al.*, 2013; Dewar *et al.*, 2009]. The field decomposition is described by

$$v_1^t(r) \approx \phi^\top(r) x_1^t \tag{3.29}$$

$$v_2^t(r) \approx \phi^\top(r) x_2^t \tag{3.30}$$

where x_1^t, x_2^t are state vectors that scale the field basis functions $\phi^\top(r)$. The field basis as a function of space is given by equation (3.31).

$$\phi(r - r') = e^{(-\frac{(r-r')^\top (r-r')}{\sigma_\phi^2})} \tag{3.31}$$

where σ_ϕ is the basis function width parameter. Field basis vector, $\phi^\top(r)$, is defined as a functions of space and it is a vector with dimension of $n_x \times 1$ where n_x is the number of field basis functions. Following this, a new term will be defined as Γ as

$$\Gamma = \int_\Omega \phi(r)\phi^\top(r)\partial r \tag{3.32}$$

Equation (3.32) will be used for simplifying equations. Considering the definition of Γ, it is an invertible matrix with size of $n_x \times n_x$ where n_x is the number of basis functions. The connectivity kernel can also be decomposed as

$$\omega(r, r') = \psi^\top(r, r')\theta \tag{3.33}$$

where in this work $\psi(r, r')$ is a vector of three of Gaussian basis functions and θ is a vector of scaling parameters. In other words, the Mexican hat connectivity kernel is assumed to be sum of three Gaussian basis functions and each basis function is an element of ψ, i.e., $\psi_1(r - r'), \psi_2(r - r'), \psi_3(r - r')$ while θ holds the gains for each basis function. Later, two other parameters related to time constants will be incremented to vector of parameters θ.

Replacing the neural field decomposition and the connectivity kernel decomposition, given in equations (3.30) and 3.33, into set of equations (3.23) gives

$$\begin{aligned}
\phi^\top x_1^{t+1} &= \phi^\top x_1^t + T_s \phi^\top x_2^t \\
\phi^\top x_2^{t+1} &= -\xi_1 \phi^\top(r) x_1^t + \xi_2 \phi^\top(r') x_2^t + \xi_1 \int_\Omega \psi^\top f(\phi^\top(r') x_1^t) \partial r' \theta + e_t(r)
\end{aligned}$$

Multiplying both sides by $\phi(r)$ and applying integration, it can be concluded that

$$\begin{aligned}
\int_\Omega \phi(r)\phi^\top(r)\partial r x_1^{t+1} &= \int_\Omega \phi(r)\phi(r)^\top(r)\partial r x_1^t + T_s \int_\Omega \phi(r)\phi(r)^\top(r)\partial r x_2^t \\
\int_\Omega \phi(r)\phi(r)^\top(r)\partial r x_2^{t+1} &= -\xi_1 \int_\Omega \phi(r)\phi^\top \partial r x_1^t + \xi_2 \int_\Omega \phi(r)\phi(r)^\top(r)\partial r x_2^t \\
&\quad + \xi_1 \int_\Omega \phi(r) \int_\Omega \psi^\top(r - r') f(\phi^\top(r') x_1^t) \partial r' \partial r \theta \\
&\quad + \int_\Omega \phi(r) e_t(r) \partial r
\end{aligned}$$

Now by multiplying both sides by Γ^{-1}

$$x_1^{t+1} = x_1^t + T_s x_2^t \tag{3.34}$$

$$\begin{aligned}
x_2^{t+1} = -\xi_1 x_1^t + \xi_2 x_2^t + \xi_1 \Gamma^{-1} \int_\Omega \phi(r) \int_\Omega \psi^\top(r - r') f(\phi^\top(r') x_1^t) \partial r' \partial r \theta \\
+ \Gamma^{-1} \int_\Omega \phi(r) e^t(r) \partial r
\end{aligned} \tag{3.35}$$

It should be mentioned that Γ is a positive-definite matrix. This is true due to the definition of the Γ given by equation (3.32) [Golub & Van Loan, 2012].

Equation 3.35 can be simplified considering the isotropy of connectivity kernel

basis functions $\psi_1(r-r'), \psi_2(r-r')$ and $\psi_3(r-r')$ where

$$\psi_i(r-r') = \psi_i(2c_i + r' - r) \tag{3.36}$$

and c_i is the centre of ith connectivity kernel basis function. In this case, there are three basis functions i.e. $i = [123]$ in equation (3.36). As a result, simplification can be applied by use of the following expression

$$[\Psi(r')]_{:i} \equiv \Gamma^{-1} \int_{\Omega} \phi(r)\psi(2c_i + r' - r)\partial r \tag{3.37}$$

where $[\Psi(r')]_{:i}$ gives the ith column of $\Psi(r')$. Dimension of $[\Psi(r')]_{:i}$ is $n_x \times n_{sp}^2$ where n_x and n_{sp} are number of basis functions and total number of sampled spatial locations on each direction of spatial grid, respectively. Hence, parameter of $\Psi(r')$ is a three dimensional matrix. One last simplification can be applied to equation (3.35) before presenting the state-space form of the model. State disturbance can be defined as a linear function of $e^t(r)$ by

$$e^t \equiv \Gamma^{-1} \int_{\Omega} \phi(r)e^t(r)\partial r \tag{3.38}$$

As mentioned earlier, based on the definition of the matrix Γ in equation(3.32), it is an invertible matrix. Replacing this in equation (3.35) after above steps, the compact form of the model can be obtained as

$$X^{t+1} = Q(X^t) + E^t \tag{3.39}$$

where

$$Q(X^t) = \begin{bmatrix} 1 & T_s \\ -\xi_1 & \xi_2 \end{bmatrix} \begin{bmatrix} x_1^t \\ x_2^t \end{bmatrix} + \begin{bmatrix} 0 \\ \int_{\Omega} \xi_1 \Psi(r') f(\phi^\top x_1^t)\partial r' \theta \end{bmatrix} \tag{3.40}$$

$$X^t = \begin{bmatrix} x_1^t \\ x_2^t \end{bmatrix}, E^t = \begin{bmatrix} 0 \\ e^t \end{bmatrix} \tag{3.41}$$

In equation (3.40) and (3.41), 0 is a zero vector with dimension of $n_x \times 1$. This gives a state-space presentation of the model that facilitates the application of the estimation framework. Considering the nonlinear properties of Q(.), an estimation framework suitable for the nonlinear case can be applied.

State space representation of the observation equation can be obtained by substituting equation (3.30) into equation (3.28). This will result in

$$y^t = \int_{\Omega} m(r_n - r')\phi^{\top}(r')x_1^t \partial r' + \varepsilon^t$$

In compact form

$$y^t = \breve{C}X^t + \breve{E}^t \tag{3.42}$$

$$\breve{C} = \begin{bmatrix} C & 0 \end{bmatrix}, \breve{E}^t = \begin{bmatrix} \varepsilon^t \\ 0 \end{bmatrix}, C_{ij} = \int_{\Omega} m(r_i - r')\phi_j(r')\partial r' \tag{3.43}$$

where C is a matrix with dimension of $n_y \times n_y$ and n_y is number of sensors as given in table 3.1. Matrix $\breve{C}$ is combination of observation matrix C and matrix of zeros, 0 with dimension of $n_y \times n_x$. Hence, matrix $\breve{C}$ will have a dimension of $n_y \times 2n_x$.

A state-space presentation of the standard IDE form of the model is given by equations (3.43) and (3.39). In case of a linear $Q(.)$ function, standard Kalman filter could be used. However, the sigmoid activation function will cause nonlinearity in $Q(.)$ and this requires the application of UKF for obtaining the estimate of the states along with the use of a least squares method for estimation of the parameters [Aram, 2011].

Expected value of E^t will be required in the estimation process and it is given by

$$\langle E^t \rangle = \begin{bmatrix} 0 \\ \Gamma^{-1} \int_{\Omega} \phi \langle e^t(r) \rangle \partial r \end{bmatrix} = 0 \tag{3.44}$$

The covariance of E^t is given by Σ_E

$$\Sigma_E = \langle E^t E^{t\top} \rangle$$

$$= \begin{bmatrix} 0 & 0 \\ 0 & \Gamma^{-1} \int_\Omega \int_\Omega \phi(r)\gamma(r-r')\phi^\top(r')\partial r' \partial r \Gamma^{-\top} \end{bmatrix}$$

where 0 is a matrix of zeros with a dimension of $n_x^2 \times n_x^2$. As a result, dimension of matrix Σ_E will be given by $2n_x^2 \times 2n_x^2$. The estimation framework is presented in the next section.

3.3 Estimation

Estimation of states x_t, connectivity kernel gains θ and synaptic constants is explained. The estimation process consist of two iterative parts. An additive form of the Unscented Rauch-Tung-Striebel Smoother (URTSS) is applied for estimation of state vector followed by least squares algorithm for parameter estimation [Särkkä, 2006, 2010; Särkkä & Hartikainen, 2010].

In the following sections, parameter estimation and state estimation steps are modified to take into account the effects of a second order synaptic kernel.

3.3.1 Parameter Estimation

Although the model equation is nonlinear, the model is linear in parameters. Hence, least squares method can be applied as an optimal solution to find the connectivity kernel gains and the synaptic constants.

As a first step in forming the least squares parameter estimation, $q(.)$ is defined as

$$q(x_1^t) = \int_\Omega \Psi(r') f(\phi^\top(r') x_1^t) \partial r' \tag{3.45}$$

Matrix $q(.)$ has a dimension of $n_x \times n_T$ by n_θ where n_x is number of field basis functions and n_T is total number of time steps (i.e. for a simulation duration

of 0.5 seconds and a sampling frequency of $3KHz$; n_T will be equal to 1500). Number of parameters to be estimated is given by n_θ. In this case, there are five parameters to be estimated so the value of n_θ can be set to five.

At each iteration of the estimation framework (URTSS) or for the purpose of initialising the estimation framework, following set of equations can be used

$$x_2^{1,f} = q(\hat{x}_1^{0,f})\Theta - \xi_1\hat{x}_1^{0,f} + \xi_2\hat{x}_2^{0,f} + e^0 \tag{3.46}$$

$$x_2^{2,f} = q(\hat{x}_1^{1,f})\Theta - \xi_1\hat{x}_1^{1,f} + \xi_2\hat{x}_2^{1,f} + e^1 \tag{3.47}$$

$$. \tag{3.48}$$

$$. \tag{3.49}$$

$$. \tag{3.50}$$

$$x_2^{T,f} = q(\hat{x}_1^{T-1,f})\Theta - \xi_1\hat{x}_1^{T-1,f} + \xi_2\hat{x}_2^{T-1,f} + e^{T-1} \tag{3.51}$$

In compact form

$$Z = \breve{X}\varpi + e \tag{3.52}$$

where

$$Z = \begin{bmatrix} \hat{x}_2^{1,f} \\ \hat{x}_2^{2,f} \\ . \\ . \\ . \\ \hat{x}_2^{T,f} \end{bmatrix}, \breve{X} = \begin{bmatrix} q_1(\hat{x}_1^{0,f}) & q_2(\hat{x}_1^{0,f}) & q_3(\hat{x}_1^{0,f}) & -\hat{x}_1^{0,f} & \hat{x}_2^{0,f} \\ q_1(\hat{x}_1^{1,f}) & q_2(\hat{x}_1^{1,f}) & q_3(\hat{x}_1^{1,f}) & -\hat{x}_1^{1,f} & \hat{x}_2^{1,f} \\ . & . & . & . & \\ . & . & . & . & \\ . & . & . & . & \\ q_1(\hat{x}_1^{T-1,f}) & q_2(\hat{x}_1^{T-1,f}) & q_3(\hat{x}_1^{T-1,f}) & -\hat{x}_1^{T-1,f} & \hat{x}_2^{T-1,f} \end{bmatrix} \tag{3.53}$$

$$\varpi = \begin{bmatrix} \Theta_1 \\ \Theta_2 \\ \Theta_3 \\ \xi_1 \\ \xi_2 \end{bmatrix}, e = \begin{bmatrix} e_0 \\ e_1 \\ . \\ . \\ . \\ e_{T-1} \end{bmatrix} \tag{3.54}$$

The least squares parameter estimator is then given by equation [Ljung, 1998]

$$\hat{\varpi} = (\breve{X}^\top \breve{X})^{-1} \breve{X}^\top Z \tag{3.55}$$

3.3.2 State Estimation

URTSS is used to estimate the states. The URTSS is inclusive of two steps; an Unscented Kalman Filter (UKF) in a forward step (computing filtered estimates) followed by a backward step (computing smoothed states). These two steps (forward and backward steps) define the URTSS. The estimation is initialised by a bounded random initial state vector which is then propagated through least squares algorithm to obtain the initial parameter set. The estimation stops once the estimation has converged. Alternatively, algorithm can be run till a set number of iterations achieved [Haykin, 2004; Kalman, 1960; Sarkka, 2008].

3.3.2.1 Forward Iteration

Forward initialisation

$$\hat{x}_0, P_0 \tag{3.56}$$

Propagating the sigma points through state equations

$$\chi^{f-}_{i,t+1} = Q(\chi^{f}_{i,t}) \tag{3.57}$$

For calculation of the Sigma points (χ_i) by use of unscented transform follows

$$\chi_0 = \bar{x} \tag{3.58}$$

$$\chi_i = \bar{x} + (\sqrt{(n_x + \lambda)P_x})_{i-n_x}, i = 1, ..., n_x \tag{3.59}$$

$$\chi_i = \bar{x} - (\sqrt{(n_x + \lambda)P_x})_{i-n_x}, i = n_x + 1, ..., 2n_x \tag{3.60}$$

where $\bar{x}$ is the estimated states in the forward iteration or from the backward pass. Superscript i in $\sqrt{(n_x + \lambda)P_x}_{i-n_x}$ presents the i^{th} column of the scaled square root of the covariance matrix P_x and n_x is total number of field basis functions. Hence, there are $2n_x + 1$ sigma points.

The scaling parameter λ is given by

$$\lambda = \alpha^2(n_x + \kappa) - n_x \tag{3.61}$$

$$\kappa = 3 - n_x \tag{3.62}$$

The value of α is set to 10^{-3} considering the previous work of Aram *et al.* [2013]. Calculation of the predicted state and predicted covariance matrix is given by

$$\hat{x}^{f-}_{t+1} = \sum_{i=0}^{2n_x} W^m_i \chi^{f-}_{i,t+1} \tag{3.63}$$

$$P^{f-}_{t+1} = \sum_{2n_x}^{i=0} W^{(c)}_i (\chi^{f-}_{i,t+1} - \hat{x}^{f-}_{t+1})(\chi^{f-}_{i,t+1} - \hat{x}^{f-}_{t+1})^\top + \Sigma_e \tag{3.64}$$

where weights W can be obtained by

$$W_0^{(m)} = \frac{\lambda}{n_x + \lambda} \tag{3.65}$$

$$W_0^c = \frac{\lambda}{n_x + \lambda} + (1 - \alpha^2 + \beta) \tag{3.66}$$

$$W_i^{(m)} = W_i^{(c)} = \frac{1}{2(n_x + \lambda)}, i = 1, ..., 2n_x \tag{3.67}$$

Superscripts m and c denote the mean and covariance and β incorporates prior knowledge of the distribution of the state. β is set equal to two in this work. The value of β is chosen from Haykin [2001].

The Kalman filter gain, filtered states and the covariance matrix is obtained by

$$K_{t+1} = P_{t+1}^{f-} C^\top (C P_{t+1}^{f-} C^\top + \Sigma_\epsilon)^{-1} \tag{3.68}$$

$$\hat{x}_{t+1}^f = \hat{x_{t+1}^{f-}} + K_{t+1}(y_{t+1} - C\hat{x}_{t+1}^{f-}) \tag{3.69}$$

$$P_{t+1}^f = (I - K_{t+1}C)P_{t+1}^{f-} \tag{3.70}$$

$$M_{t+1}^f = \sum_{i=0}^{2n_x} W_i^c (\chi_{i,t}^f - \hat{x_t^f})(\chi_{i,t+1}^{f-} - \hat{x}_{t+1}^{f-})^\top \tag{3.71}$$

Matrix M^f is the cross-covariance matrix of the states and it is required for computing the smoother gain in backward pass.

3.3.2.2 Backward Pass

Here, a separate recursive backward smoothing pass is given for computing the corrections to the forward filtered results. The difference is that smoothed solution requires the whole measurement data while the filtered solution relies on the measurements obtained up to the time step k. Backward pass is initialised by

$$P_T^b = P_T^f, \hat{x}_T^b = \hat{x}_T^f$$

So, the backward iterations start from time step $T - 1$ towards the first time step. Smoother gain, the smoothed states and smoothed covariance matrix can

be updated by the following equations

$$S_t = M_{t+1}^f [P_{t+1}^{f-}]^{-1} \tag{3.72}$$

$$\hat{x}_t^b = \hat{x}_t^f + S_t[\hat{x_{t+1}^b} - \hat{x}_{t+1}^{f-}] \tag{3.73}$$

$$P_t^b = P_t^f + S_t[P_{t+1}^b - P_{t+1}^{f-}]S_t^\top \tag{3.74}$$

3.4 Results and Discussion

In this section, parameter and state estimation results are given for different scenarios. The first experiment is based on the Monte Carlo simulation for a set of parameters given in Table 3.1 where the variant parameters are fixed with the values in Table 3.2. Results of this experiment includes the simulated field at different time frames and distribution of estimated parameters. Another experiment is carried out by changing the parameters for sigmoid firing rate functions and effects of this on simulation result and estimation of parameters is given in next section. Finally, the connectivity kernel gains have been changed and the results of estimated kernel gains are provided.

In Table 3.1 parameter values marked as variant have been set in each Monte Carlo simulation. It does not mean that the parameter values change during a simulation but this is to indicate that the variable value is changed in different Monte Carlo simulation sets. Parameters are assumed to hold a fixed value during each individual Monte Carlo simulation. Considering the short run time of simulations, such an assumption is plausible biologically under a controlled environment for a patient. Simulation time is fixed at 0.5 second in the simulations presented here. Longer runs have been executed to check the outcome of the simulations. Neural field was not saturated and active dynamics such as variant peak locations and peak amplitudes are observed as expected.

Scaling parameter κ for the URTSS is set by $3 - n_x$ where n_x is number of basis functions [Julier *et al.*, 1995]. Parameter α is a small constant number set as 10^{-3} that indicates the spread of the sigma points [Haykin, 2004]. Our choice of number of sensors, n_s, and number of field bass functions,n_x, are motivated by Aram [2011]. Other parameters have been assumed as fixed values. For values of

Symbol	Parameter	Value	Unit
	Model		
	simulation duration (time)	0.5	sec
Δ	spatial discretisation step	0.5	mm
F_s	sampling frequency	3K	Hz
τ	synaptic time constant	$[166^{-1}, 56^{-1}]$	sec^{-1}
ς	slope of firing rate function	0.56	mV^{-1} spike sec^{-1}
f_{max}	maximum firing frequency	1	Hz
θ_{hom}	homogeneous connectivity kernel gains	variant	mV^{-1} $spike^{-1}$
$\sigma_{\psi_{hom}}$	homogeneous connectivity kernel width	variant	mm
n_y	number of sensors	14×14=196	Not Applicable
Δ_y	distance between adjacent sensors	1.5	mm
σ_m	observation Kernel width	0.9	mm
Σ_ε	observation noise variance	$0.1I_{n_y}$	mm^2
σ_y	disturbance spatial covariance width	1.3	mm
σ_d^2	disturbance variance	0.1	mV^2
	Reduced Model		
n_x	number of basis functions	9×9=81	Not applicable
Δ_ϕ	distance between field basis functions	2.5	mm
σ_ϕ	width of field basis functions	1.58	mm^2
	Estimation		
α	range of variation for sigma points	0.001	Not Applicable
β	prior knowledge of sigma points	2	Not Applicable
κ	scaling parameter	$3 - n_x$	Not Applicable
λ	scaling parameter	80.99	Not Applicable

Table 3.1: Table of Parameters

variant parameters, one can refer to their specified table of parameter values in Table 3.1.

3.4.1 Experiment 1: Monte Carlo Simulation with Fixed Parameters

Having simulated the neural field electrical activity using the model equations (3.35), the parameters have been estimated. The results of estimation and neural field simulation have been demonstrated in this section. An example of simulated field with parameters set in Table 3.2 is given in Figure 3.1 where its changing dynamics is displayed on nine different time frames.

Model			
Symbol	Parameter	Value	Unit
θ_{hom}	homogeneous connectivity kernel gain	$[4, -3.2, 0.2]$	$mV spike^{-1}$
v_0	firing threshold	3.2	mV
ζ	inverse synaptic time constant	$[55.3, 18.3]$	sec^{-1}

Table 3.2: Table of Parameters

Figure 3.1 also gives details about the amplitude of the neural field activities. It should be noted that neural field electrical activity is presented in millivolts (mv).

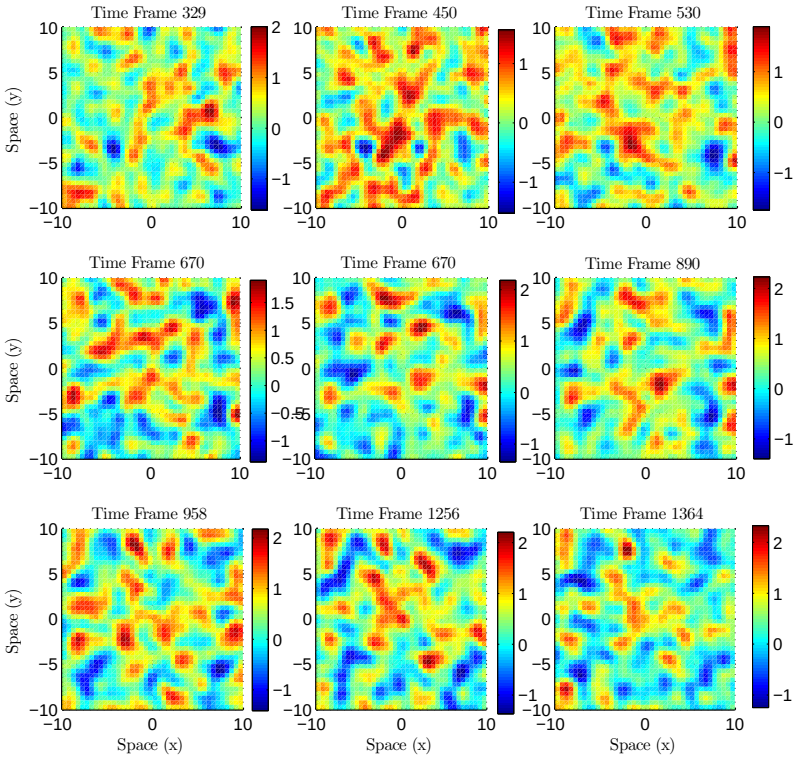

Figure 3.1: Simulated neural field at nine time frames.

Figure 3.1 demonstrates samples of simulated field at nine different time frames 329, 450, 530, 670, 720, 890, 958, 1256, 1364. This is to demonstrate the changing dynamics in the simulated field. It is demonstrated that simulated field is not saturated and changing dynamics can be observed in the field as the peaks' location and amplitude is varying in time.

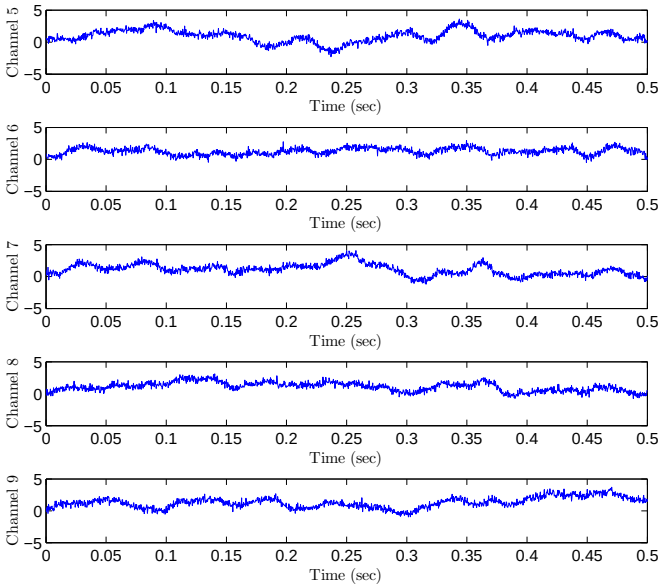

Figure 3.2: Plot of five observation channels.

Observations from five randomly selected channels are displayed in Figure 3.2. These observations are generated based on equation (3.28). It is demonstrated that observations are not saturated and there is no dead-zone in the observations.

The histogram plot of the estimated parameters for 150 Monte Carlo simulations is given in Figure 3.3 and Figure 3.4. The green line shows the true value of the parameters. Parameters θ_1, θ_2 and θ_3 are the gains used for forming the homogeneous Mexican hat connectivity kernel. Parameter ζ is the inverse of synaptic time constant.

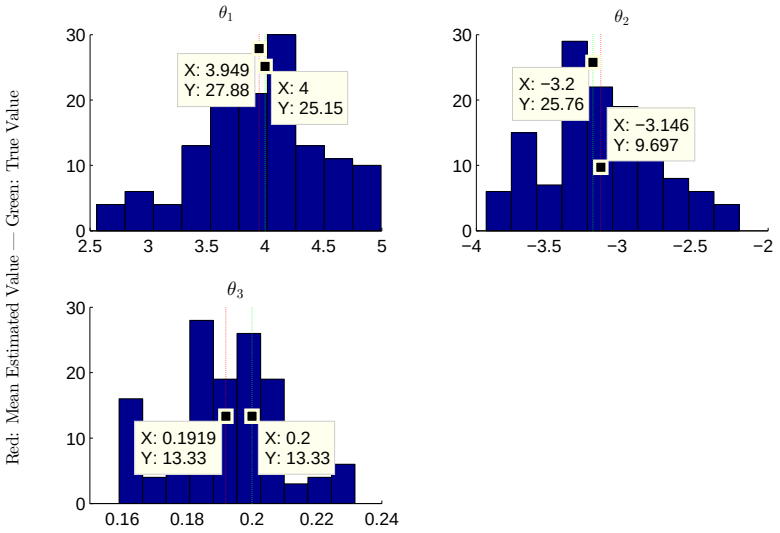

Figure 3.3: Histograms of estimated connectivity kernel gains from Monte Carlo simulation for $\theta_1, \theta_2, \theta_3$.

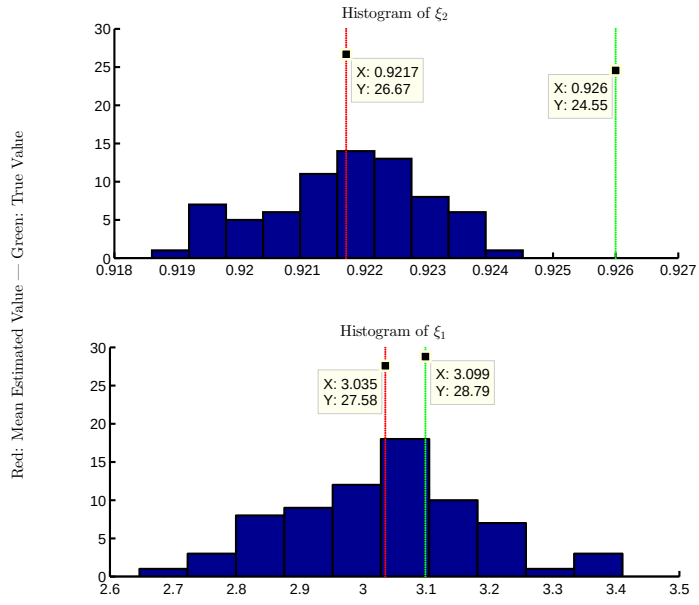

Figure 3.4: Histogram of estimated parameters from Monte Carlo simulation for ξ_1, ξ_2.

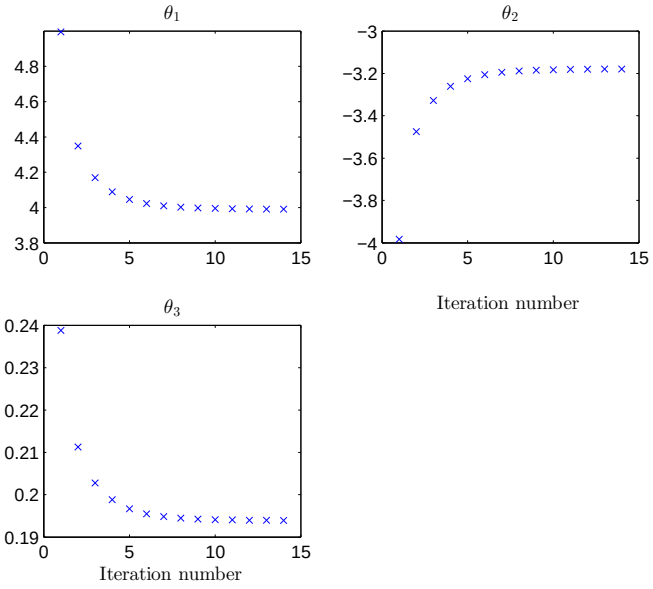

Figure 3.5: Convergence of estimation for connectivity kernel gains.

Figure 3.5 demonstrates the convergence of connectivity kernel gains $\theta_1, \theta_2, \theta_3$ over a single iteration of Monte Carlo simulation.

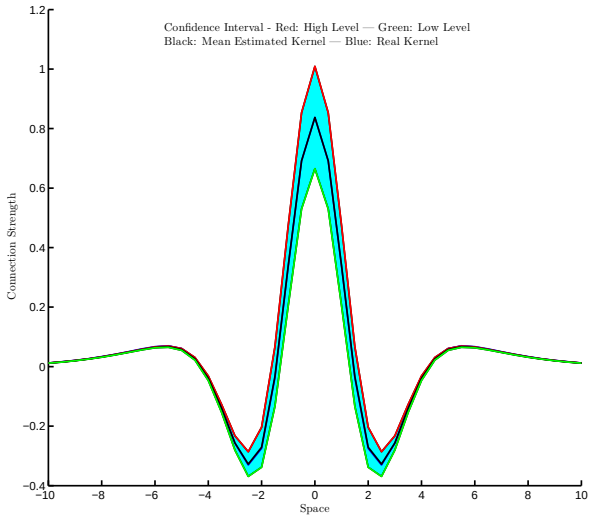

Figure 3.6: Confidence interval of estimated kernel over 150 Monte Carlo simulations.

Figure 3.6 exhibits the 95% confidence level for reconstructed kernels from

estimated connectivity kernel gains. Considering the random disturbance input to the model, a wide range of estimated gains is expected. The green kernel is the lower confidence interval and red coloured kernel is the upper limit of confidence interval. The black curve is the mean of estimated connectivity kernel over 150 Monte Carlo simulations. Real kernel is presented in blue which is covered with the estimated kernel due to a close fit.

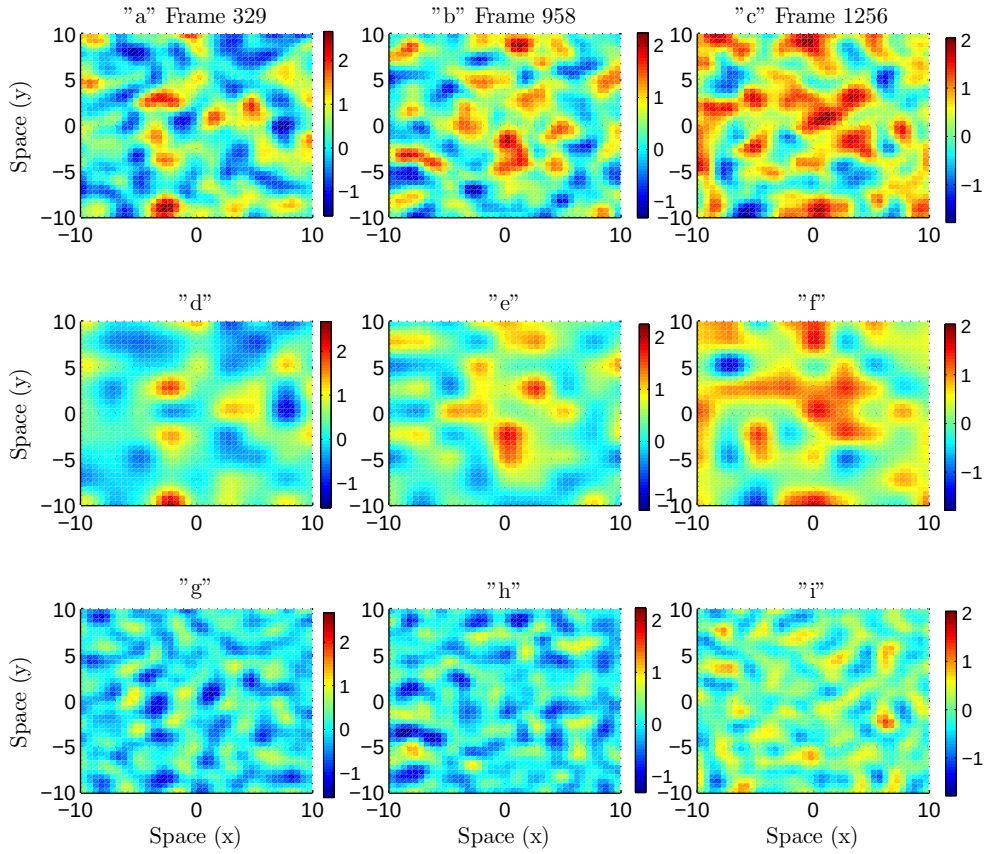

Figure 3.7: Plots "a,b,c" are simulated neural fields, plots "d,e,f" are reconstructed neural fields and plots "g,h,i" are the error in reconstructing the original neural fields.

Figure 3.7 illustrates true field at three different time frames (329, 958, 1265) at sub-plots "a", "b", "c". Estimated states and parameters are used to reconstruct the field based on equation (3.30). Reconstructed field for above time steps

are given in sub-plots “d”, “e”, “f”. It can be concluded that the general pattern of the true neural field is captured in estimated field (reconstructed field) which gives an insight to underlying neural field dynamics from sensor observations. It should be mentioned that at this stage, true field is synthetic and it is assumed that true field is available for comparison purposes. However, access to neural field dynamics is not possible and only patient recordings will be available in real applications. Therefore, the importance of this method is highlighted as it gives insight and possibility of having potential access to the underlying neural field dynamics. Sub-plots “g”, “h”, “i” show the difference between the estimated field and true field.

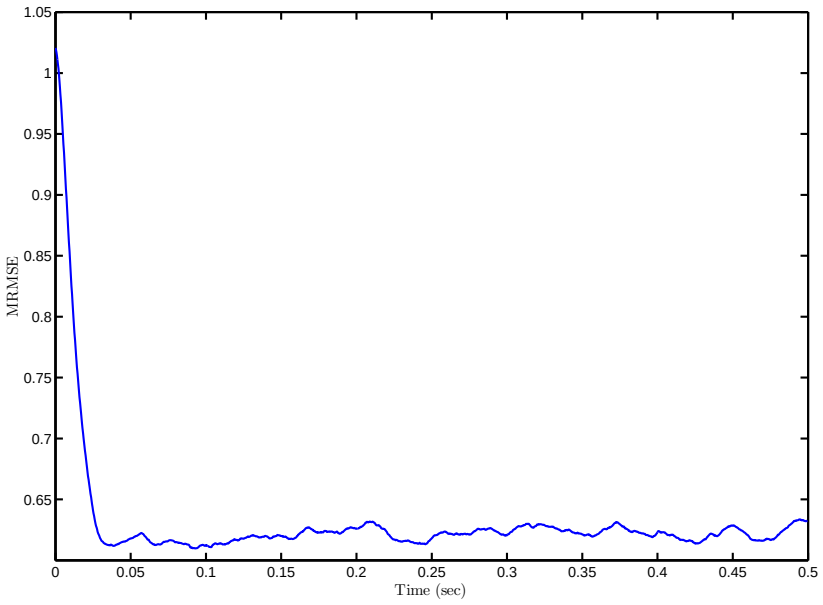

Figure 3.8: Mean Root Mean Squared Error.

Figure 3.8 shows MRMSE (Mean Root Mean Squared Error) for 150 Monte Carlo Simulations. At each time step, mean of squared error between estimated field and true field is obtained over space. Once this is done for each Monte Carlo simulation, MRMSE is obtained by applying mean root to the MSE over 150 Monte Carlo iterations. Hence, x-axis is time and y-axis is the MRMSE. The initial high value is due to the random initial states. This reduces significantly

after transition period.

3.4.2 Experiment 2: Different Firing Rate Parameters

Firing rate function is one of the important elements in the model as simulation and estimation results can be affected by changes to the activation function parameters. Hence, different case scenarios have been explored to check the effect of variation in activation function on estimated kernel gains. In the following section, it is demonstrated that for different firing rate thresholds [Laing *et al.*, 2012], the estimation results are stable and general connectivity kernel shape is obtained.

Model			
Symbol	Parameter	Value	Unit
θ_{hom}	homogeneous connectivity kernel gain	[4,-3.2,2]	$mVspike^{-1}$
ζ	inverse synaptic time constant	$[166, 56]$	sec^{-1}

Table 3.3: Model parameter values applied in different firing threshold experiments.

Firing rate function is varied based on the values in Table 3.4.

Case #	firing threshold	mean estimated values	unit
Case I	$\upsilon_0 = 1.8mV$	$\theta_1 = 3.51$	$mV spike^{-1}$
		$\theta_2 = -2.84$	$mV spike^{-1}$
		$\theta_3 = 0.18$	$mV spike^{-1}$
		$\xi_1 = 0.9217$	sec^{-1}
		$\xi_2 = 2.75$	sec^{-1}
Case II	$\upsilon_0 = 2.4mV$	$\theta_1 = 3.69$	$mV spike^{-1}$
		$\theta_2 = -2.97$	$mV spike^{-1}$
		$\theta_3 = 0.18$	$mV spike^{-1}$
		$\xi_1 = 0.9215$	sec^{-1}
		$\xi_2 = 2.89$	sec^{-1}
Case III	$\upsilon_0 = 2.8mV$	$\theta_1 = 3.84$	$mV spike^{-1}$
		$\theta_2 = -3.06$	$mV spike^{-1}$
		$\theta_3 = 0.18$	$mV spike^{-1}$
		$\xi_1 = 0.9218$	sec^{-1}
		$\xi_2 = 2.99$	sec^{-1}
Case IV	$\upsilon_0 = 3.8mV$	$\theta_1 = 4.27$	$mV spike^{-1}$
		$\theta_2 = -3.36$	$mV spike^{-1}$
		$\theta_3 = 0.199$	$mV spike^{-1}$
		$\xi_1 = 0.9216$	sec^{-1}
		$\xi_2 = 3.143$	sec^{-1}

Table 3.4: Firing threshold and mean of estimated parameters for each experiment.

Table 3.3 shows different firing thresholds for each case. The values are chosen for a range of firing thresholds given in similar work such as $\upsilon_0 = 1.8\ mV$ used in Aram [2011] to $\upsilon_0 = 6\ mv$ used in Wendling *et al.* [2001]. Hence, four different values of 1.8, 2.4, 2.8, 3.8 mv are selected and confidence interval of the estimation from 150 Monte Carlo Simulations are given in the following four figures (Figure 3.9 to Figure 3.12).

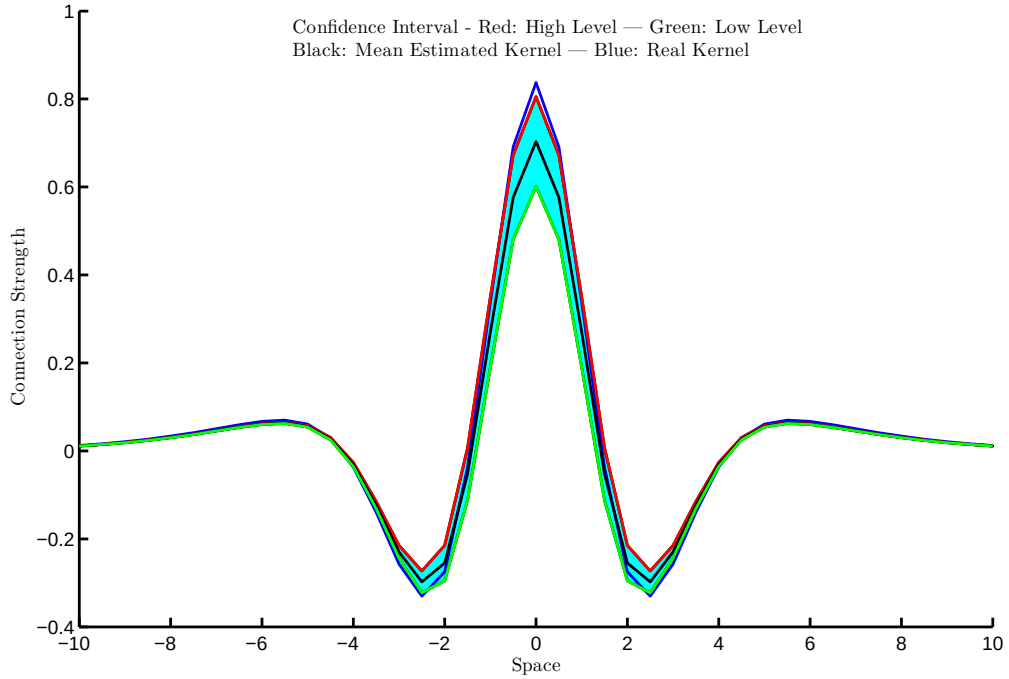

Figure 3.9: Estimated kernel with 95% confidence interval, firing threshold of $v_0 = 1.8\ mv$.

In Figure 3.9, firing threshold is set to 1.8 mv and the red kernel is reconstructed from the upper confidence level parameters and similarly green kernel is reconstructed based on parameters obtained from lower confidence level. Real kernel is given by blue kernel. and it is clear that the real inhibition curve falls inside of the 95% confidence interval. Black kernel shows the true kernel used in the simulations.

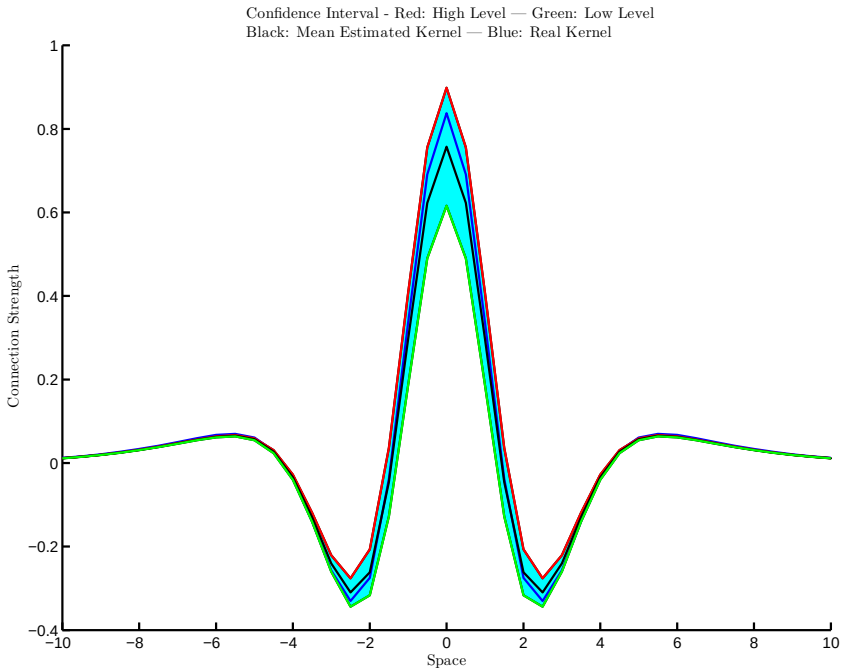

Figure 3.10: Estimated kernel with 95% confidence interval, firing threshold of $v_0 = 2.4\ mv$.

For $v_0 = 2.4\ mv$ the general shape of the connectivity kernel is estimated and mean of the estimated kernels from 150 Monte Carlo simulations are within the confidence interval. By this, it is meant that the mean of the estimated parameters are within 95% confidence interval. In comparison to Figure 3.9, increasing the threshold value has improved the estimation performance and this can be due the fact that firing rate function will operate in linear region for wider range of inputs and it will not saturate due to a small firing rate threshold.

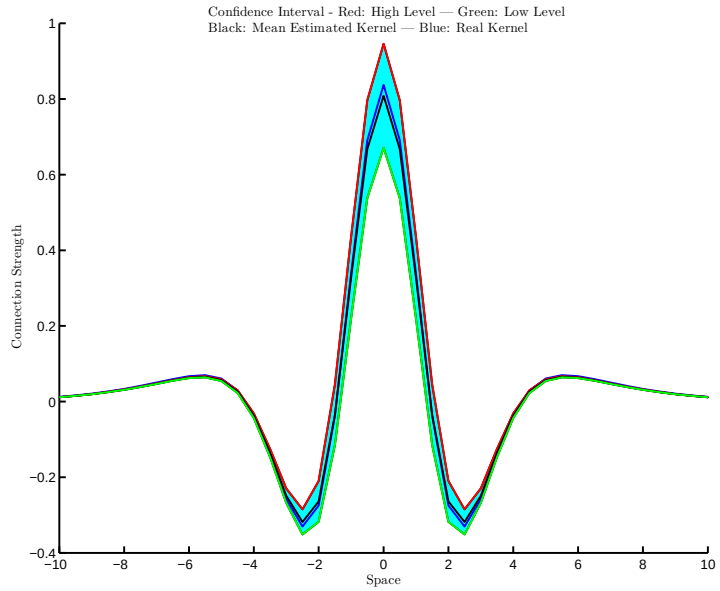

Figure 3.11: Estimated kernel with 95% confidence interval, firing threshold of $v_0 = 2.8\ mv$.

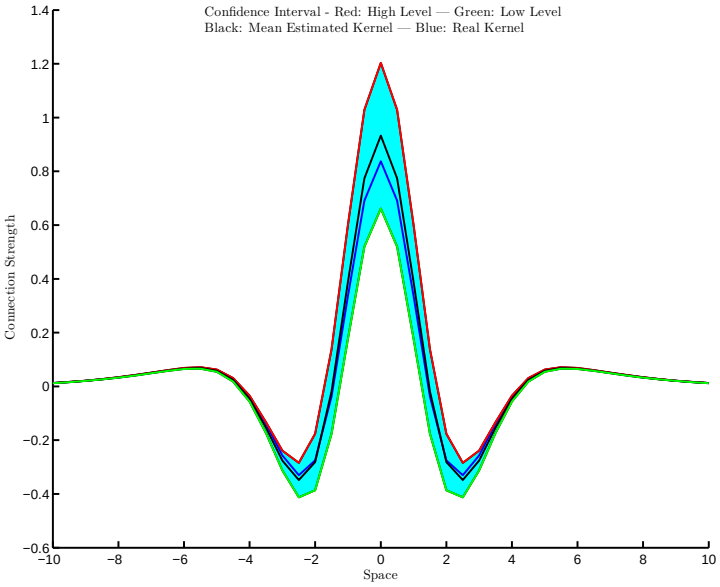

Figure 3.12: Estimated kernel with 95% confidence interval, firing threshold of $v_0 = 3.8\ mv$.

Figure 3.11 demonstrates a good performance in estimation of the true kernel with a firing threshold of 2.8 mv. In Figure 3.12, firing threshold is set to 3.8 mv and it is shown that increasing the firing rate threshold results in underestimating the parameters where the reconstructed kernel is below the true connectivity kernel. As mentioned in the earlier figures, mean of the estimated kernel from 150 Monte Carlo simulations is plotted in blue and true kernel is given in black. Green and red kernels are lower and upper confidence intervals, respectively.

In summary, sensitivity of the estimation framework to changes in the activation function is checked under four case scenarios and general shape of the connectivity kernel is obtained despite the changes in the firing threshold. It should be mentioned that the estimation will be invalid if the field is saturated, however, a saturated field is not plausible biologically and simulations shown on Figure 3.1 demonstrates that the dynamics in the simulated neural field are not saturated.

Chapter 4

Connectivity Estimation Using Intracranial EEG Data

4.1 Introduction

As mentioned earlier in the literature review, epilepsy is one of the brain disorders that affects the life quality of $600,000$ people each year in UK. This number gets bigger when it comes to a world wide scale. Traditional and current treatments are not focused on patient specific data and a patient specific treatment has become the interest of many researchers and scientists in the field of neuroscience [Kramer & Cash, 2012].

Despite advances in epilepsy treatments, cause of epilepsy in 6 out of 10 patients remains unknown [Action, 2015]. Based on reports from Epilepsy Action - epilepsy leading organisation in UK - one in 103 people is affected by epilepsy. EEG tests help the clinicians to diagnose and treat patients. Patient specific treatment is an open area of research and monitoring of the connectivity kernel gains can potentially provide insight to underlying neural field dynamics at different seizure stages [Aram *et al.*, 2013; Freestone *et al.*, 2011, 2013, 2014].

In this chapter, estimation framework and modified version of Amari type model developed in Chapter 3 will be used as a mechanism to understand the underlying dynamics observed during an epileptic seizure. It should be noted that, in this chapter, the term "data" is used to refer to epilepsy data.

This data set was obtained with informed consent from patients with ethics approval from St. Vincent's Hospital Melbourne Human Research Ethics Committee. Pre-processed data has been provided. The pre-processing usually involves filtering and re-referencing. Here data was re-referenced to a common-average reference (CAR) montage. The common average re-referencing acts as a spatial filter to determine changes from average activity at any location.

4.2 Epilepsy Data

It is a standard step prior to the surgery to implement intracranial electrodes to record iEEG to identify the epileptic tissue. The electrode placed on the temporal lobe and comprises a grid of 120 (8×15). The spacing along x and y directions is 0.5 and 1 centimetres respectively. The original sampling frequency during the recordings is $5KHz$. Data is down sampled from $5KHz$ to $1KHz$. This has the advantage of reducing the size of the data while not affecting the connectivity estimation. The data characteristics are also summarised in Table 4.1. The full length of data is divided to three different seizure stages, namely, pre-seizure, seizure and post-seizure.

Epilepsy Data		
recording time	669	seconds
number of sensors	8×15=120	N.A
sensor spacing	$[1, 0.5]$	cm
pre-seizure duration	300	seconds
seizure duration	69	seconds
post-seizure duration	300	seconds

Table 4.1: Characteristics of the iEEG recordings.

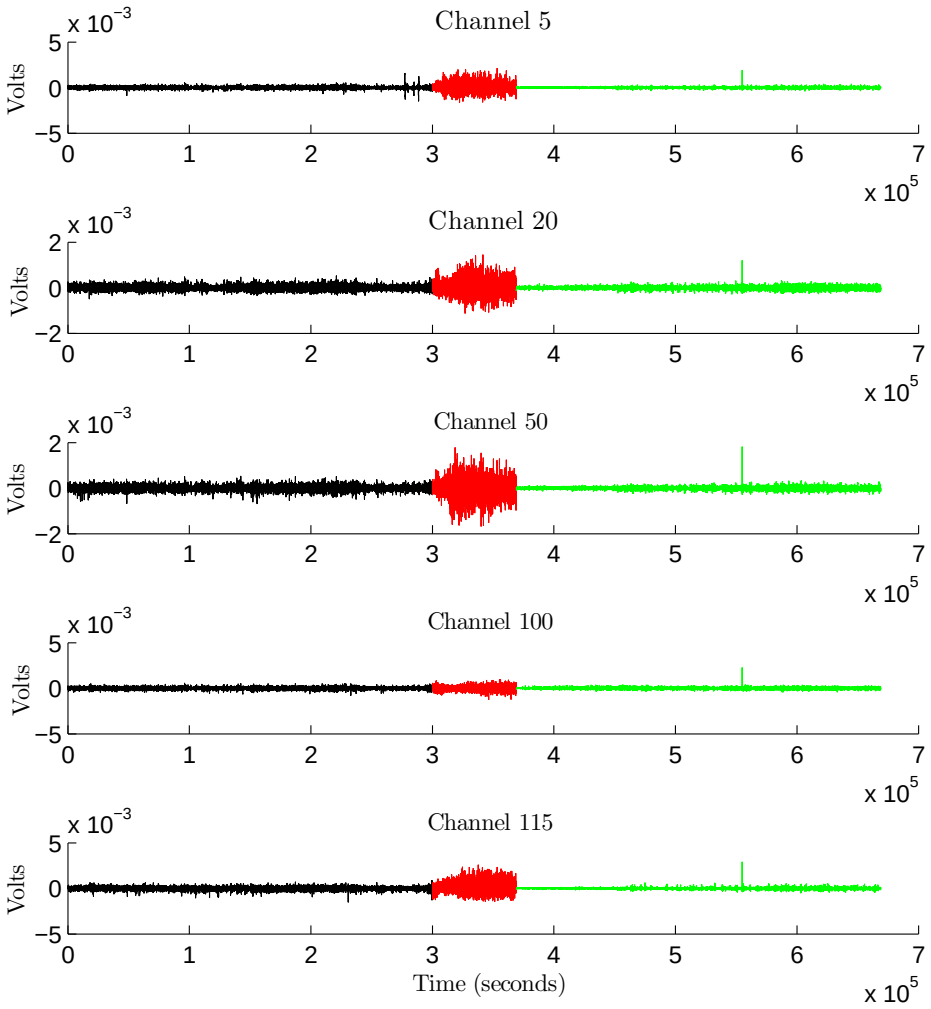

Figure 4.1: Plots of recordings from five different channels, Black: pre-seizure, red: seizure, green: post-seizure.

Figure 4.1 shows five channels of EEG recordings. The plots are colour coded to show the different stages of neural activities. Black, red and green lines show pre-seizure, seizure and post-seizure stages respectively.

Model			
Symbol	Parameter	Value	Unit
$[\Delta_x, \Delta_y]$	spatial discretisation step	[1,0.5]	mm
F_s	sampling frequency	1K	Hz
τ_1, τ_2	synaptic time constant	$[166^{-1}, 56^{-1}]$	sec^{-1}
ς	activation function slope	0.56	mV^{-1} spike sec^{-1}
f_{max}	maximum firing frequency	1	Hz
n_s	number of sensors	8×15=120	Not Applicable
$[\Delta_{sx}\Delta_{sy}]$	distance between adjacent sensors	[1,0.5]	mm
σ_m	observation Kernel width	0.9	mm
Σ_ε	observation noise variance	$0.1I_{n_y}$	mm^2
σ_y	disturbance spatial covariance width	1.3	mm
σ_d^2	disturbance variance	0.1	mV^2
n_b	number of basis functions	9×9=81	Not applicable
Δ_ϕ	distance between field basis functions	1.5	mm
σ_ϕ	width of field basis functions	1.58	mm^2
Estimation			
α	range of variation for sigma points	0.001	Not Applicable
β	prior knowledge of sigma points	2	Not Applicable
κ	scaling parameter	$3 - n_x$	Not Applicable
λ	scaling parameter	80.99	Not Applicable

Table 4.2: List of parameters of model and Unscented Kalman Smoother in estimation of connectivity kernel gains.

4.3 Model & Estimation

The estimation framework developed in Chapter 3 will be used in this section to estimate the connectivity kernel weights. It is assumed that the synaptic time constants are known and hence, some minor alterations have been applied to least squares estimator for the parameter estimation. A summary of model equations and estimation procedure will be also provided. Derivation of the model, its state-space representation and a detailed description of the estimation framework can be found in Chapter 3.

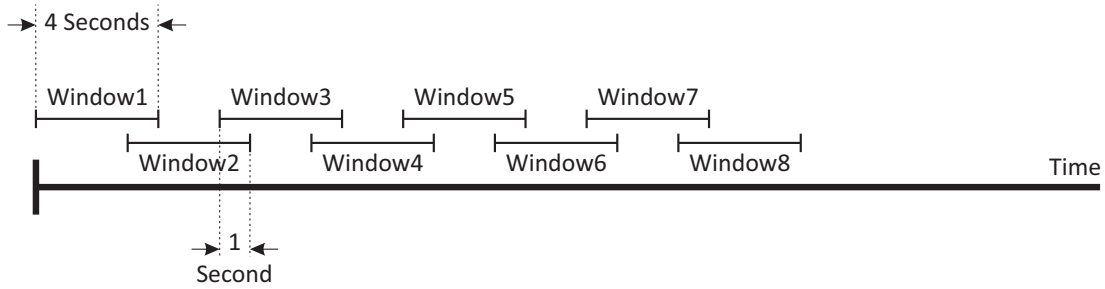

Figure 4.2: Windowing of the data prior to applying the estimation algorithm.

Figure 4.2 displays the windowing of the data. Data is split into smaller windows with fixed durations. Estimation is applied on observations at each window. Except the first window, the start and the end indices of each window can be found using (indexing)

$$Window = n * (WindowLength) - (n-1) * (OverlapWindowLength) \quad (4.1)$$

where $n > 0$ is the window number. Estimated kernel gains for each window are then plotted for each case.

Model equations

$$x_1^{t+1} = x_1^t + T_s x_2^t$$

$$x_2^{t+1} = -\xi_1 x_1^t + \xi_2 x_2^t + \xi_1 \Gamma^{-1} \int_{\Omega} \phi(r) \int_{\Omega} \psi^\top(r - r') f(\phi^\top(r') x_1^t) \partial r'' \partial r' \theta + \int_{\Omega} \phi(r) e^t(r) \partial r'$$

$\xi_1 = T_s \zeta_1 \zeta_2$	$\xi_2 = 1 - (\zeta_1 + \zeta_2) T_s$

Parameter Estimation

$$q(x_1^t) = \int_{\Omega} \Psi(r') f(\phi^\top(r') x_1^t) \partial r''$$

$$\Psi = [\psi_1, \psi_2, \psi_3]$$

$$W = \left[\Theta_1, \Theta_2, \Theta_3\right]'$$

$$e = \left[e_0, e_1 ...., e_{T-1}\right]'$$

$$Z = \breve{X} W + e$$

$$\breve{X} = \begin{bmatrix} q_1(\hat{x}_1^{0,f}) & q_2(\hat{x}_1^{0,f}) & q_3(\hat{x}_1^{0,f}) \\ q_1(\hat{x}_1^{1,f}) & q_2(\hat{x}_1^{1,f}) & q_3(\hat{x}_1^{1,f}) \\ \cdot & \cdot & \cdot \\ \cdot & \cdot & \cdot \\ \cdot & \cdot & \cdot \\ q_1(\hat{x}_1^{T-1,f}) & q_2(\hat{x}_1^{T-1,f}) & q_3(\hat{x}_1^{T-1,f}) \end{bmatrix}$$

$$Z = \left[\hat{x}_2^{1,f}, \hat{x}_2^{2,f} ...., \hat{x}_2^{T,f}\right]'$$

$$\hat{\varpi} = (\breve{X}^\top \breve{X})^{-1} \breve{X}^\top Z$$

State Estimation

$$Q(X^t) = \begin{bmatrix} 1 & T_s \\ -\xi_1 & \xi_2 \end{bmatrix} \begin{bmatrix} x_1^t \\ x_2^t \end{bmatrix} + \begin{bmatrix} 0 \\ \int_{\Omega} \xi_1 \Psi(r') f(\phi^\top x_1^t) \partial r' \theta \end{bmatrix}$$

$$\chi_{i,t+1}^{f-} = Q(\chi_{i,t}^f)$$

$$\hat{x}_{t+1}^{f-} = \sum_{i=0}^{2n_x} W_i^m \chi_{i,t+1}^{f-}$$

$$P_{t+1}^{f-} = \sum_{i=0}^{2n_x} W_i^{(c)} (\chi_{i,t+1}^{f-} - \hat{x}_{t+1}^{f-})(\chi_{i,t+1}^{f-} - \hat{x}_{t+1}^{f-})^\top + \Sigma_e$$

First: Forward Iterations	then: Backward Iterations
$K_{t+1} = P_{t+1}^{f-} C^\top (C P_{t+1}^{f-} C^\top + \Sigma_\epsilon)^{-1}$	$P_T^b = P_T^f, \hat{x}_T^b = \hat{x}_T^f$
$\hat{x}_{t+1}^f = \hat{x_{t+1}^{f-}} + K_{t+1}(y_{t+1} - C\hat{x}_{t+1}^{f-})$	$S_t = M_{t+1}^f [P_{t+1}^{f-}]^{-1}$
$P_{t+1}^f = (I - K_{t+1} C) P_{t+1}^{f-}$	$\hat{x}_t^b = \hat{x}_t^f + S_t [\hat{x_{t+1}^b} - \hat{x}_{t+1}^{f-}]$
$M_{t+1}^f = \sum_{i=0}^{2n_x} W_i^c (\chi_{i,t}^f - \hat{x_t^f})(\chi_{i,t+1}^{f-} - \hat{x}_{t+1}^{f-})^\top$	$P_t^b = P_t^f + S_t [P_{t+1}^b - P_{t+1}^{f-}] S_t^\top$

4.4 Results and Discussion

It should be noted that Figures 4.5 to 4.11 are generated based on a window length of 4000 data points (equal to 4 seconds) with an overlap of 1000 data points (equal to 1 second) which has resulted in 220 windows. Values for model parameters and estimation constants are given in Table 4.2.

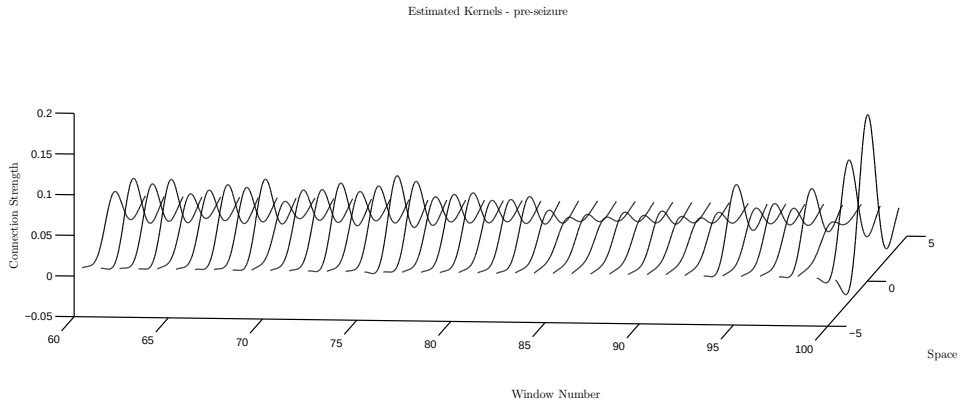

Figure 4.3: Estimated connectivity kernels during pre-seizure period.

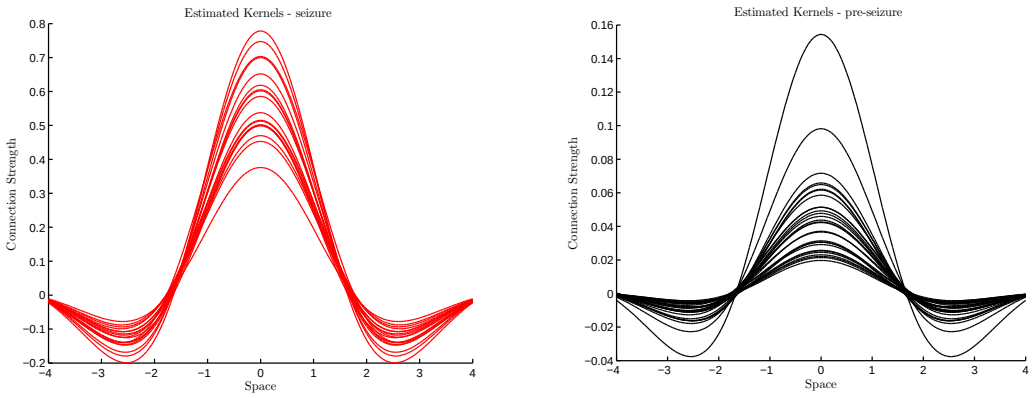

(a) Seizure period.

(b) Pre-seizure period.

Figure 4.4: (a) Reconstructed kernel in red during seizure for 28 windows. (b) Reconstructed connectivity kernel during pre-seizure for 28 windows before the seizure (shown by black lines).

It can be seen in Figure 4.4 that during the seizure period, there is a noticeable increase on the connectivity kernel gains. The results in Figure 4.4a show that

the inhibition and excitation has increased in amplitude during the seizure state. Changes in the connectivity kernel magnitudes starts towards the end of pre-seizure as displayed in Figure 4.3.

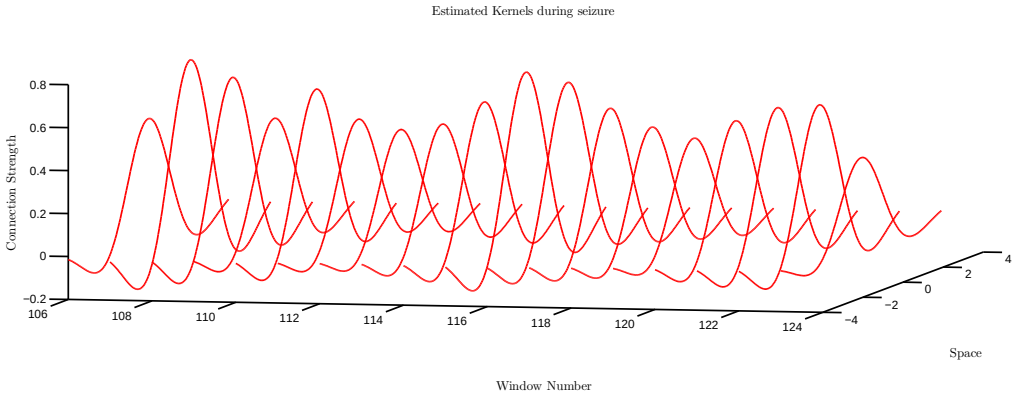

Figure 4.5: Estimated connectivity kernels during seizure period.

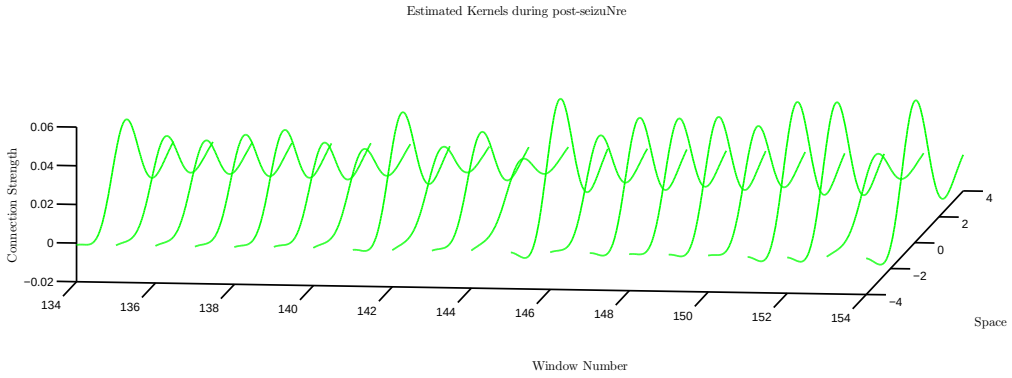

Figure 4.6: Estimated connectivity kernels during the post-seizure period.

Figures 4.5 and 4.6 show the estimated kernels over given number of the windows in the graphs during seizure and post-seizure stages, respectively.

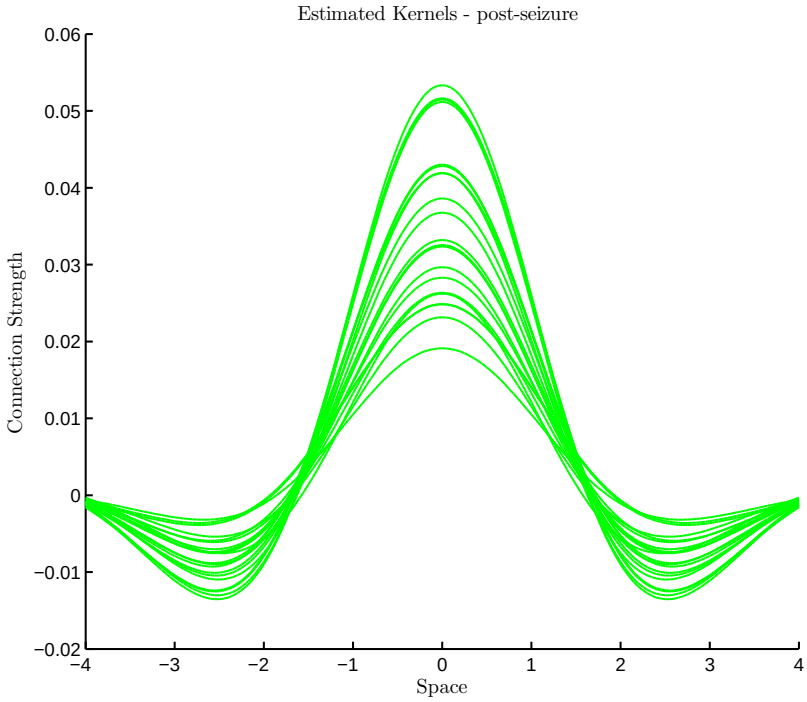

Figure 4.7: Estimated kernels during post-seizure period.

The estimated connectivity kernel follows a Mexican-hat connectivity structure with different excitatory and inhibitory amplitudes.

4.4.1 Transition States

Here the changes in connectivity kernel gains while the patient is going through an epileptic seizure are investigated. As the previous sections, a consistency in colours is held in this section has well (green for post-seizure, red for seizure and black for pre-seizure).

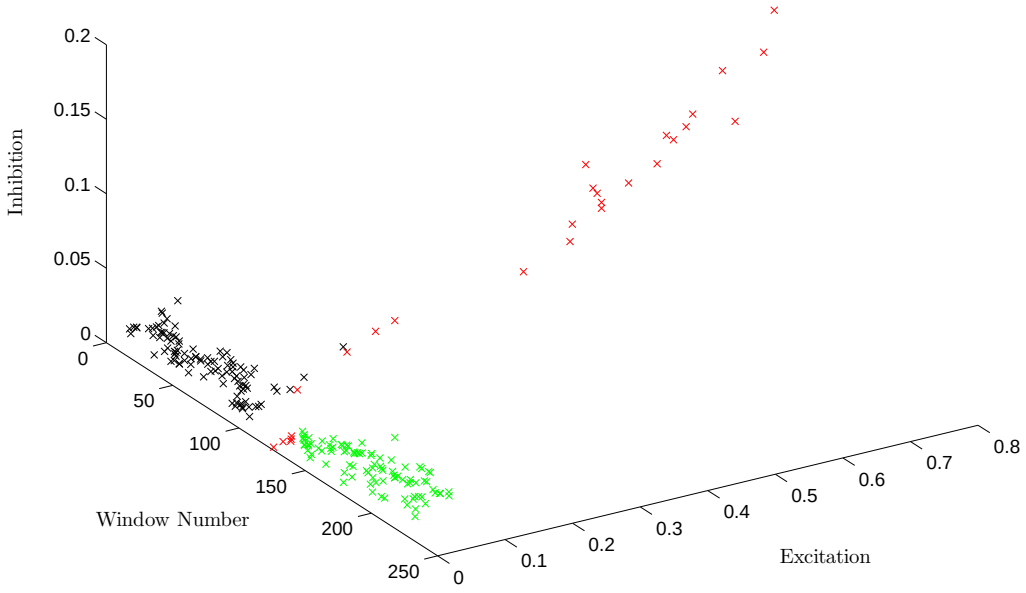

Figure 4.8: Change of excitation and inhibition in the connectivity kernel during different stages of the neural activity.

Changes in amplitude of excitation in the connectivity kernel versus amplitude of inhibition in the connectivity kernel during the full length of recorded seizure is given in Figure 4.8. The results suggest a patient specific trajectory for variations of connectivity kernel gains. This required further investigation and it is denoted as future work as discussed in the next chapter.

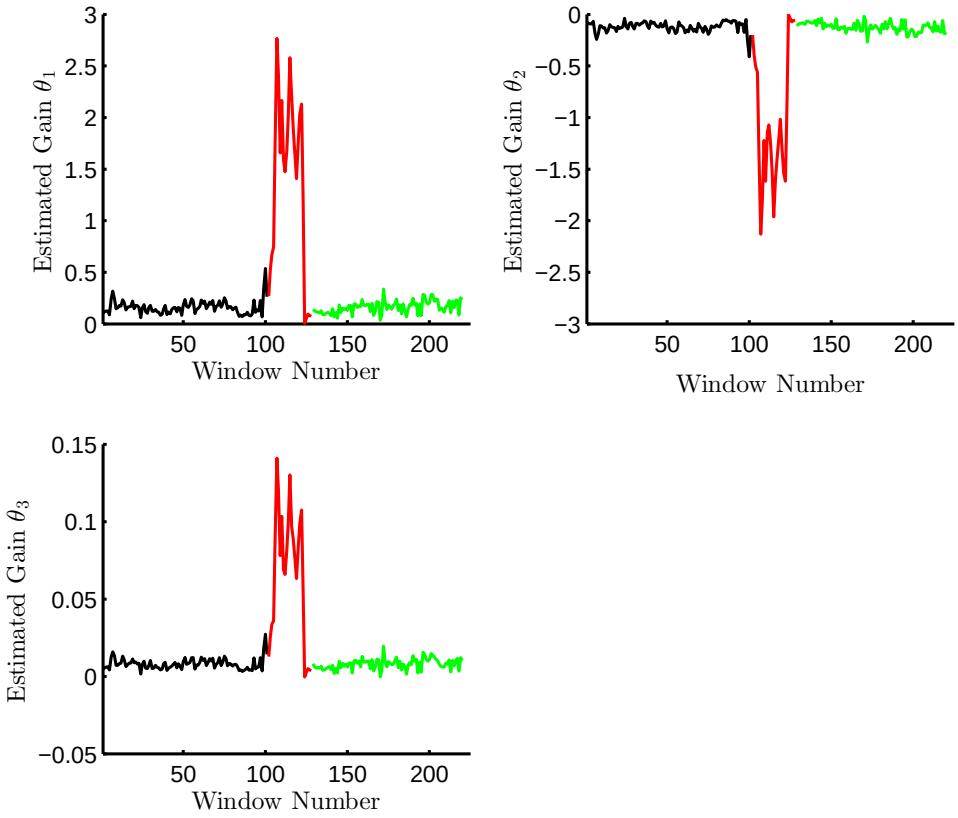

Figure 4.9: Change of connectivity kernel gains during pre-seizure, seizure and post-seizure periods (window size: 4000 data points, window overlapping: 1000 data points).

Figure 4.9 shows connectivity kernel gains estimated over each window of the data set. It is clear that the changes in the kernel gains can be easily detected where a threshold can be set to detect the changes in the neural activity.

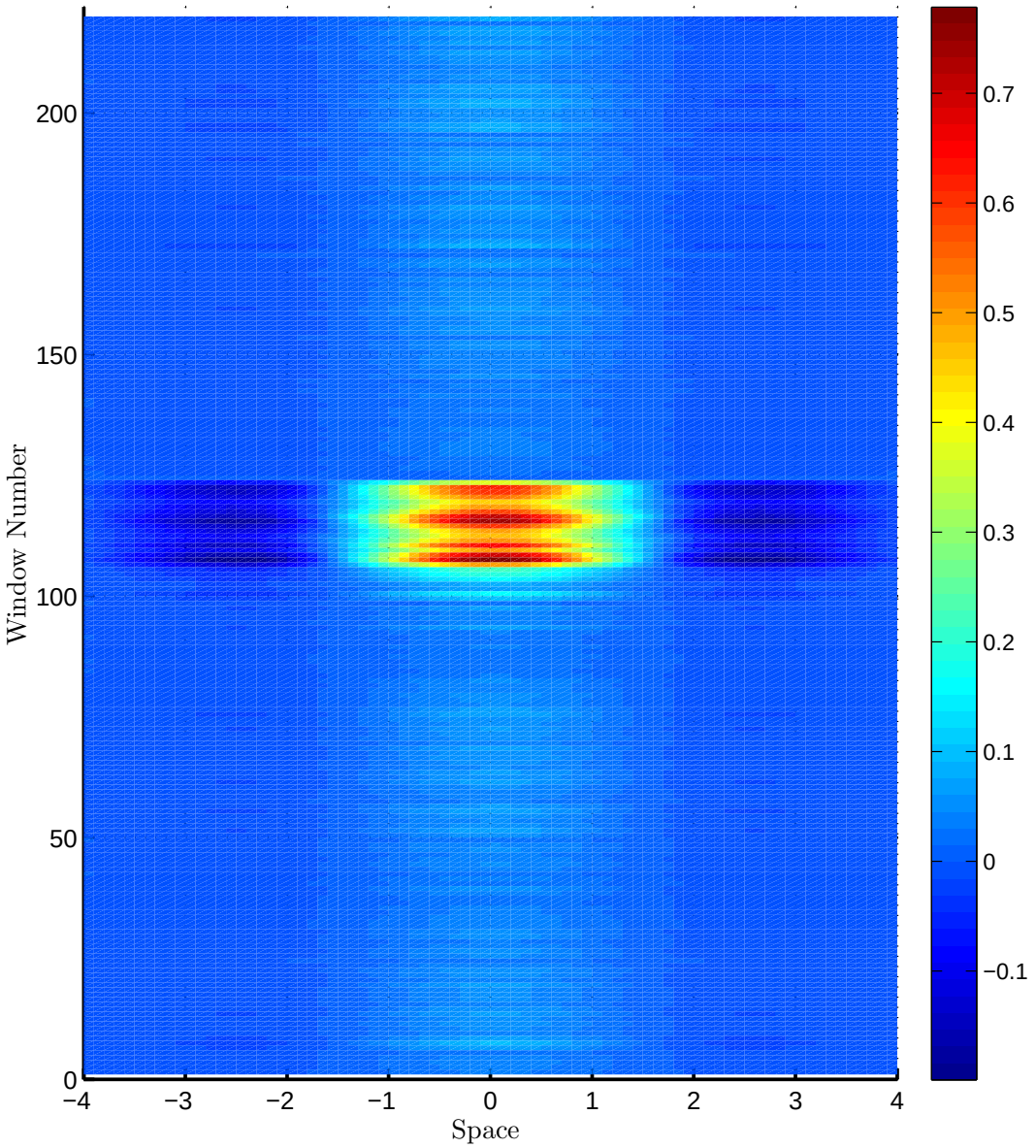

Figure 4.10: Estimated kernels during pre-seizure, seizure and post-seizure periods.

Similar to the previous results, it can be observed that the connectivity kernel gains increase during the seizure stage. Increase in inhibition is also better visualised in Figure 4.10.

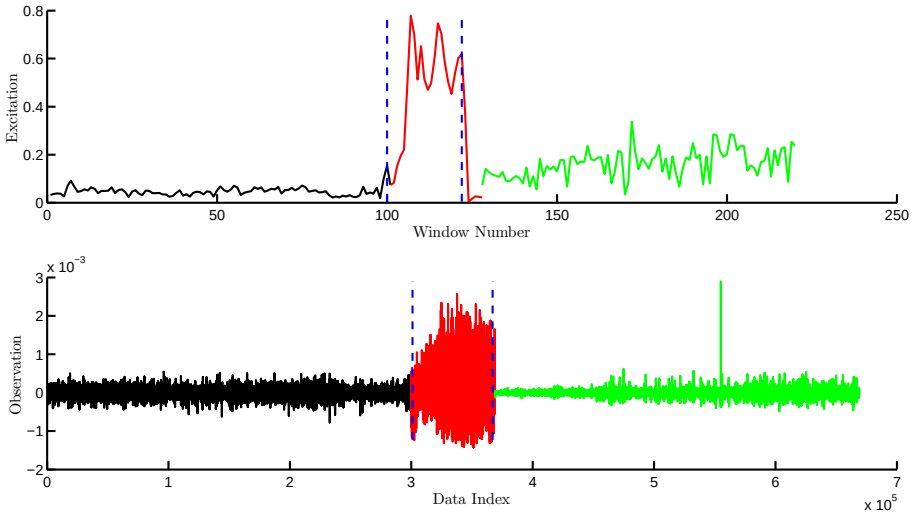

Figure 4.11: Estimated changes during the epileptic seizure versus recorded transition in the measurements.

An integration of a connectivity kernel gain (θ_3) over full length of epilepsy data and detecting the sharp change in the connectivity kernel gains have been applied and demonstrated in Figure 4.11. The blue dashed lines are edges where a sharp changes in connectivity kernel gains occur. The corresponding points in the recorded data also show changes in the state of the data.

4.5 Different Window Sizes

Two different windowing lengths are used in addition to the given settings in the previous section (Window length: 1.5, 2.5 and 4 seconds). Following figures demonstrate the results obtained with different windowing lengths. It can be concluded that the change in the window size does not affect the observed pattern in the results significantly.

4.5.1 Case 1: Window Size of 1500 Samples

Model and estimation parameters are the same as previous section as shown in Table 4.2. In this case, the window length is set to 1.5 seconds with an overlap

of 0.75 seconds. The alterations are checked to learn about the effect of different window length in the result.

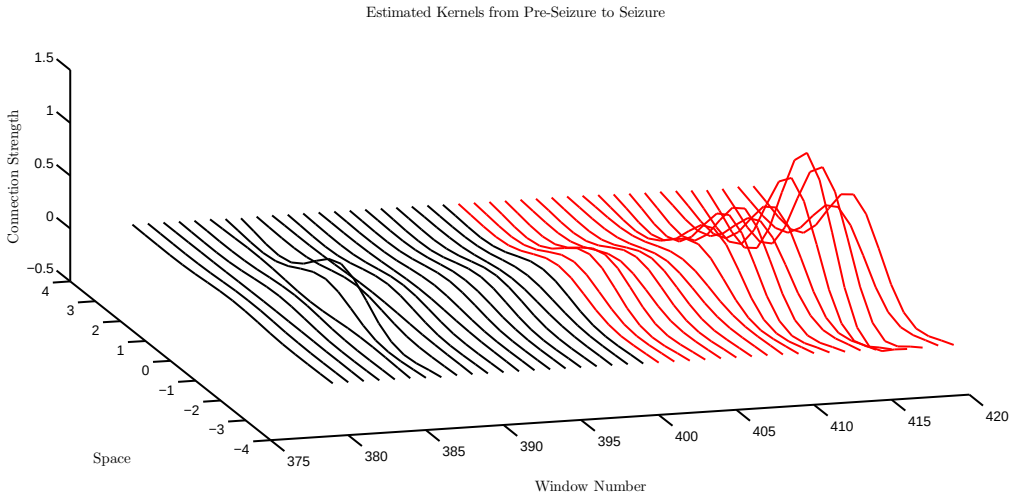

Figure 4.12: Estimated kernels at the transition from pre-seizure to seizure state (window length: 1500 ms, overlap length: 750 ms).

Estimated kernel gains of epilepsy data during the transition from pre-seizure stage to seizure stage is given in Figure 4.12. Estimated kernels plotted in red colour correspond to the pre-seizure stage and estimated kernels plotted in blue are related to the seizure stage. A sudden change in connectivity kernel gains - especially with excitatory gains - are evident from the figures.

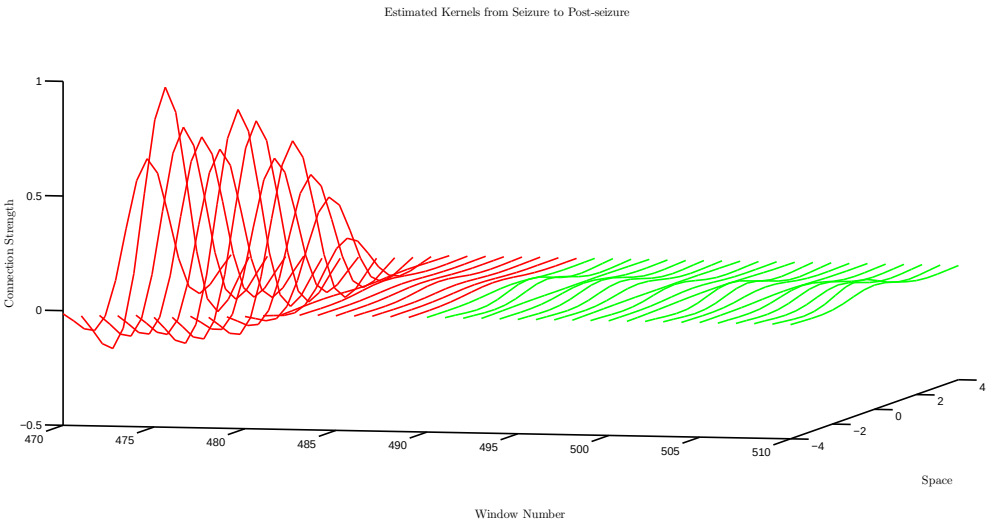

Figure 4.13: Estimated kernels in transition from seizure to post-seizure state (window length: 1500 ms, overlap length: 750 ms).

The kernels plotted in red are obtained from seizure duration and kernels in green are reconstructed based on kernel gain estimations during the post-seizure period.

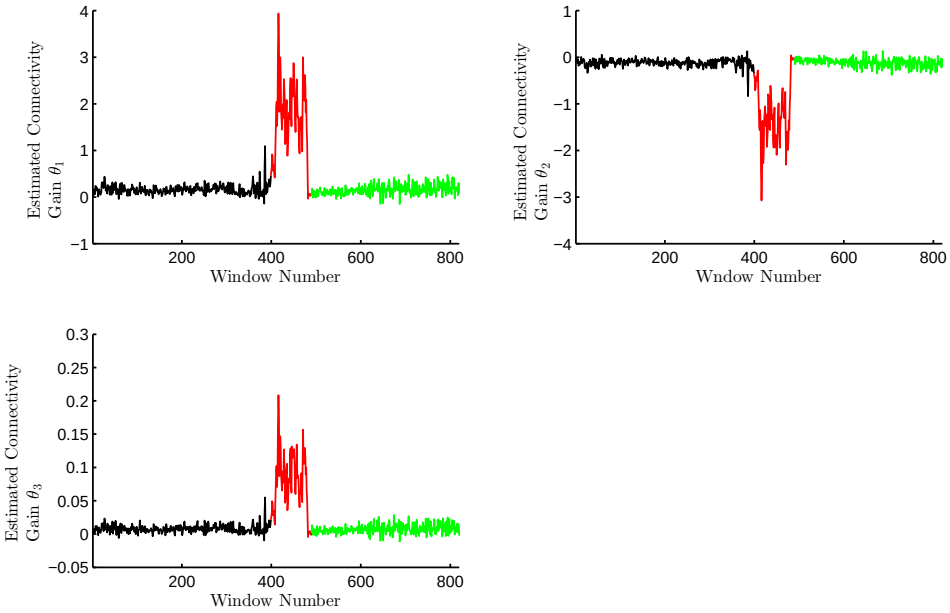

Figure 4.14: Change of connectivity kernel gains during different seizure stages (window length:1500 ms, overlap length: 750 ms).

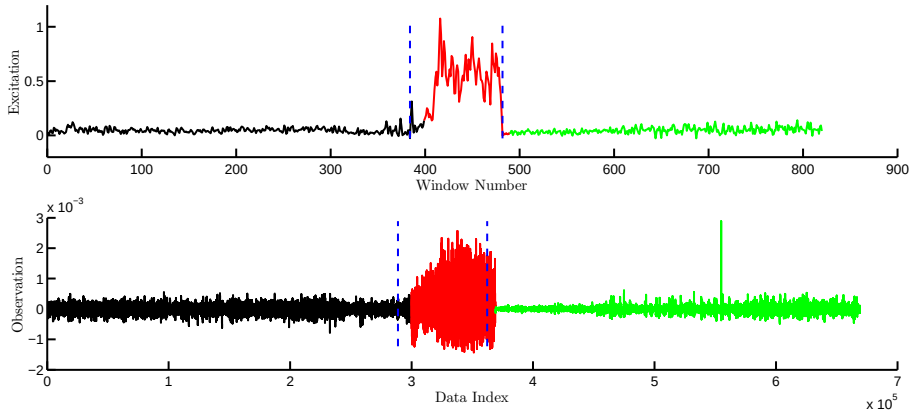

Figure 4.15: Estimated changes during the epileptic seizure versus recorded transition in the measurements (window length: 1500 ms, overlap length: 750 ms).

4.5.2 Case 2: Window Size of 2500 Samples

Following figures demonstrate the changes in the connectivity kernel gains and reconstructed kernel. A window length of 2500 data points with an overlap of 500 data points are considered in this case. It should be mentioned that the statements about the variations of gains also hold true in this case.

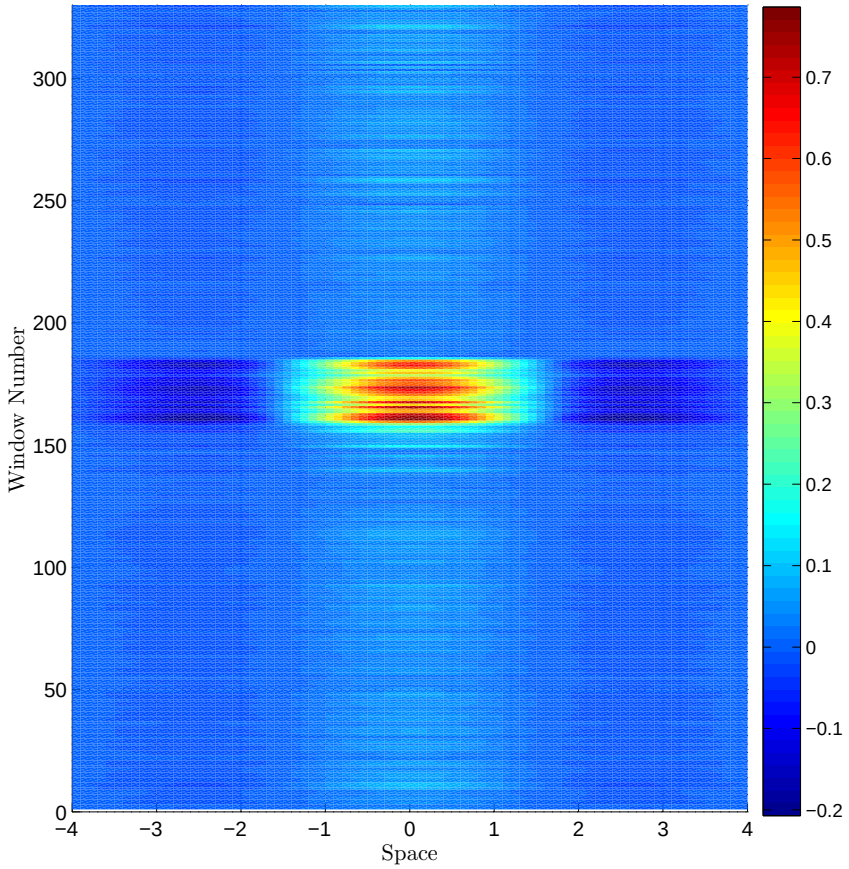

Figure 4.16: Estimated kernel during pre-seizure, seizure and post-seizure periods (window length: 2500 ms, overlap length: 500 ms).

Figure 4.16 shows the increase in inhibitory activity and excitatory activity during the seizure.

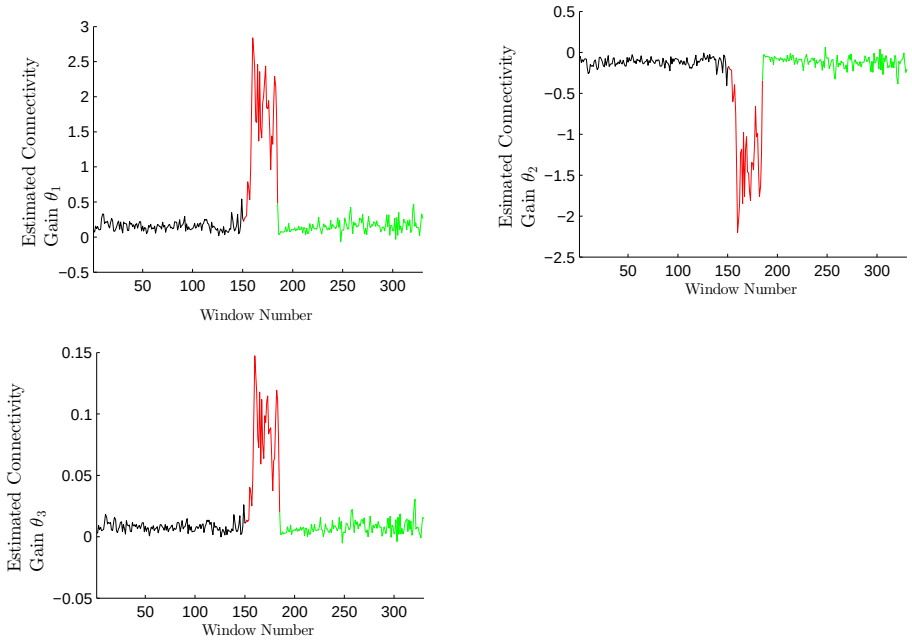

Figure 4.17: Change of connectivity kernel gains during different seizure stages (window length: 2500 ms, overlap length: 500 ms).

Three different window sizes have been applied and corresponding results are consistent with an increase of excitation and inhibition in the reconstructed kernels during seizure period. Hence, it can be concluded that in this particular case seizure state will result in increase of the excitatory and inhibitory activities as exhibited in reconstructed connectivity kernel. As it will be discussed in the future work in the next chapter, the algorithm requires further testing using data from more patients with epilepsy. The proposed method can be potentially used to infer patient specific connectivity kernel parameters from electro-physiological data.

Chapter 5

Heterogeneous Amari Type Neural Field Model

5.1 Introduction

During the past decades significant area of the brain research is devoted to understanding the underlying dynamics of the brain's function. A general discussion of heterogeneous connectivity in large neural networks can be found in Stefanescu & Jirsa [2008]. Although each model is designed to describe the dynamics of the brain certain assumptions are made in each model to overcome the overwhelming complexity of the problem. A basic assumption in many of the neural field models is the symmetrical connection in a small local neural population [Chavez *et al.*, 2011]. In other words, the connectivity matrix between the neural nodes has a spatial translation symmetry. However, in patchy areas of the brain long-range connections have been observed that effect the spatial translation of the connectivity matrix. Visual cortex can be named as a region where heterogeneous connectivity is commonly reported [Brackley & Turner, 2009; Bressloff, 2003]. Spatio-temporal patterns can be formed in a sheet of neurons. Unlike usual physical or chemical pattern formations, the patterns formed by neural activities originate from both short and long-range connections. Such patterns contribute to neural activities in a macroscopic level in addition to local synchronised rhythms [Jirsa & Kelso, 2000]. Cortical structure consists of short

range intracortical connectivity which are local homogeneous connections and also long-range corticocortical connection which can be presented by non-local heterogeneous connections. In such a configuration, the heterogeneous connectivity is considered as long-range connections. Previous work of Jirsa *et al.* [2002]; Roth *et al.* [2014] show the examples of heterogeneous connections existence in areas with widely distributed networks such as parieto-frontal cortex which is also correlated with sensorimotor actions. It is demonstrated that mean field models with heterogeneous connections produce complex spatial patterns.

The model of the heterogeneous connectivity kernel and its contribution to global neural dynamics are extended version of work in Jirsa *et al.* [2002] where a two point heterogeneous connectivity is considered in one dimensional space. This is extended to two dimensions in this work.

By assuming the long-range connections as heterogeneous connectivity, the developed model is a closer biological description of the neural dynamics and promotes an efficient information transmission in the neural system. Heterogeneous connectivity is considered in relation to formation of self-organised fluctuations and that global response properties are effected by this structure [Chavez *et al.*, 2011; Jirsa *et al.*, 2002]. Such models are used in describing a number of activities related to cortex and phenomena affecting the neural field such as evoke potentials, epileptic behaviour and visual hallucinations [Coombes, 2005; Hendrey *et al.*, 1999].

Introducing a heterogeneous connectivity in model equations adds additional complexity to the model and hence increases the computational complexity of the estimation algorithm. In the following sections, a number of assumptions will be introduced in order to simplify the problem. Clearly, a simplified model of a small network can act as a single node on a large network where it presents the dynamics of its underlying network.

The simulated field for a single time frame is displayed in the left panel of Figure 5.1. In the right panel, the centre of the long-range connection points are given. Two peaks on the simulated field emerge on the centres of the corresponding long-range connection points.

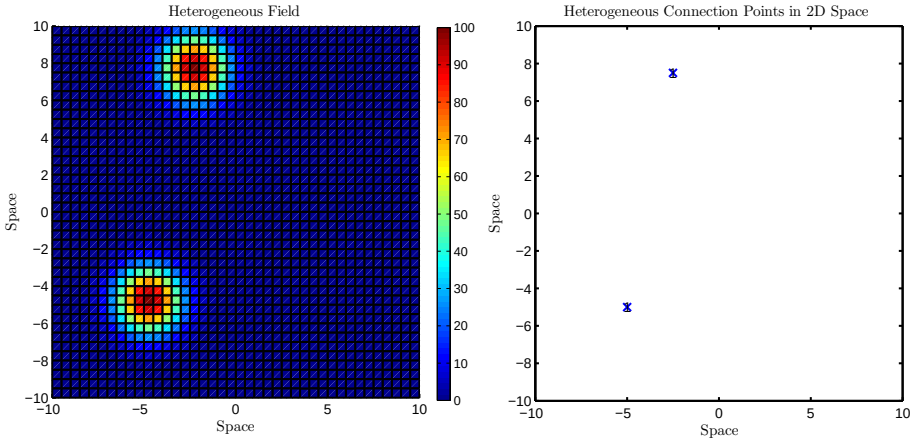

Figure 5.1: Heterogeneous connection points.

As mentioned earlier, heterogeneous connectivity structure increases the computational complexity where additional parameters need to be estimated. In order to simplify the problem, it is assumed that the long-range connections in this work are two-way and symmetric in connectivity gains. From this point on, the term "Heterogeneous connectivity" is referred to the long-range connections that cause the connectivity kernel to be spatially variant. Number of heterogeneous connection points are limited to a single pair on a two dimensional space. Additionally, a symmetric heterogeneous connection is assumed.

Next section is focused on deriving the model equations for simulations and decomposing the model and in order to obtain a state-space representation which facilitates the estimation process.

5.2 Model Derivation with Heterogeneous Spatial Connectivity Kernel

The model presented in this section is based on relation of average action potentials. Assuming that function $g(r,t)$ presents the average number of action potentials arriving at time t and location r, the postsynaptic potential $v(r,t)$ generated at location r by all other arriving surrounding populations can be

written in the form of

$$v(r,t) = \int_{-\infty}^{t} h(t-t')g(r,t')\partial t' \tag{5.1}$$

$$g(r,t) = \int_{\Omega} W(r,r')f(v(r',t))\partial r' \tag{5.2}$$

where $h(t)$ is the postsynaptic response kernel, given by

$$h(t) = u(t)e^{-\zeta t} \tag{5.3}$$

In equation (5.3), parameter ζ is the inverse of synaptic time constant τ and $u(t)$ is the Heaviside step function.

The connectivity kernel is $W(r,r')$ and $f(v(r',t))$ denotes the firing rate which is a sigmoid function given by equation (5.4) [Aram, 2011; Jirsa & Haken, 1997].

$$f(v(r',t)) = \frac{1}{1+e^{\varsigma(\vartheta_0 - v(r',t))}} \tag{5.4}$$

In equation (5.4), v_0 is the firing rate threshold which should be satisfied before a new postsynaptic potential is fired. Parameter ς is the slope of the linear section of the sigmoid function. The connectivity kernel is a Mexican hat function or a Wizard hat which can be decomposed into a sum of Gaussian basis functions with different gains and widths (same centres).

Substituting equation (5.2) into (5.1), the spatio-temporal model can be obtained as

$$v(r,t) = \int_{-\infty}^{t} h(t-t') \int_{\Omega} W(r,r')f(v(r',t))\partial r'\partial t' \tag{5.5}$$

It can be shown that the synaptic kernel response is a Green's function. Assuming a first order differential operator as $D = \partial/\partial t + \zeta$, Green function satisfies the following relation

$$Dh(t) = \delta(t) \tag{5.6}$$

where $\delta(t)$ is a Dirac delta function [Bayin, 2006]. Considering this, multiplying both sides of the equation (5.1) by the differential operator D, the following can be obtained

$$Dv(r,t) = D(h * g)(r,t) \tag{5.7}$$

$$Dv(r,t) = Dh * g(r,t) \tag{5.8}$$

$$Dv(r,t) = \delta(t) * g(r,t) = g(r,t) \tag{5.9}$$

The sign * denotes the convolution operator. This will result in the standard mean field model given by

$$\frac{\partial v}{\partial t} + \xi v(r,t) = \int_{\Omega} W(r',r) f(v(r',t)) \partial r' \tag{5.10}$$

First order Eurler's method is applied on standard mean field model given by equation (5.10) to obtain the integro-difference equation (IDE) form of the model.

$$\frac{v(r,t+T_s) - v(r,t)}{T_S} = -\zeta v(r,t) + \int_{\Omega} W(r,r') f(v(r',t)) \partial r' \tag{5.11}$$

Where $\xi = 1 - T_s\zeta$ and T_s is the sampling time. It is assumed that after this point, the index t is used for denoting the current time and $t+1$ is used to indicate the next time frame. After simplifying equation (5.11), the following discrete form of the model can be obtained

$$v_{t+1}(r) = \xi v_t(r) + T_s \int_{\Omega} W(r,r') f(v(r',t)) \partial r' \tag{5.12}$$

It should be noted that the use of first order Euler's method can affect the system's behaviour and also cause a noticeable difference between the continuous and discrete time systems. In the simulations of the neural field, the sampling period is chosen to be ten times bigger than the synaptic time constant to minimise this effect. This yields a stable system and a good estimation performance.

In this chapter the connectivity kernel is assumed to be the sum of heterogeneous connectivity kernel and the homogeneous connectivity kernel which is given by Jirsa *et al.* [2008].

$$W(r, r') = \Psi_{hom}(r, r') + \Psi_{het}(r, r') \tag{5.13}$$

Replacing equation (5.13) into (5.12), the following equation will be obtained

$$v_{t+1}(r) = \xi v_t(r) + T_s \int_{\Omega} \left(\Psi_{hom}(r, r') + \Psi_{het}(r, r')\right) f(v(r', t)) \partial r' \tag{5.14}$$

This equation can be expanded to give

$$v_{t+1}(r) = \xi v_t(r) + T_s \int_{\Omega} \Psi_{hom}(r, r') f(v(r', t)) \partial r' + T_s \int_{\Omega} \Psi_{het}(r, r') f(v(r', t)) \partial r' \tag{5.15}$$

Considering the isotropy of the homogeneous connectivity kernel, it can be assumed that

$$\Psi_{hom}(r, r') = \Psi_{hom}(r - r') \tag{5.16}$$

Finally, the discretized form of IDE model with homogeneous and heterogeneous connectivity can be written as

$$v_{t+1}(r) = \xi v_t(r) + T_s \int_{\Omega} \Psi_{hom}(r - r') f(v(r', t)) \partial r' + T_s \int_{\Omega} \Psi_{het}(r, r') f(v(r', t)) \partial r' + e_t(r) \tag{5.17}$$

where $e_t(r)$ includes the effect of model uncertainty and unmodeled inputs. It is a zero mean Gaussian process with spatial covariance function of $\gamma(r - r')$ [Petersen & Middleton, 1962; Rasmussen & Williams, 2005].

The observation equation which models the data recorded from intracranial sensors is given by

$$y_t(r_n) = \int_{\Omega} m(r - r') v_t(r') \partial r' + \varepsilon_t(r_n) \tag{5.18}$$

where $m(r - r')$ is the observation kernel, r_n is the location of electrodes on

the cortex and n is the sensor number. $\varepsilon_t(r_n)$ denotes a multivariate normal distribution with zero mean and the covariance matrix $\Sigma_\varepsilon = \sigma_\varepsilon^2 I$ where I is the identity matrix.

5.2.1 Decomposition of the Model

Neural field can be decomposed by use of Gaussian basis functions to allow application of standard estimation framework such as Unscented Kalman Filter. Decomposition will result in finite dimensional vector states.

$$v_t(r) \approx \phi(r)^\top x_t \tag{5.19}$$

$$\Psi_{hom}(r, r') = \psi_{hom}(r, r')^\top \theta_{hom} \tag{5.20}$$

$$\Psi_{het}(r, r') = \psi_{het}(r, r')^\top \theta_{het} \tag{5.21}$$

Following the previous work Jirsa [2009]; Qubbaj & Jirsa [2007], in case of two point heterogeneous connection, the following equation can be used to describe long-range connections as the heterogeneous connectivity.

$$\psi_{het}(r, r') = \begin{bmatrix} \delta(r - r_1)\delta(r' - r_2) & \delta(r - r_2)\delta(r' - r_1) \end{bmatrix} \tag{5.22}$$

x_t in equation (5.19) is a vector of states (time dependant) and ϕ is spatial field basis functions which is defined as

$$\phi(r - r') = e^{\frac{-(r-r')^\top (r-r')}{\sigma_\phi^2}} \tag{5.23}$$

As mentioned earlier, the connectivity kernel can also be described as sum of Gaussian basis functions as demonstrated in Figure 5.2. In this case three Gaussian basis functions are used for the decomposition.

It should be noted that the parametric form of the connectivity kernel is assumed to be known whereas the connectivity kernel gain θ is to be estimated. A quick reminder that in case of heterogeneous connectivity kernel, a two dimensional connectivity matrix is considered where two long-range connections are considered. The heterogeneous connections are assumed to be symmetric.

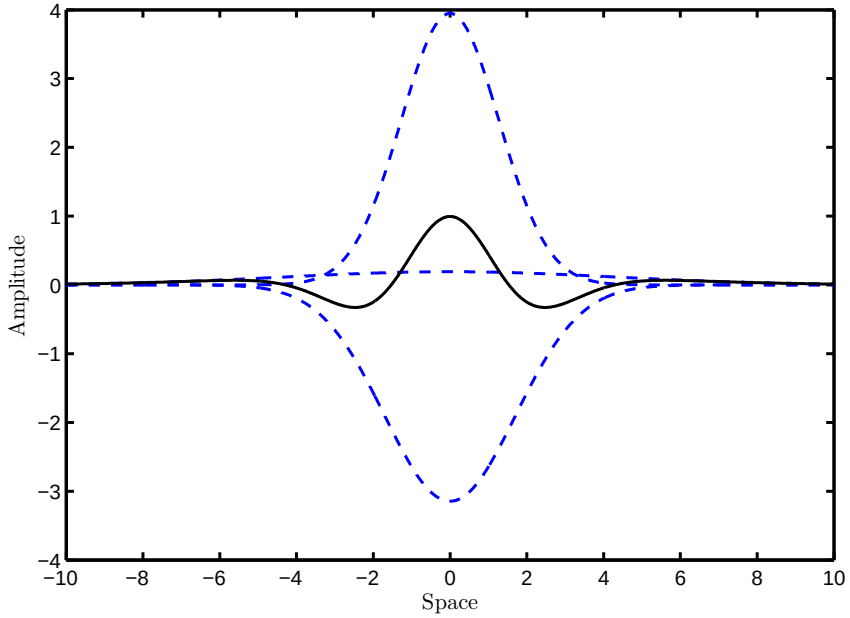

Figure 5.2: Homogeneous connectivity kernel as sum of three Gaussian basis functions.

Additionally, connections have been assumed to be active over simulation period where its spatial coordinates are fixed.

5.2.2 State-Space Representation

In this section the state-space representation of the model is derived. Multiplying both sides of equation (5.12) by $\phi(r)$ and integrating over the space will result in

$$\int_{\Omega} \phi(r) v_{t+1}(r) \partial r \tag{5.24}$$

$$\approx \xi \int_{\Omega} \phi(r) v_t(r) \partial r + \int_{\Omega} \phi(r) e_t(r) \partial r + T_s \int_{\Omega} \phi(r) \int_{\Omega} \Psi_{het}(r, r') f(v(r', t)) \partial r' \partial r$$

$$+ T_s \int_{\Omega} \phi(r) \int_{\Omega} \Psi_{hom}(r - r') f(v(r', t)) \partial r' \partial r$$

We define the following term which will simplify the derivation of the model in a later step

$$\Gamma \cong \int_{\Omega} \phi(r)\phi(r)^{\top}\partial r \tag{5.25}$$

The new term Γ is a matrix of size $n_x \times n_x$ and based on its definition, it is a positive definite matrix and hence is invertible. Replacing equation (5.19) in equation (5.24) and simplifying by use of equation (5.25), it can be obtained that

$$x_{t+1} = T_s\Gamma^{-1}\int_{\Omega}\phi(r)\int_{\Omega}\psi_{hom}(r-r')^{\top}f(\phi(r')^{\top}x_t)\partial r'\partial r\theta_{hom} \tag{5.26}$$

$$+ T_s\Gamma^{-1}\int_{\Omega}\phi(r)\int_{\Omega}\psi_{het}(r,r')^{\top}f(\phi(r')^{\top}x_t)\partial r'\partial r\theta_{het} + \xi x_t$$
$$+ \Gamma^{-1}\int_{\Omega}\phi(r)e_t(r)\partial r$$

Following the above equations, disturbance vector for states becomes

$$e_t = \Gamma^{-1}\int_{\Omega}\phi(r)e_t(r)\partial r \tag{5.27}$$

Hence, disturbance vector is a linear function of $e_t(r)$. Expected value of $e_t(r)$ is equal to

$$E[e_t] = \Gamma^{-1}\int_{\Omega}\phi(r)E[e_t(r)]\partial r = 0 \tag{5.28}$$

The disturbance covariance matrix can be obtained by

$$\begin{aligned}\Sigma_e &= E[e_t e_t^{\top}]\\ &= \Gamma^{-1}e[\int_{\Omega}\phi(r)e_t(r)\partial r\int_{\Omega}\phi^{\top}(r')e_t(r')\partial r']\Gamma^{-\top}\\ &= \Gamma^{-1}\int_{\Omega}\int_{\Omega}\phi(r)E[e_t(r)e_t(r')]\phi^{\top}(r')\partial r'\partial r\Omega^{-\top}\end{aligned}$$

Therefore we have

$$\Sigma_e = \Gamma^{-1} \int_\Omega \int_\Omega \phi(r)\gamma(r-r')\phi^\top(r')\partial r'\partial r\Gamma^{-\top} \tag{5.29}$$

Hence, equation (5.26) can be written as

$$\begin{aligned} & x_{t+1} = \\ & T_s\Gamma^{-1} \int_\Omega \phi(r) \int_\Omega \psi_{hom}(r-r')^\top f(\phi(r')^\top x_t)\partial r'\partial r\theta_{hom} \\ & + T_s\Gamma^{-1} \int_\Omega \phi(r) \int_\Omega \psi_{het}(r,r')^\top f(\phi(r')^\top x_t)\partial r'\partial r\theta_{het} + \xi x_t \\ & + e_t \end{aligned} \tag{5.30}$$

where $e_t(r)$ is a zero mean normally distributed white noise process with its covariance given by equation (5.29).

A state-space presentation can be given in a compact form as

$$x_{t+1} = Q(x_t) + e_t \tag{5.31}$$

where

$$\begin{aligned} Q(x_t) = \xi x_t + T_s\Gamma^{-1} \int_\Omega \phi(r) \int_\Omega \psi_{hom}(r-r')^\top f(\phi(r')^\top x_t)\partial r'\partial r\theta_{hom} \\ + T_s\Gamma^{-1} \int_\Omega \phi(r) \int_\Omega \psi_{het}(r,r')^\top f(\phi(r')^\top x_t)\partial r'\partial r\theta_{het} \end{aligned}$$

The observation equation is described by

$$y_t = \int_{\Omega} m(r_n - r')\phi^{\top}(r')x_t \partial r' + \varepsilon_t(r) \tag{5.32}$$

The compact form of the observation equation is given by

$$y_t = Cx_t + e_t \tag{5.33}$$

where the elements of the observation matrix, C, are given by

$$C_{ij} = \int_{\Omega} m(r_i - r')\phi_j(r')\partial r' \tag{5.34}$$

5.3 Parameter and State Estimation

It is intended to estimate the connectivity kernel gains $\Theta = [\theta_1, \theta_2, \theta_3, \theta_{het}]$ for homogeneous and heterogeneous connection in addition to inverse of time constant $\xi = 1 - T_s\zeta$ and state vector, x.

It is assumed that the above parameters are fixed during a given set of data recorded over a short duration of time.

The estimation process is based on two iterative parts. The first part is to use the estimated states to update the parameter estimation. The updated set of parameters are then applied in the next iteration of the state estimation. This process continues till the estimated parameters are converged. The estimation is initialised by a bounded random state vector which ensures that the initial estimation of parameters will result in a stable kernel.

Following the earlier work of Aram [2011], additive Unscented Raunch-Tung-Striebel Smoother (URTSS) is used for the state estimation. In this method, Unscented Kalman Filter is applied in forward iterations to obtain filtered state estimates, $\hat{x}_t^f$, using a carefully selected minimal set of sigma points, followed by a backward pass to capture smoothed states estimates, x_t^b. This method can handle the nonlinearity and it is reported to show a better performance in dealing with nonlinearity in comparison to other methods such as EKF. This procedure is also

superior to other more computationally expensive methods such as Sequential Monte Carlo (SMC) filtering.

The sigma points are obtained by the following unscented transforms. Once calculated, sigma points go through the state equations. For calculation of the sigma points, χ, the following steps should be implemented.

$$\chi_0 = \bar{x} \tag{5.35}$$

$$\chi_i = \bar{x} + (\sqrt{(n_x + \lambda)P_x})_{i-n_x}, i = 1, ..., n_x \tag{5.36}$$

$$\chi_i = \bar{x} - (\sqrt{(n_x + \lambda)P_x})_{i-n_x}, i = n_x + 1, ..., 2n_x \tag{5.37}$$

$$\lambda = \alpha^2(n_x + \kappa) - n_x \tag{5.38}$$

$$\kappa = 3 - n_x \tag{5.39}$$

where $\bar{\mathrm{x}}$ is the estimated states in the forward/backward iteration. P_x is covariance matrix for filtering. $(\sqrt{(n_x + \lambda)P_x})_i$ is the i^{th} column of scaled covariance matrix. α is used to specify the variation range of sigma points from states. It can take an arbitrary set value which is set as a small positive constant to minimise the higher order effects. The value of α is set to 10^{-3} [Haykin, 2004].

Mean and covariance prediction is obtained by applying weighted state equations to sigma points. Weights are calculated by

$$W_0^{(m)} = \frac{\lambda}{n_x + \lambda} \tag{5.40}$$

$$W_0^{c} = \frac{\lambda}{n_x + \lambda} + (1 - \alpha^2 + \beta) \tag{5.41}$$

$$W_i^{(m)} = W_i^{(c)} = \frac{1}{2(n_x + \lambda)}, i = 1, ..., 2n_x \tag{5.42}$$

Where superscripts m and c stand for mean and covariance. Parameter β describes the prior knowledge of the distribution of the states (β is given a value of two with regards to a Gaussian disturbance) [Haykin, 2004]. Standard Kalman filter equations are used to update the states as the observation equation is linear.

Despite the fact that the system is nonlinear, the parameters of the system are linear with respect to states. Hence, a least squares method is used to update the parameter values in each iteration. The following sub-section will explain the

least squares method on updating the parameters [Stigler, 1981].

5.3.1 Least Squares Estimator

Considering that the heterogeneous connectivity is assumed to be symmetric, a single gain is considered during the estimation process ($\mu_{12} = \mu_{21}$). This is reflected in the state equation by θ_{het}.

$$Q(x_t) = \xi x_t + q(x_t)\theta_{hom} + \Upsilon(x_t)\theta_{het} \tag{5.43}$$

where

$$q(x_t) = \int_{\Omega} \Psi_{hom}(r - r')f(\phi^{\top}(r')x_t)\partial r'$$
$$\Upsilon(x_t) = T_s\Gamma^{-1}\begin{bmatrix} \phi(r_1)f(\phi(r_2)x^t) & \phi(r_2)f(\phi(r_1)x^t) \end{bmatrix}\theta_{het}$$
$$\theta_{het} = \begin{bmatrix} \mu_{12} \\ \mu_{21} \end{bmatrix}, \mu_{12} = \mu_{21}$$

For an estimated state sequence from the initialisation or an iteration of the URTSS, equations below are given

$$x_1^f = \xi\hat{x}_0^f + q(\hat{x}_0^f)\theta_{hom} + \Upsilon(\hat{x}_0^f)\theta_{het} + e_0$$
$$x_2^f = \xi\hat{x}_1^f + q(\hat{x}_1^f)\theta_{hom} + \Upsilon(\hat{x}_1^f)\theta_{het} + e_1$$
$$.$$
$$.$$
$$.$$
$$x_T^f = \xi\hat{x}_{T-1}^f + q(\hat{x}_{T-1}^f)\theta_{hom} + \Upsilon(\hat{x}_{T-1}^f)\theta_{het} + e_{T-1}$$

The above set of equations can be written in a compact form as

$$Z = \breve{X}W + e \tag{5.44}$$

Where

$$\breve{X} = \begin{bmatrix} q_1(\hat{x}^{0,f}) & q_2(\hat{x}^{0,f}) & q_3(\hat{x}^{0,f}) & \Upsilon(\hat{x}^{0,f}) & \hat{x}^{0,f} \\ q_1(\hat{x}^{1,f}) & q_2(\hat{x}^{1,f}) & q_3(\hat{x}^{1,f}) & \Upsilon(\hat{x}^{1,f}) & \hat{x}^{1,f} \\ . & . & . & . & \\ . & . & . & . & \\ . & . & . & . & \\ q_1(\hat{x}^{T-1,f}) & q_2(\hat{x}^{T-1,f}) & q_3(\hat{x}^{T-1,f}) & \Upsilon(\hat{x}^{T-1,f}) & \hat{x}^{T-1,f} \end{bmatrix} \tag{5.45}$$

$$Z = \begin{bmatrix} \hat{x}^{1,f} \\ \hat{x}^{2,f} \\ . \\ . \\ . \\ \hat{x}^{T,f} \end{bmatrix}, W = \begin{bmatrix} \theta_{1hom} \\ \theta_{2hom} \\ \theta_{3hom} \\ \theta_{het} \\ \xi \end{bmatrix}, \text{ and } e = \begin{bmatrix} e_0 \\ e_1 \\ . \\ . \\ . \\ e_{T-1} \end{bmatrix} \tag{5.46}$$

Following this, the least square parameters estimate can be obtained by

$$\hat{W} = (\breve{X}^\top \breve{X})^{-1} \breve{X}^\top Z \tag{5.47}$$

5.3.2 State Estimation

URTSS is applied for estimation of states. Here, a summary of the standard steps for UKF and smoother algorithm, explained earlier in Chapter 3, is provided.

1. Forward initialisation

As discussed earlier, forward step is initialised by set of bounded randomly generated initial states and covariance matrix.

$$\hat{x}_0, P_0 \tag{5.48}$$

Forward Iteration

Propagation of the sigma points through state equation given by equation (5.43)

$$\chi_{i,t+1}^{f-} = Q(\chi_{i,t}^{f}) \tag{5.49}$$

Calculation of the predicted state and predicted covariance matrix can be obtained as

$$\hat{x}_{t+1}^{f-} = \sum_{i=0}^{2n_x} W_i^m \chi_{i,t+1}^{f-} \tag{5.50}$$

$$P_{t+1}^{f-} = \sum_{2n_x}^{i=0} W_i^{(c)} (\chi_{i,t+1}^{f-} - \hat{x}_{t+1}^{f-})(\chi_{i,t+1}^{f-} - \hat{x}_{t+1}^{f-})^\top + \Sigma_e \tag{5.51}$$

where weights W can be obtained by equations (5.40) to (5.42). Filtered states and covariance matrix can be achieved by

$$K_{t+1} = P_{t+1}^{f-} C^\top (C P_{t+1}^{f-} C^\top + \Sigma_\epsilon)^{-1} \tag{5.52}$$

$$\hat{x}_{t+1}^{f} = \hat{x_{t+1}^{f-}} + K_{t+1}(y_{t+1} - C\hat{x}_{t+1}^{f-}) \tag{5.53}$$

$$P_{t+1}^{f} = (I - K_{t+1}C) P_{t+1}^{f-} \tag{5.54}$$

$$M_{t+1}^{f} = \sum_{i=0}^{2n_x} W_i^c (\chi_{i,t}^{f} - \hat{x_t^f})(\chi_{i,t+1}^{f-} - \hat{x}_{t+1}^{f-})^\top \tag{5.55}$$

where M_{t+1}^f is the cross-covariance of the states that will be used in backward iterations.

Backward Initialisation Backward pass is initialised by the updated covariance matrix and filtered states from forward iterations. This is presented by

$$P_T^b = P_T^f, \hat{x}_T^b = \hat{x}_T^f$$

Once the above steps are completed, the backward iterations start from time step (index) $T-1$ towards the first time step. Smoother gain, the smoothed states

and smoothed covariance matrix are calculated at backward step using

$$S_t = M_{t+1}^f [P_{t+1}^{f-}]^{-1} \tag{5.56}$$

$$\hat{x}_t^b = \hat{x}_t^f + S_t[\hat{x_{t+1}^b} - \hat{x}_{t+1}^{f-}] \tag{5.57}$$

$$P_t^b = P_t^f + S_t[P_{t+1}^b - P_{t+1}^{f-}]S_t^\top \tag{5.58}$$

5.4 Results and Discussion

5.4.1 Neural field Simulation and Estimation Results

In this section, the field simulation results and connectivity kernel gain estimation are discussed. Considering the existence of the heterogeneous connection in addition to a homogeneous connectivity, two different cases will be discussed. It can be shown that for a large heterogeneous connectivity kernel gain, the mean neural field will be dominated by the heterogeneous connection. In a second case scenario, a heterogeneous connection with a lower gain is introduced. In both cases, heterogeneous and homogeneous connectivity gains are estimated. Model given in equation (5.26) is used in these two case scenarios to provide a better understanding of introducing the heterogeneous connectivity on the synthetic field and estimation of kernel gains. Table 5.1 can be used as a reference point for parameter values for simulations and estimations unless stated otherwise.

Symbol	Parameter	Value	Unit
Model			
Δ	spatial discretisation step	0.5	mm
T_s	sampling time	0.001	sec
τ	synaptic time constant	0.01	sec^{-1}
ς	Slope of the firing rate function	0.56	mV^{-1} spike sec^{-1}
υ_0	firing threshold	1.8	mV
θ_{hom}	homogeneous connectivity kernel gains	[100,-80,5]	mV^{-1} $spike^{-1}$
θ_{het}	heterogeneous connectivity kernel gains	variant	mV^{-1} $spike^{-1}$
$\sigma_{\psi_{hom}}$	homogeneous connectivity kernel width	[1.8,2.4,6]	mm
$\sigma_{\psi_{het}}$	heterogeneous connectivity kernel width	[0.01]	mm
n_y	number of sensors	14×14=196	Not Applicable
Δ_y	distance between adjacent sensors	1.5	mm
σ_m	observation kernel width	0.9	mm
Σ_ε	observation noise variance	$0.1 \times I_{n_y}$	mm^2
σ_y	disturbance spatial covariance width	1.3	mm
σ_d^2	disturbance variance	0.1	mV^2
Reduced Model			
n_x	number of basis functions	9×9=81	Not applicable
Δ_ϕ	distance between field basis functions	2.5	mm
σ_ϕ	width of field basis functions	1.58	mm^2
Estimation			
α	range of variation for sigma points	0.001	Not Applicable
β	prior knowledge of sigma points	2	Not Applicable
κ	scaling parameter	$3 - n_x$	Not Applicable
λ	scaling parameter	80.99	Not Applicable

Table 5.1: Parameter values marked as variant is set in each Monte Carlo simulation. It does not mean that the value changes during the simulation but this is to indicate that the variable value is changed in different Monte Carlo simulation runs. Values for each specific simulation are fixed. Other parameters have been assumed to be fixed. For values of variant parameters, one can refer to their specified table of parameter values.

Considering the above mentioned assumptions, it is intended to estimate the heterogeneous connectivity kernel gains. As it can be seen in Figure 5.3, sharp edges appear on simulated field as a result of long-range connections.

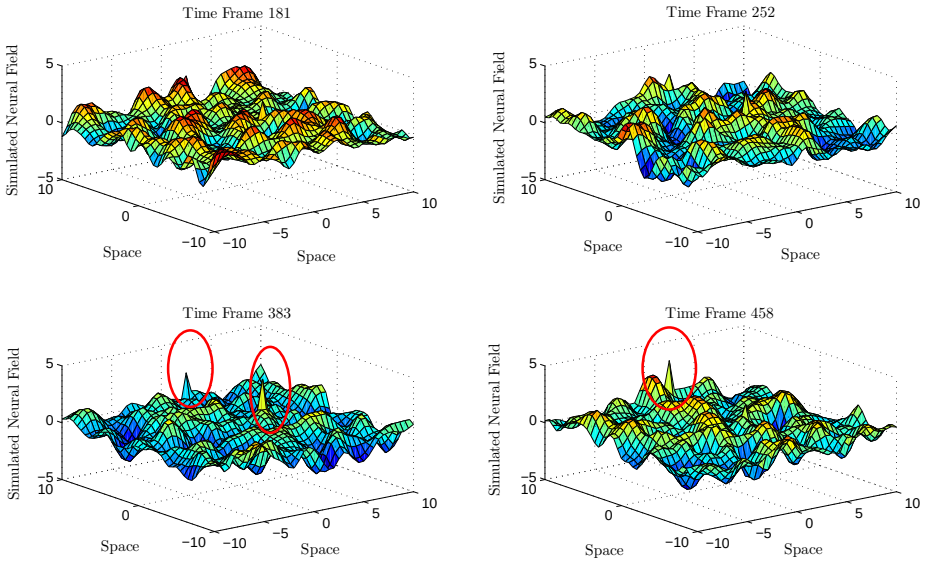

Figure 5.3: Sharp edges on neural field as a result of long-range connections.

The sharp incoming activity is a result of Dirac delta function modelled as a sharp Gaussian contributing to the neural field activity. A large residual existed when comparing the estimated gains with true values. Hence, a second approach is adapted where the structure of the long-range connection is considered as "one to many" connection points. In other words, a single point on neural field has a long-range connections to neighbourhood of a small area which can be defined by a wider Gaussian [Jirsa, 2004a].

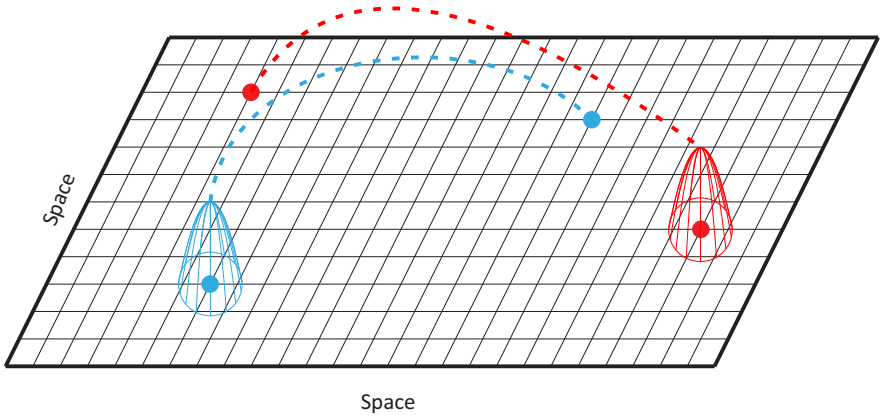

Figure 5.4: "One to many" long-range connection topology.

In the following subsections, two different cases will be explained where long-range connection gain is changed. In the first case, a large heterogeneous connectivity gain is assumed where as in the second case, a smaller long-range connection gain is assumed. Result of estimation is given in both cases. One of the important features is the mean neural activity shown for each case in Figures 5.6 and 5.7. More details will be given in the next subsection.

5.4.1.1 Case 1: High Heterogeneous Connectivity Gain

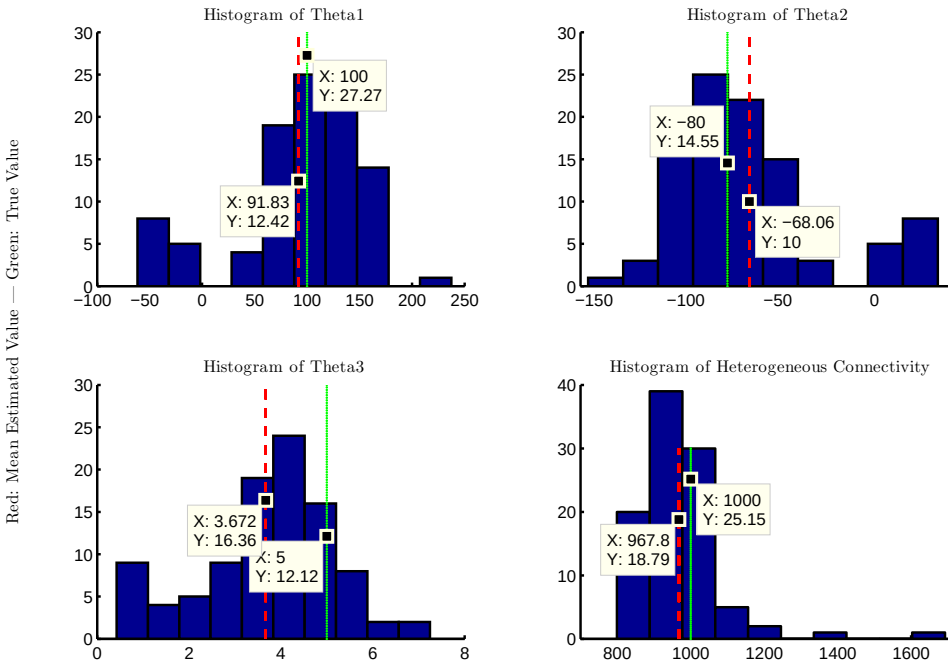

Figure 5.5: Heterogeneous connectivity gain estimation where the heterogeneous gain is chosen 40 times larger than the homogeneous peak strength.

Figure 5.5 demonstrates the gains of homogeneous connectivity kernel and estimated heterogeneous connectivity kernel gain for relative heterogeneous connectivity kernel gain of 40 where as homogeneous kernel gains gives a peak of 25. It can be seen in the plots, the mean of the estimated values for heterogeneous connectivity kernel is 967.8.

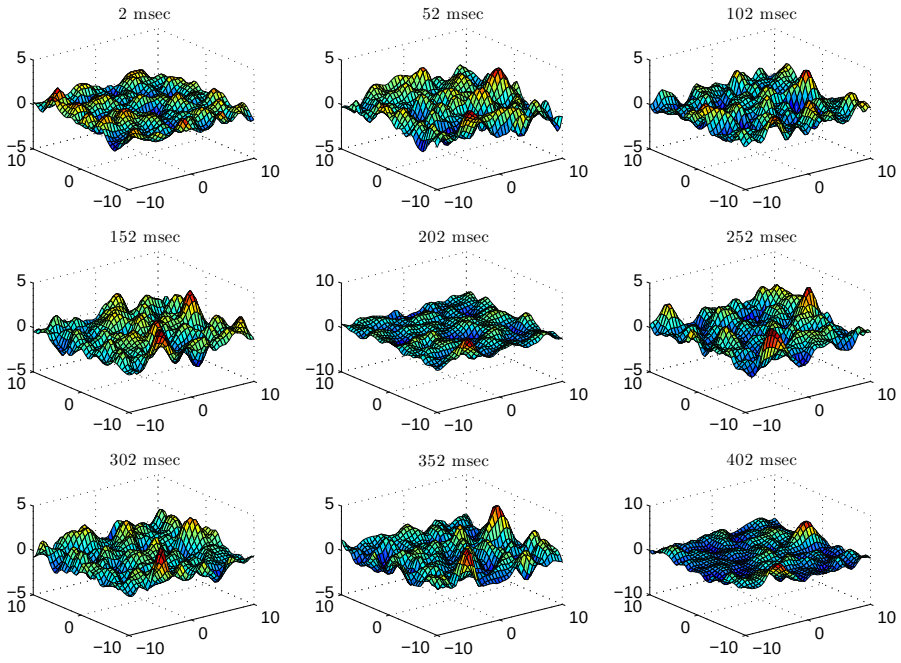

Figure 5.6: Neural field simulation where the heterogeneous connectivity with a high gain affecting the homogeneous field.

It should be noted that for such a high gain, the field will be dominated by heterogeneous connections which does not have a biological interpretation. Figure 5.6 is showing an example of this case where heterogeneous connectivity dominates the synthetic neural field.

In this case, the heterogeneous connectivity relative gain is assumed to be about forty which has dominated the simulated field over time. The main interest on running a heterogeneous connection with a high gain is to analyse the possibility of detecting the location of the heterogeneous connection based on the model mismatch which will be discussed in the next section.

5.4.1.2 Case 2: Smaller Heterogeneous Connectivity Gain

In this case, the heterogeneous connectivity is assumed to have a relative gain of four. Figure 5.7 demonstrates the changes in the simulated neural field from equation (5.31). As it can be seen for a small range of heterogeneous connection, the field is not dominated by the heterogeneous connection. This scenario is employed in longer time period and field dynamics are observed over the longer running time confirming the earlier statement.

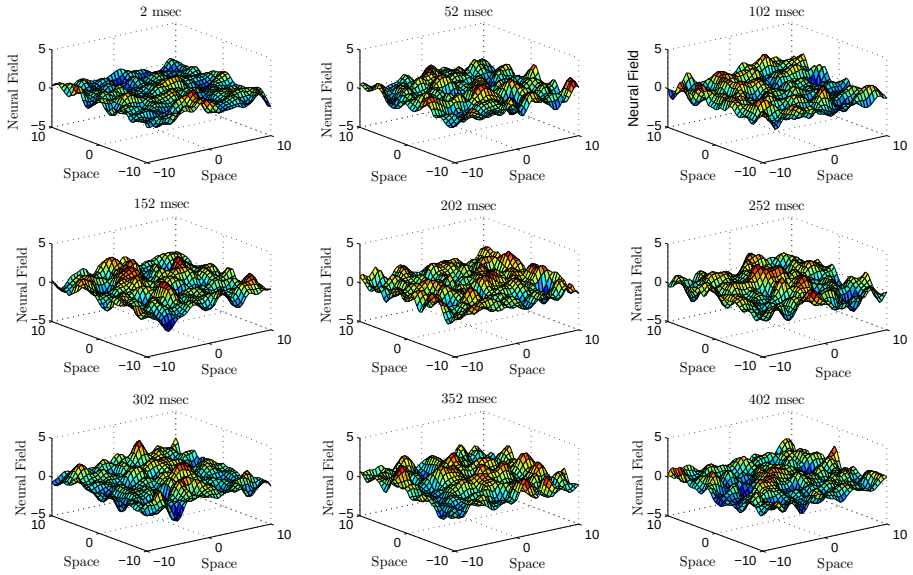

Figure 5.7: Simulated field at different time points with heterogeneous connectivity contributing to the mean field (Heterogeneous Gain: 100).

Figure 5.8 demonstrates the gains of homogeneous connectivity kernel and estimated heterogeneous connectivity kernel gain for relative heterogeneous connectivity kernel gain of 4 whereas the homogeneous kernel gains gives a peak of 25. Mean of the estimated values for heterogeneous connectivity kernel is 184. In estimation of weaker heterogeneous connectivity with smaller connectivity gain, big residuals is obtained. This can be due to the fact that heterogeneous contribution to the mean field model will be very negligible for small gains.

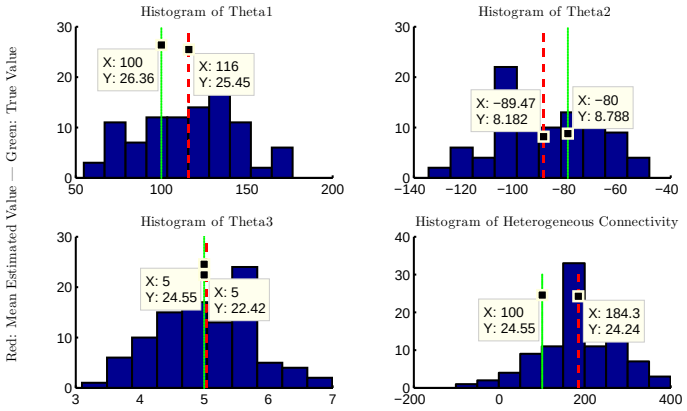

Figure 5.8: Histogram of heterogeneous connectivity gain estimation over 90 Monte Carlo simulations with true heterogeneous connectivity gain of 100.

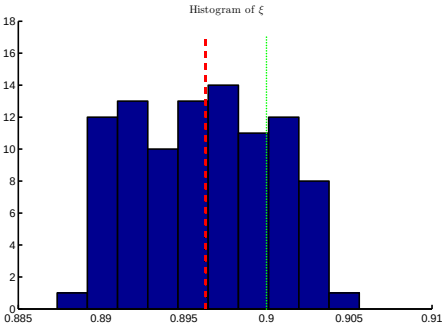

Figure 5.9: Histogram for estimation of parameter ξ.

Figures 5.8 and 5.9 show the histogram of estimated parameters for 100 Monte Carlo simulations. It is observed that the estimation result has improved in comparison to the case where a large heterogeneous connectivity gain was used in the simulation of the neural field. For a smaller heterogeneous connectivity kernel gain, the estimation will preform better under the assumption that the location of heterogeneous connectivity is known.

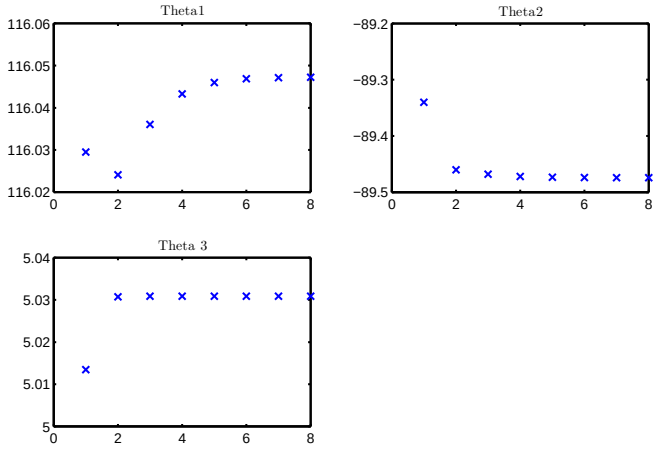

Figure 5.10: Convergence of the estimation algorithm.

Figure 5.10 demonstrates mean of 150 Monte Carlo simulations for 8 epochs of estimation iterations. It can be observed that the estimation has stopped due to convergence of the homogeneous connectivity kernel gains, θ_{hom}.

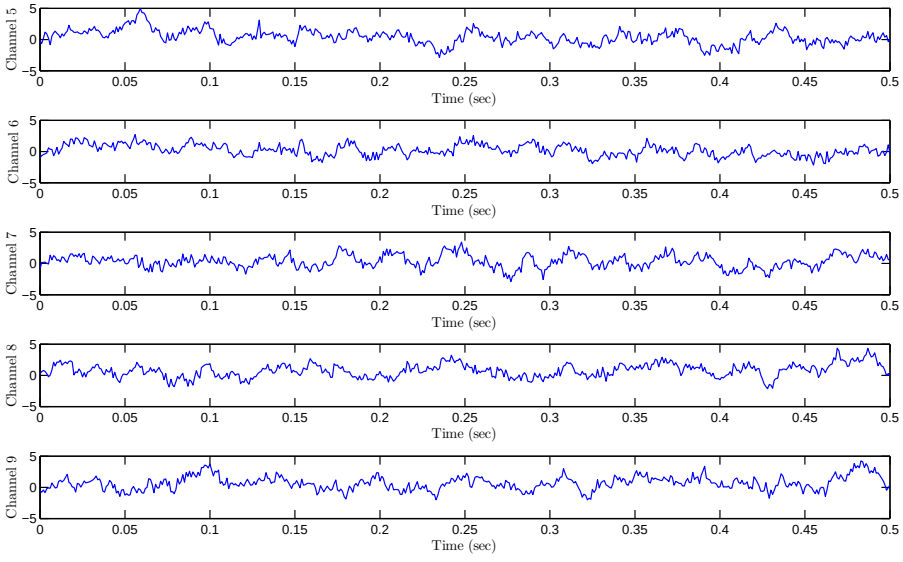

Figure 5.11: Observations from 5 different channels.

Observations from 5 randomly selected channels are displayed for a simulated neural field with relative heterogeneous connectivity gain of 100 in Figure 5.11.

5.4.2 Model Mismatch

In previous sections, it is demonstrated that by use of estimation framework explained in section 3.5, it is possible to estimate the homogeneous gains in addition to heterogeneous connectivity kernel gains. This is achieved with the assumption that heterogeneous connections are located randomly in the centre of field basis functions. In this section, the earlier assumption will be altered to a pair of long-range connection in the field in form of two random spatial locations. The assumption of symmetric connection is set, hence, the forward and backward connection gains are equal.

Model mismatch is based on the estimation of the connectivity kernel gains with initial assumption of a homogeneous field. Figure 5.12 shows the estimation result for a simulated field with a symmetric heterogeneous connectivity but the estimation is applied under the assumption of a homogeneous field. Estimated kernel gains are used to reconstruct the field and the calculated residuals will be the basis for checking the possible long-range connections as a result of a model mismatch. This approach becomes feasible when heterogeneous connectivity has a high gain in comparison to the homogeneous connectivity.

On the other hand, it should be noted that in a practical situation, direct access to underlying dynamics of neural field activity is not possible and recorded electrophysiological data is only noisy observations of the underlying neural activity.

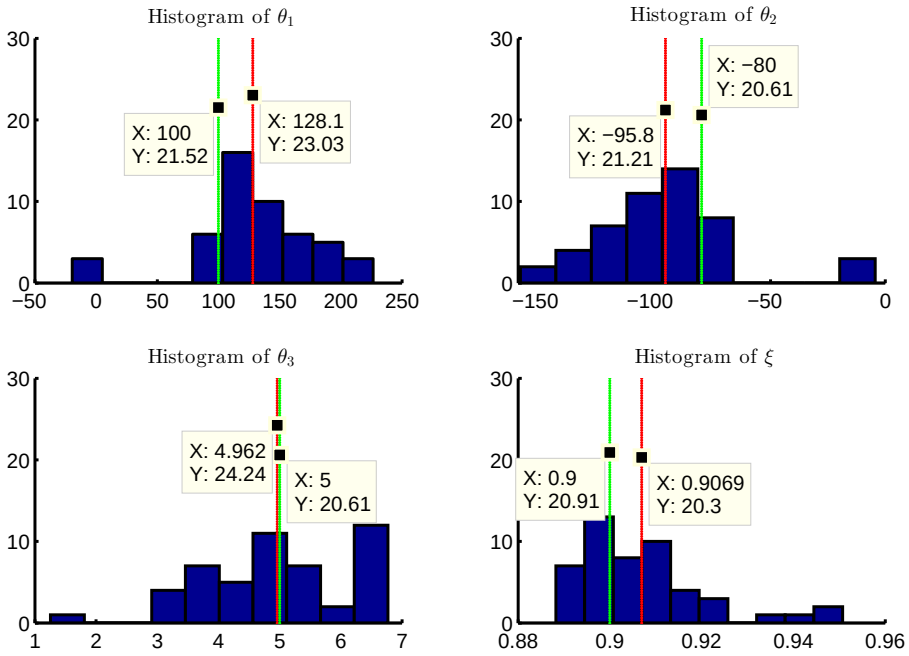

Figure 5.12: Histograms of estimated homogeneous connectivity kernel gain for 50 Monte Carlo simulations.

Model mismatch is used to identify the location of the heterogeneous connection and outcome is demonstrated in Figure 5.13. This can be obtained by subtracting the reconstructed homogeneous neural field from the original field. However, it should be noted that in real applications such an assumption can not be used for identification of the heterogeneous connection points as the real neural field is not available. This can be utilised if the effect of the heterogeneous connection becomes detectable from observations. On the other hand, the heterogeneous connection gain is assumed to be much bigger than the homogeneous gain. Heterogeneous connectivity kernel can have a wide range of gains but this should be a biologically plausible value. At the time of writing this thesis, there is no agreement on specific ranges of heterogeneous connection gains (to the author's best knowledge).

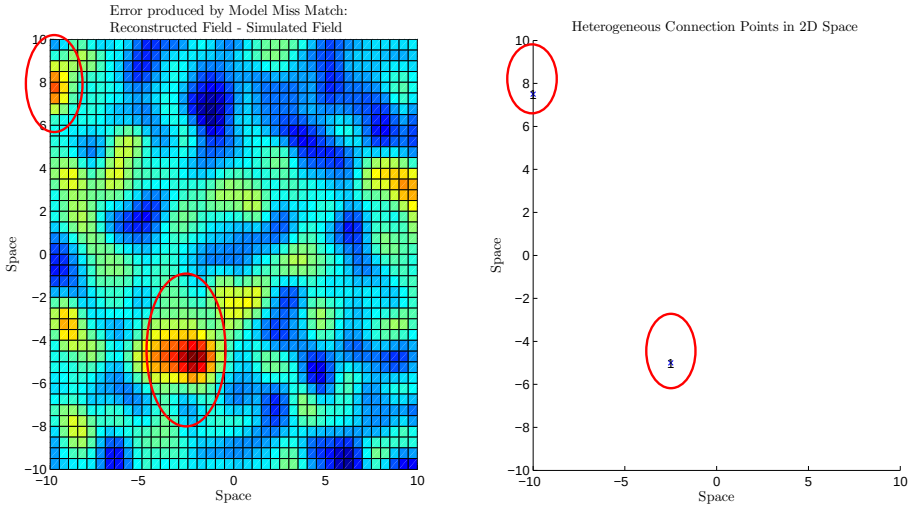

Figure 5.13: Identification of heterogeneous connection points.

The graph on the right panel shows the location of the long-range connections and the plot on the left panel indicates two peaks in error which are related to the heterogeneous connectivity connection. This is a good indication that for a strong heterogeneous connectivity gain, model mismatch can be used to obtain the location of the heterogeneous connections and estimation framework explained earlier in the section 5.3 can be used to obtain the heterogeneous connectivity gains. However, for smaller heterogeneous connectivity gains, current method is not adequate and further developments in modelling and identification framework is required.

Chapter 6

Conclusions

6.1 Summary

Considering the major developments in neural modelling, neural functions and their behaviours at different levels are explained in general. An opportunity appears to exist in targeting patient specific data analysis based on recorded data.

It is intended in the thesis to develop patient-focused models based on clinical iEEG recordings. Proposed methods can potentially contribute towards patient specific treatments, clinical decision making and where needed can be combined with other control design methods to improve the estimation results or to extend the analysis for a new purpose.

This thesis started with a general background on neuroscience, so a reader can understand the foundations of neuroscience where a very brief history of previous work is given. Previous work of Wilson & Cowan, Amari and Aram have been briefly explained. Amari type models and Wilson & Cowan models are well-known models in the computational neuroscience community considering their capabilities in explaining the underlying physiology.

Chapter 3 focused on the integration of the second order synaptic kernel to homogeneous model equations. Estimation of the parameters was provided under different case scenarios. It was demonstrated that the connectivity kernel shape can be obtained with a good accuracy. Considering that second order synaptic kernel is a general description of synaptic conductance profile and followed by re-

sults from this chapter, the proposed method was applied to the iEEG recordings from a patient with epilepsy.

Followed by the objectives achieved in Chapter 3, connectivity kernel gains were obtained during pre-seizure, seizure and post-seizure periods. It is observed that the connectivity kernel gains go through a transition as the underlying neural activity changes its state from pre-seizure to seizure and from seizure to post-seizure. The outline of the connectivity kernel pattern over full data length revealed an increase in inhibition and excitation activities during the seizure period. However, this analysis does not show that the seizure in this patient is predictable using this approach. This can be extended and evaluated on more date sets where the consistency in the performance of the algorithm can be tested.

Chapter 5 focused on introducing the heterogeneous connectivity as an extension to the previous work. It is intended to identify the long-range connections and estimate the heterogeneous connectivity kernel gains based on current estimation framework. It was demonstrated that under given conditions and mathematical description of long-range connections, detection of connection centres were not possible unless a structure with large connectivity gain was assumed. Additionally, it was demonstrated that the estimated of connectivity kernel gains (heterogeneous and homogeneous) is achievable by use of current estimation framework under certain assumptions such as fixed parameters during the simulations and one pair of symmetrical heterogeneous spatial connectivity. Details of all these assumption were discussed in Chapter 5.

6.2 Future Work

In this work different assumptions were made in order to develop efficient algorithms for neural field estimation. Removal or relaxing these assumptions will result in more biologically realistic models.

It is assumed that the model has fixed parameter values during the simulations. Such an assumption can be made for short periods of time but in a longer time period, more sophisticated methods should be adopted for estimation of the parameters where parameters are considered time variant and therefore the

estimation framework should be altered accordingly.

Part of the future work should focus on introducing time delay in the heterogeneous model caused by long-range connections. Previous work of Jirsa & Ding [2004] introduced time delays in the model where the stability of the model was also analytically studied. Other studies such as Marten *et al.* [2009b]; Walker *et al.* [2010] have also considered time delay and have discussed the modifications in the model derivation or the use of Delayed Differential Equations (DDE) with a number of assumptions to simplify the problem. Estimation of the model in the presence of time delays is a very challenging task. One can read more about time delay introduced by heterogeneity in neural modelling in the work of Jirsa & McIntosh [2007]. Utilising methods from system identification theory developed for estimation of models with time delays can provide a possible solution to deal with the effect of time delays arising from long-range connections at large networks. Future work can include the effect of time delay in the estimation framework.

Additionally, there exists a high sensitivity to the heterogeneous connectivity kernel gain in the proposed framework. More sophisticated detection methods can be combined with the proposed estimation framework to facilitate the identification of long-range connections.

Regarding the heterogeneous connectivity, a different model can be used where the heterogeneous function is considered as a function of distance between two heterogeneous connection points. It will be an interesting problem to check the correlation of neural field activity at different points considering such heterogeneous models. This might facilitate the identification of long-range connection points.

Another part of the future work can contribute towards parametrisation of the spatial connectivity kernel with more than three Gaussian kernels. This will provide more flexibility in extending the connectivity kernel to other sophisticated shapes.

Following the accomplished objectives on applications of developed model with second order synaptic kernel and Unscented Kalman Filter (UKF) to estimate the connectivity kernel gains, this can be extended to large cohort of data sets. An interesting result could be a trend of connectivity kernel gain trajectory

for each individual patient.

Bibliography

Abbott, L F. 1991. Realistic synaptic inputs for model neural networks. *Solutions*, **2**, 245–258. 14

Action, Epilepsy. 2015. *Epilepsy Action*. 68

Alejo J.Nevado Holgado. 2010. *Analysis of seizure evolution through neural mass modelling*. Ph.D. thesis. 3

Amari, Shun-ichi. 1977. Dynamics of pattern formation in lateral-inhibition type neural fields. *Biological cybernetics*, **27**(2), 77–87. 26

Aram, P., Freestone, D. R., Dewar, M., Scerri, K., Jirsa, V., Grayden, D. B., & Kadirkamanathan, V. 2013. Spatiotemporal multi-resolution approximation of the Amari type neural field model. *NeuroImage*, **66**(Oct.), 88–102. 3, 5, 44, 51, 68

Aram, Parham. 2011. *A Framework for modelling spatiotemporal cortical dynamics*. Doctor of Philosophy, The University of Sheffield. 19, 21, 28, 29, 31, 35, 47, 53, 63, 89, 96

Bayin, Selcuk. 2006. *Mathematical methods in science and engineering*. First edit edn. Wiley-Blackwell. 39, 90

Bear, M F, Connors, B W, & Paradiso, M A. 2007. *Neuroscience: Exploring the brain*. Neuroscience: Exploring the Brain. Lippincott Williams & Wilkins. viii, 7, 8, 9, 10, 11, 13, 20

Ben-Tal, Alona, & Smith, Jeffrey C. 2008. A model for control of breathing in mammals: Coupling neural dynamics to peripheral gas exchange and transport. *Journal of Theoretical Biology*, **251**(3), 480–497. 21

Bhattacharya, Basabdatta S. 2013. Implementing the cellular mechanisms of synaptic transmission in a neural mass model of the thalamo-cortical circuitry. *Frontiers in computational neuroscience*, **7**(July), 81. 15

Brackley, C. a., & Turner, M. S. 2009. Two-point heterogeneous connections in a continuum neural field model. *Biological Cybernetics*, **100**(5), 371–383. 31, 86

Braitenberg, V, & Schüz, A. 1991. *Anatomy of the cortex: statistics and geometry*. Studies of brain function. Springer-Verlag. 31

Breakspear, Michael, Jirsa, Viktor, & Deco, Gustavo. 2010. Computational models of the brain: From structure to function. *NeuroImage*, **52**(3), 727–730. 1

Bressloff, Paul C. 2003. Spatially periodic modulation of cortical patterns by long-range horizontal connections. *Physica D: Nonlinear Phenomena*, **185**(3-4), 131–157. 7, 86

Buzsáki, G C N Kent State U Online Resource Ohio U Alden 7Th Floor Qp376 .B88 2006 C.1 Available Bowling Green Science Stacks Qp376 .B88 2006 C.1 D U E 05-22-09 Kent State U Main See Bldg Guide Qp376 .B88 2006 C.1 Available Wright State FordhamHSL Stacks W L 300. 2006. *Rhythms of the brain*. 21

Chavez, M., Besserve, M., & Le Van Quyen, M. 2011. Dynamics of excitable neural networks with heterogeneous connectivity. *Progress in Biophysics and Molecular Biology*, **105**(1-2), 29–33. 86, 87

Coombes, S. 2005. Waves, bumps, and patterns in neural field theories. *Biological Cybernetics*, **93**(2), 91–108. 87

Coombes, S., Venkov, N. a., Shiau, L., Bojak, I., Liley, D. T J, & Laing, C. R. 2007. Modeling electrocortical activity through improved local approximations

of integral neural field equations. *Physical Review E - Statistical, Nonlinear, and Soft Matter Physics*, **76**(5), 051901. 22

Coombes, Stephen. 2010. Large-scale neural dynamics: simple and complex. *Neuroimage*, **52**(3), 731–739. 22

Cunningham, John P, & Yu, Byron M. 2014. Dimensionality reduction for large-scale neural recordings. *Nature Neuroscience*, **17**(11), 1500–1509. 3

David, Olivier, & Friston, Karl J. 2003. A neural mass model for MEG/EEG: Coupling and neuronal dynamics. *NeuroImage*, **20**(3), 1743–1755. 37

Destexhe, Alain, Mainen, Zachary F., & Sejnowski, Terrence J. 2002. Kinetic models for synaptic interactions. *The Handbook of Brain Theory and Neural Networks*, 1126–1130. 14, 16

Dewar, Michael, Scerri, Kenneth, & Kadirkamanathan, Visakan. 2009. Data-driven spatio-temporal modeling using the integro-difference equation. *IEEE Transactions on Signal Processing*, **57**(1), 83–91. 44

Dityatev, Alexander, & Rusakov, Dmitri a. 2011. Molecular signals of plasticity at the tetrapartite synapse. *Current Opinion in Neurobiology*, **21**(2), 353–359. 11

Falk, E B, Berkman, E T, & Lieberman, M D. 2012. From neural responses to population behavior: Neural focus group predicts population-level media effects. *Psychological Science*, **23**(5), 439–445. 22

Fratini, Michela, Bukreeva, Inna, Campi, Gaetano, Brun, Francesco, Tromba, Giuliana, Modregger, Peter, Bucci, Domenico, Battaglia, Giuseppe, Spanò, Raffaele, Mastrogiacomo, Maddalena, Requardt, Herwig, Giove, Federico, Bravin, Alberto, & Cedola, Alessia. 2015. Simultaneous submicrometric 3D imaging of the micro-vascular network and the neuronal system in a mouse spinal cord. *Scientific reports*, **5**(Jan.), 8514. 11

Freeman, Walter. 2007. Hilbert transform for brain waves. *Scholarpedia*, **2**(1), 1338. 20

Freestone, D. R., Aram, P., Dewar, M., Scerri, K., Grayden, D. B., & Kadirkamanathan, V. 2011. A data-driven framework for neural field modeling. *NeuroImage*, **56**(3), 1043–1058. 68

Freestone, D. R., Kuhlman, L., Chong, M.S., Nesic, D., Grayden, D.B., Aram, P., Postoyan, R., & Cook, M.J. 2013. Patient-specific neural mass modeling - stochastic and deterministic methods. *Pages 63–82 of: Recent Advances in Predicting and Preventing Epileptic Seizures*. WORLD SCIENTIFIC. 68

Freestone, D. R., Karoly, Philippa J, Nešić, Dragan, Aram, Parham, Cook, Mark J, & Grayden, David B. 2014. Estimation of effective connectivity via data-driven neural modeling. *Frontiers in neuroscience*, **8**(Jan.), 383. 68

Fürtinger, Stefan, Zinn, Joel C, & Simonyan, Kristina. 2014. A neural population model incorporating dopaminergic neurotransmission during complex voluntary behaviors. *PLoS computational biology*, **10**(11), e1003924. 22

Gabbiani, F, Midtgaard, J, & Knöpfel, T. 1994 (Aug.). *Synaptic integration in a model of cerebellar granule cells.* 16

Gastaut, H. 1970. Clinical and electroencephalographical classification of Eeileptic seizures. *Epilepsia*, **11**(1), 102–112. xii, 18

Gensini, Gian Franco, Conti, Andrea A, Lippi, Donatella, & Conti, Antonio. 2004. The historical bases of a super-specialty: electrocardiography. *Medicina nei secoli*, **16**(3), 595–602. 18

Gibson, Jay R, Beierlein, Michael, & Connors, Barry W. 2005. Functional properties of electrical synapses between inhibitory interneurons of neocortical layer 4. *Journal of neurophysiology*, **93**(1), 467–480. 13

Golub, Gene H, & Van Loan, Charles F. 2012. *Matrix computations*. Vol. 3. JHU Press. 45

Goodfellow, Marc, Schindler, Kaspar, & Baier, Gerold. 2011. Intermittent spike-wave dynamics in a heterogeneous, spatially extended neural mass model. *NeuroImage*, **55**(3), 920–932. 38

Harris, Kristen M, & Weinberg, Richard J. 2012. Ultrastructure of synapses in the mammalian brain. *Cold Spring Harbor perspectives in biology*, **4**(5), a005587—-. 20

Haykin, S. 2004. *Kalman filtering and neural networks*. Adaptive and Cognitive Dynamic Systems: Signal Processing, Learning, Communications and Control. Wiley. 33, 34, 35, 50, 53, 97

Haykin, Simon S. 2001. *Kalman filtering and neural networks*. New York, NY, USA: John Wiley & Sons, Inc. 52

Hendrey, Matthew, Ott, Edward, & Antonsen, Thomas. 1999. Effect of inhomogeneity on spiral wave dynamics. *Physical Review Letters*, **82**(4), 859–862. 87

Hesse, Wolfram, Möller, Eva, Arnold, Matthias, & Schack, Bärbel. 2003. The use of time-variant EEG Granger causality for inspecting directed interdependencies of neural assemblies. *Journal of neuroscience methods*, **124**(1), 27–44. 19

Hodgkin, A L, & Huxley, A F. 1952. A quantitative description of membrane current and its application to conduction and excitation in nerve. *The Journal of physiology*, **117**(4), 500–544. 22

Hormuzdi, Sheriar G, Filippov, Mikhail a., Mitropoulou, Georgia, Monyer, Hannah, & Bruzzone, Roberto. 2004. Electrical synapses: A dynamic signaling system that shapes the activity of neuronal networks. *Biochimica et Biophysica Acta - Biomembranes*, **1662**(1-2), 113–137. 14

Institute of Medicine (US) Committee on the Public Health Dimensions, England, Mary Jane, Liverman, Catharyn T, Schultz, Andrea M, & Strawbridge, Larisa M. 2012. *Epilepsy across the spectrum: Promoting health and understanding.* 17

Jazwinski, Andrew H. 2007. *Stochastic processes and filtering theory*. Courier Corporation. 35

Jirsa, V., & Haken, H. 1996. Field theory of electromagnetic brain activity. *Physical Review Letters*, **77**(5), 960–963. 3

Jirsa, V. K., & Kelso, J. a S. 2000. Spatiotemporal pattern formation in neural systems with heterogeneous connection topologies. *Physical Review E - Statistical Physics, Plasmas, Fluids, and Related Interdisciplinary Topics*, **62**(6 B), 8462–8465. 86

Jirsa, Viktor, & McIntosh, a R. 2007. *Handbook of brain connectivity*. Springer. 27, 114

Jirsa, Viktor, Group, Theoretical Neuroscience, & Sciences, Brain. 2008. *Neural masses, cortical fields and connectivity*. Tech. rept. Florida Atlantic University. 27, 33, 91

Jirsa, Viktor K. 2002. Heterogeneous connectivity patterns alter the timing variability in spatially distributed dynamic systems. *Nonlinear Phenomena in Complex Systems*, **4**, 356–363. 5, 32

Jirsa, Viktor K. 2004a. Connectivity and dynamics of neural information processing. *Neuroinformatics*, **2**(2), 183–204. 5, 103

Jirsa, Viktor K. 2004b. Information processing in bain and behavior displayed in large-scale scalp topographies such as EEG and MEG. *International Journal of Bifurcation and Chaos*, **14**(02), 679–692. 31

Jirsa, Viktor K. 2009. Neural field dynamics with local and global connectivity and time delay. *Philosophical transactions. Series A, Mathematical, physical, and engineering sciences*, **367**(1891), 1131–1143. 28, 92

Jirsa, Viktor K., & Ding, Mingzhou. 2004. Will a large complex system with time delays be stable? *Physical Review Letters*, **93**(7), 1–4. 114

Jirsa, Viktor K., Jantzen, Kelly J., Fuchs, Armin, & Kelso, J. a Scott. 2002. Spatiotemporal forward solution of the EEG and MEG using network modeling. *IEEE Transactions on Medical Imaging*, **21**(5), 493–504. 32, 87

Jirsa, V.K., & Haken, H. 1997. A derivation of a macroscopic field theory of the brain from the quasi-microscopic neural dynamics. *Physica D: Nonlinear Phenomena*, **99**(4), 503–526. 89

Johnson, Mark H. 2003. Development of human brain functions. *Biological Psychiatry*, **54**(12), 1312–1316. 2

Jradeh, Mouhamad. 2010. A new bidimensional neural field model with heterogeneous connection topology. *Neural computation*, **22**(10), 2647–2654. 28

Julier, Simon J, & Uhlmann, Jeffrey K. 1996. *A general method for approximating nonlinear transformations of probability distributions.* Tech. rept. Technical report, RRG, Department of engineering science, University of Oxford. 33, 35

Julier, Simon J, & Uhlmann, Jeffrey K. 1997. New extension of the Kalman filter to nonlinear systems. *Pages 182–193 of: AeroSense'97*. International Society for Optics and Photonics. 33, 35

Julier, Simon J, Uhlmann, Jeffrey K, & Durrant-Whyte, Hugh F. 1995. A new approach for filtering nonlinear systems. *Pages 1628–1632 of: American Control Conference, Proceedings of the 1995*, vol. 3. IEEE. 33, 35, 53

Kalman, R. E. 1960. A new approach to linear filtering and prediction problems. *Journal of Basic Engineering*, **82**(1), 35. 33, 50

Kaminski, M J, & Blinowska, K J. 1991. A new method of the description of the information flow in the brain structures. *Biological cybernetics*, **65**(3), 203–210. 19

Kandel, Eric R, Schwartz, James H, & Jessell, Thomas M. 2000. *Principles of neural science*. Vol. 4. McGraw-Hill. 1, 7, 9, 10, 14, 17

Kramer, Mark A, & Cash, Sydney S. 2012. Epilepsy as a disorder of cortical network organization. *The Neuroscientist : a review journal bringing neurobiology, neurology and psychiatry*, **18**(4), 360–372. 19, 20, 68

Kramer, Mark a, Szeri, Andrew J, Sleigh, James W, & Kirsch, Heidi E. 2007. Mechanisms of seizure propagation in a cortical model. *Journal of computational neuroscience*, **22**(1), 63–80. 20

Laing, Carlo R, Zou, Yu, Smith, Ben, & Kevrekidis, Ioannis G. 2012. Managing heterogeneity in the study of neural oscillator dynamics. *The Journal of Mathematical Neuroscience*, **2**(1), 5. 62

Lehnertz, K. 1999. Non-linear time series analysis of intracranial EEG recordings in patients with epilepsy–an overview. *International journal of psychophysiology : official journal of the International Organization of Psychophysiology*, **34**(1), 45–52. 19

Leuze, Christoph W U, Anwander, Alfred, Bazin, Pierre-Louis, Dhital, Bibek, Stüber, Carsten, Reimann, Katja, Geyer, Stefan, & Turner, Robert. 2014. Layer-specific intracortical connectivity revealed with diffusion MRI. *Cerebral cortex (New York, N.Y. : 1991)*, **24**(2), 328–339. 28

Liley, David T J, Bojak, Ingo, & Foster, Brett L. 2011. A mesoscopic modelling approach to anaesthetic action on brain electrical activity. 1–31. 23

Ljung, Lennart. 1998. *System identification*. Springer. 50

Lopes da Silva, F. 1991. Neural mechanisms underlying brain waves: from neural membranes to networks. *Electroencephalography and clinical neurophysiology*, **79**(2), 81–93. 37

Lopes da Silva, F. H., Hoeks, a., Smits, H., & Zetterberg, L. H. 1974. Model of brain rhythmic activity - The alpha-rhythm of the thalamus. *Kybernetik*, **15**(1), 27–37. 19, 20, 22, 37

Magee, J C. 2000. Dendritic integration of excitatory synaptic input. *Nature reviews. Neuroscience*, **1**(3), 181–190. 13

Malagarriga, Daniel, Villa, Alessandro E P, Garcia-Ojalvo, Jordi, & Pons, Antonio J. 2015. Mesoscopic segregation of excitation and inhibition in a brain network model. *PLoS computational biology*, **11**(2), e1004007. 20, 21

Markounikau, Valentin, Igel, Christian, Grinvald, Amiram, & Jancke, Dirk. 2010. A dynamic neural field model of mesoscopic cortical activity captured with voltage-sensitive dye imaging. *PLoS computational biology*, **6**(9), 289–301. 21

Marten, Frank, Rodrigues, Serafim, Suffczynski, Piotr, Richardson, Mark P., & Terry, John R. 2009a. Derivation and analysis of an ordinary differential equation mean-field model for studying clinically recorded epilepsy dynamics. *Physical Review E - Statistical, Nonlinear, and Soft Matter Physics*, **79**(2), 1–7. 17, 20, 41

Marten, Frank, Rodrigues, Serafim, Benjamin, Oscar, Richardson, Mark P, & Terry, John R. 2009b. Onset of polyspike complexes in a mean-field model of human electroencephalography and its application to absence epilepsy. *Philosophical transactions. Series A, Mathematical, physical, and engineering sciences*, **367**(1891), 1145–1161. 20, 114

Mascagni, Michael V, & Sherman, Arthur S. 1989. Numerical methods for neuronal modeling. *Methods*, 439–484. 22

McLaughlin, Deirdre P, Pachana, Nancy a., & Mcfarland, Ken. 2008. Stigma, seizure frequency and quality of life: The impact of epilepsy in late adulthood. *Seizure*, **17**(3), 281–287. 17

Mirowski, Piotr W, LeCun, Yann, Madhavan, Deepak, & Kuzniecky, Ruben. 2008. Comparing SVM and convolutional networks for epileptic seizure prediction from intracranial EEG. *Proceedings of the 2008 IEEE Workshop on Machine Learning for Signal Processing, MLSP 2008*, 244–249. 20

Moran, Rosalyn, Pinotsis, Dimitris A, & Friston, Karl. 2013. Neural masses and fields in dynamic causal modeling. *Frontiers in computational neuroscience*, **7**(Jan.), 57. 23

Moratal, David. 2012. *Principles of computational modelling in neuroscience*. First edit edn. Vol. 3. Cambridge, UK: Cambridge University Press. 14

Nevado-Holgado, Alejo J., Marten, Frank, Richardson, Mark P., & Terry, John R. 2012a. Characterising the dynamics of EEG waveforms as the path through

parameter space of a neural mass model: Application to epilepsy seizure evolution. *NeuroImage*, **59**(3), 2374–2392. 20

Nevado-Holgado, Alejo J., Marten, Frank, Richardson, Mark P., & Terry, John R. 2012b. Characterising the dynamics of EEG waveforms as the path through parameter space of a neural mass model: Application to epilepsy seizure evolution. *NeuroImage*, **59**(3), 2374–2392. 21

Nunez, P. L. 1974. The brain wave equation: A model for the EEG. *Mathematical Biosciences*, **21**(3-4), 279–297. 22

Panzeri, Stefano, Macke, Jakob H, Gross, Joachim, & Kayser, Christoph. 2015. Neural population coding: combining insights from microscopic and mass signals. *Trends in Cognitive Sciences*, **19**(3), 162–172. 21

Pearce, J M S. 2001. Emil Heinrich Du Bois-Reymond (1818-96). *Journal of Neurology, Neurosurgery & Psychiatry*, **71**(5), 620–620. 18

Petersen, Daniel P, & Middleton, David. 1962. Sampling and reconstruction of wave-number-limited functions in N-dimensional euclidean spaces. *Information and Control*, **5**(4), 279–323. 91

Pinotsis, D A, & Friston, K J. 2011. Neural fields, spectral responses and lateral connections. *NeuroImage*, **55**(1), 39–48. 32

Pinotsis, D A, Moran, R J, & Friston, K J. 2012. Dynamic causal modeling with neural fields. *NeuroImage*, **59**(2), 1261–1274. 22

Pinotsis, D A, Hansen, E, Friston, K J, & Jirsa, V K. 2013. Anatomical connectivity and the resting state activity of large cortical networks. *NeuroImage*, **65**(Jan.), 127–138. 28

Qubbaj, Murad R., & Jirsa, Viktor K. 2007. Neural field dynamics with heterogeneous connection topology. *Physical Review Letters*, **98**(23), 238102. 28, 32, 92

Rall, Wilfrid. 1967. Distinguishing theoretical synaptic potentials computed for different soma dendritic distributions of synaptic. *J Neurophysiol*, **30**(5), 1138–68. 15

Rasmussen, Carl Edward, & Williams, Christopher K I. 2005. *Gaussian processes for machine learning (adaptive computation and machine learning)*. The MIT Press. 91

Roth, a. 2009. Modeling synapses. *Chap. 6, pages 139–160 of: Computational Modeling Methods for Neuroscientists*, vol. 06. 15, 41

Roth, Jennifer K, Johnson, Marcia K, Tokoglu, Fuyuze, Murphy, Isabella, & Constable, R Todd. 2014. Modulating intrinsic connectivity: adjacent subregions within supplementary motor cortex, dorsolateral prefrontal cortex, and parietal cortex connect to separate functional networks during task and also connect during rest. *PloS one*, **9**(3), e90672. 87

Saeid Sanei, Jonathon A Chambers. 2007. *EEG signal processing*. 19

Sameshima, Koichi, & Baccalá, Luiz Antonio. 1999. Using partial directed coherence to describe neuronal ensemble interactions. *Journal of neuroscience methods*, **94**(1), 93–103. 19

Sanz-Leon, Paula, Knock, Stuart A, Spiegler, Andreas, & Jirsa, Viktor K. 2015. Mathematical framework for large-scale brain network modelling in The Virtual Brain. *NeuroImage*, **111**(Jan.), 385–430. 21

Särkkä, Simo. 2006. *Recursive baysian inference on stochastic differential equations*. Ph.D. thesis, The University of Technology. 48

Sarkka, Simo. 2008. Unscented Rauch-Tung-Striebel Smoother. *IEEE Transactions on Automatic Control*, **53**(3), 845–849. 50

Särkkä, Simo. 2010. Continuous-time and continuous–discrete-time unscented Rauch–Tung–Striebel smoothers. *Signal Processing*, **90**(1), 225–235. 48

Särkkä, Simo, & Hartikainen, Jouni. 2010. Gaussian optimal smoothing of non-linear state space models. *IEEE Transactions on Automatic Control*, **55**(8), 1938–1941. 48

Schiff, Steven J, & Sauer, Tim. 2008. Kalman filter control of a model of spatiotemporal cortical dynamics. *BMC Neuroscience*, **9**(Suppl 1), O1. 35

Seeger, Matthias. 2004. *Gaussian processes for machine learning.* Vol. 14. 31

Sejnowski, Terrence J, & Poggio, Tomaso a. 2007. *Dynamical Systems in Neuroscience Computational Neuroscience.* Vol. 25. London, England: The MIT Press, Cambridge, Massachusetts. 11

Spiegler, Andreas, Knösche, Thomas R, Schwab, Karin, Haueisen, Jens, & Atay, Fatihcan M. 2011. Modeling brain resonance phenomena using a neural mass model. *PLoS computational biology*, **7**(12), e1002298. 2, 21

Stefanescu, Roxana a., & Jirsa, Viktor K. 2008. A low dimensional description of globally coupled heterogeneous neural networks of excitatory and inhibitory neurons. *PLoS Computational Biology*, **4**(11), e1000219. 86

Stigler, Stephen M. 1981. Gauss and the Invention of Least Squares. *Ann. Statist.*, **9**(3), 465–474. 98

Strogatz, Steven H. 1994. *Nonlinear dynamics and chaos.* Westview Pr. 41

Suffczynski, P, Kalitzin, S, & Lopes Da Silva, F H. 2004. Dynamics of non-convulsive epileptic phenomena modeled by a bistable neuronal network. *Neuroscience*, **126**(2), 467–84. 20

Ullah, Ghanim, & Schiff, Steven. 2009. Models of epilepsy. *Scholarpedia*, **4**(7), 1409. 19, 20

US National Institutes of Health, National Institute on Aging. 2008. *Synapse.* viii, 12

Van Der Merwe, Rudolph. 2004. *Sigma-point Kalman filters for probabilistic inference in dynamic state-space models.* Ph.D. thesis, Oregon Health & Science University. 35

Van Veen, B D, van Drongelen, W, Yuchtman, M, & Suzuki, a. 1997. Localization of brain electrical activity via linearly constrained minimum variance spatial filtering. *IEEE transactions on bio-medical engineering*, **44**(9), 867–880. 22

Walker, Jamie J, Terry, John R, & Lightman, Stafford L. 2010. Origin of ultradian pulsatility in the hypothalamic-pituitary-adrenal axis. *Proceedings. Biological sciences / The Royal Society*, **277**(1688), 1627–1633. 114

Wan, Eric A, & Van Der Merwe, Rudolph. 2000. The unscented Kalman filter for nonlinear estimation. *Pages 153–158 of: Adaptive Systems for Signal Processing, Communications, and Control Symposium 2000. AS-SPCC. The IEEE 2000*. IEEE. 35

Wan, Eric A, Van Der Merwe, Rudolph, & Nelson, Alex T. 1999. Dual Estimation and the Unscented Transformation. *Pages 666–672 of: NIPS*. Citeseer. 35

Wendling, F., Bartolomei, F., Bellanger, J. J., & Chauvel, P. 2001. *Interpretation of interdependencies in epileptic signals using a macroscopic physiological model of the EEG*. Tech. rept. 7. Laboratoire Traitement du Signal et de L'Image - INSERM, Université de Rennes 1, Campus de Beaulieu, 35042 Rennes Cedex, France. fabrice.wendling@univ-rennes1.fr. 20, 63

Wendling, F., Bartolomei, F., Bellanger, J. J., & Chauvel, P. 2002. Epileptic fast activity can be explained by a model of impaired GABAergic dendritic inhibition. *European Journal of Neuroscience*, **15**(9), 1499–1508. 20

Whittaker, V P. 1963. Synaptic transmission. *California Medicine*, **2**(2), 203. 15

Wikipedia, Quasar Jarosz at English. 2009. *Neuron Cell*. viii, 11, 14

Wilson, Hugh R, & Cowan, Jack D. 1972. Excitatory and inhibitory interactions in localized populations of model neurons. *Biophysical journal*, **12**(1), 1–24. 19, 23

Wilson, Hugh R, & Cowan, Jack D. 1973. A mathematical theory of the functional dynamics of cortical and thalamic nervous tissue. *Kybernetik*, **13**(2), 55–80. 23, 26

Wright, J.J., & Liley, D.T.L. 1996. Dynamics of the brain at global and microscopic scales: Neural networks and the EEG. *Behavioral and Brain Sciences*, **19**(02), 285. 7, 22

Zhou, Shui-Sheng, Liu, Hong-Wei, & Ye, Feng. 2009. Variant of Gaussian kernel and parameter setting method for nonlinear SVM. *Neurocomputing*, **72**(13-15), 2931–2937. 27